論文 / 著書情報
Article / Book Information

題目(和文)	耐シンタリング性と耐コーキング性に優れたシリカライト-1内包ニッケル触媒によるメタンドライ改質に関する研究
Title(English)	Study on Methane Dry Reforming by Silicalite-1 Encapsulated Nickel Catalyst with Excellent Sintering and Coking Resistance
著者(和文)	ZHANGYUSHENG
Author(English)	Yusheng Zhang
出典(和文)	学位:博士(工学), 学位授与機関:東京工業大学, 報告番号:甲第12427号, 授与年月日:2023年3月26日, 学位の種別:課程博士, 審査員:多湖 輝興,関口 秀俊,下山 裕介,松本 秀行,横井 俊之
Citation(English)	Degree:Doctor (Engineering), Conferring organization: Tokyo Institute of Technology, Report number:甲第12427号, Conferred date:2023/3/26, Degree Type:Course doctor, Examiner:,,,,
学位種別(和文)	博士論文
Type(English)	Doctoral Thesis

Tokyo Tech

Study on Methane Dry Reforming by Silicalite-1 Encapsulated Nickel Catalyst with Excellent Sintering and Coking Resistance

by

Yusheng Zhang

A Dissertation Submitted to the
Department of Chemical Science and Engineering
Tokyo Institute of Technology
in Partial Fulfillment of the Requirements for
the Degree of Doctor of Engineering

March, 2023

Contents

Chapter 1. Introduction

1.1.Syngas production and utilization

Synthesis gas (syngas) is a generic term for raw gas mixtures, primarily consisting of carbon monoxide (CO) and hydrogen (H_2) in various ratios. It is the key building block and intermediate to be further synthesized and upgraded to various value-added chemicals and fuels[1,2]. The composition of syngas is highly dependent upon the inputs to the reactor (e.g., feedstock, feed gas ratio, reaction conditions, catalyst), affecting the H_2/CO ratio and components in the final gas mixture. Theoretically, as shown in **Fig. 1.1**, the syngas can be generated from any hydrocarbon feedstock, such as coal, natural gas, crude oil, petroleum coke, biomass and waste, carbon dioxide (CO_2), and so on[3]. The existing technology for syngas production includes gasification or pyrolysis of coal, biomass, and waste, reforming of natural gas, partial oxidation of heavy hydrocarbons, electrochemical reduction of CO_2, etc.[4–6] The choice of the technology to produce syngas depends on the cost and availability of the feedstock and the downstream desired product production. Furthermore, the product gas inevitably contains a certain amount of other components, for example, CO_2, H_2O, CH_4, and sometimes SO_2. Therefore, the produced raw syngas usually needs to be cleaned and purified, e.g., desulfurization, soot removal, acid gas removal, to remove the impurities and contaminants, and conditioning, e.g., Water–Gas Shift Reaction, Methanation, and introduction N_2, to adjust the H_2/CO ratio to the desired composition.[2]

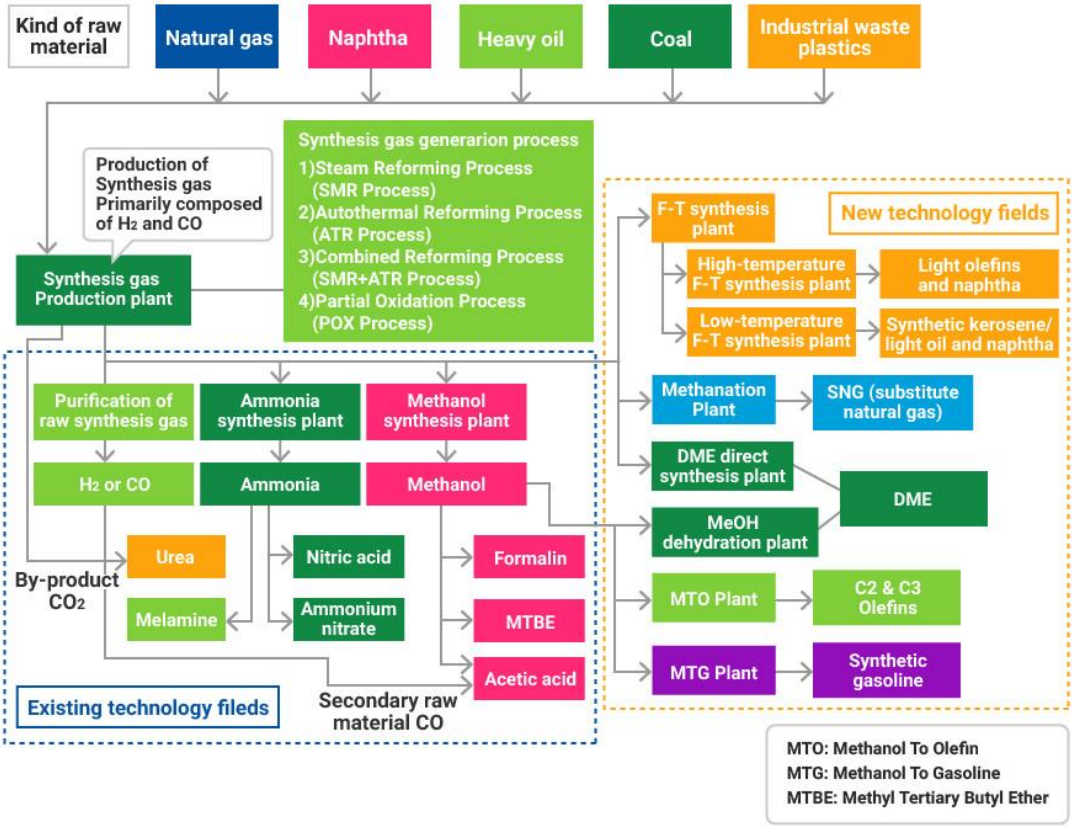

Figure 1.1. The production and utilization of syngas [7]

As shown in **Table 1.1** and **Fig. 1.2**, the syngas with different compositions can be utilized in a variety of fields. Typically, the syngas can be used directly as fuel to generate electricity and heat[8]. Apart from this, as mentioned above, syngas is the flexible intermediate used for the production of valuable chemicals. Reportedly, the primary syngas chemically derived products are ammonia and its derivatives (urea, nitric acid, and ammonium nitrate).[3,9] Besides, syngas is also applied as a hydrogen source in the refinery, providing hydrogen for refining heavy crude by hydrotreating and hydrocracking processes.[10,11] Additionally, syngas is the raw material in producing clean synthetic fuels, such as synthetic natural gas, oxo alcohol, and methanol, which has a crucial role in the manufacturing of olefins, gasoline, acetic acid, formaldehyde, methyl methacrylate, and methyl tertiary-butyl ether.[12–14] In addition to these applications, the Gas-to-liquids (GTL), which can convert natural gas via syngas into transportation fuels based on Fischer-Tropsch (F-T) process, are now drawing considerable attention as well.[4,15]

All in all, syngas is the crucial and prominent hub that connects upstream resources, such as natural gas, coal, crude oil, and biomass, with downstream desired liquid fuels and chemical products.

Table 1.1. Composition and utilization of syngas

Composition	Utilization
flexible	Heat and electricity production
Pure H_2	Ammonia synthesis, Refinery hydrotreating and hydrocracking, Fuel cell
$H_2 : CO = 2 : 1$	Methanol, alkenes, and alcohols synthesis
$H_2 : CO = 1 : 1$	Aldehydes and long-chain hydrocarbons synthesis
CO	Acids (formic and acetic)

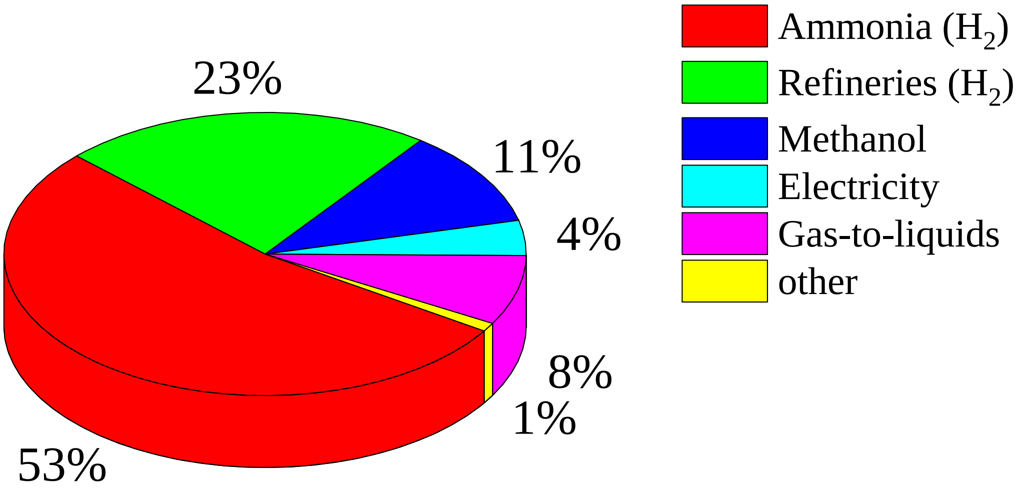

Figure 1.2. The world syngas market in 2019, totally ~6 EJ/y. [2]

1.2. Introduction of methane reforming

It is reported that syngas production accounts for about 50-60% of the overall cost of the GTL process[16], so it is of great significance to manufacture syngas from the cheap and abundant feedstock. Thanks to the shale gas revolution and the discovery of large reserves of natural gas, coalbed methane, and combustible ice, methane as the main component of these resources has come to the fore as a primary source to produce syngas[15,17–20].

The methane is converted to syngas through a reforming process. In general, the most common reforming of methane to syngas can be divided into four main types[10,21]: (i) steam reforming (SRM) , (ii) partial oxidation (POM) , (iii) dry (CO2) reforming (DRM) , (iv) combined reforming, a combination of any two or all the three processes, e.g., autothermal reforming (ATR: SRM + POM or DRM + POM) , combined steam and dry reforming (CSDRM: SRM + DRM), and tri-reforming (SRM+POM+DRM). The differences between the processes are based on the oxidant used (H_2O, O_2, CO_2, and their mixtures), thus leading to the different energetics and kinetics of the reaction and the produced syngas with different H_2/CO ratios. The main characteristics of each process are described in the following text and summarized in **Table 1.2**.

1.2.1. Steam reforming of methane (SRM)

$$CH_4 + H_2O \longleftrightarrow 3H_2 + CO \qquad \Delta_r H^{\circ}_{298K} = +206\ \text{kJ/mol} \qquad \textbf{Equation 1}$$

Steam reforming of methane (SRM) is a well-established and industrially applied process in which methane is reacted with steam in the presence of a catalyst to produce syngas.[22–24] As shown in **Equation 1**, theoretically, SRM can produce syngas with an H_2/CO ratio of 3. Since it can provide H_2-rich product gas, currently, SRM is the most widely used process to generate hydrogen. The manufactured hydrogen is generally utilized in ammonia synthesis, fuel cells, and petroleum refining. On the other hand, because this technology yields syngas with a high hydrogen concentration, the produced gas is unsuitable for other synthesis applications, for example, methanol synthesis (typically requiring syngas with an H_2/CO ratio of 2.) Consequently, in industry, a specified amount of carbon dioxide is often introduced into the feed gas to increase the proportion of carbon monoxide in the product to meet the diverse needs of downstream utilization.

SRM is a strongly endothermic reaction, it was commonly carried out at high temperatures of 700~1000 °C, so it requires a large amount of energy input and is therefore highly energy intensive and very expensive. Furthermore, owing to the presence of steam and ultra-high operation temperature, the catalyst's degradation and collapse always occur.[11,25] Developing a catalyst with outstanding hydrothermal stability is indispensable under high-temperature steaming conditions.

1.2.2. Partial oxidation of methane (POM)

$$CH_4 + 1/2O_2 \longleftrightarrow 2H_2 + CO \qquad \Delta_r H^{\circ}_{298K} = -36\ \text{kJ/mol} \qquad \textbf{Equation 2}$$

Another attractive process for syngas generation is the partial oxidation of methane (POM, **Equation 2**), which utilizes oxygen as the oxidant in a highly exothermic reaction to stoichiometrically produce syngas with an H_2/CO ratio of 2. This ratio is desired for downstream methanol and [13,26–28] (F-T) synthesis to manufacture heavier hydrocarbons and naphtha. Additionally, compared to the SRM process, the POM process exhibits several advantages, such as high energy effectiveness, very short residence time, and high conversion rates.

However, despite its exothermicity, high temperatures (800–1000 °C) are required to obtain a high yield of H_2 and CO.[29,30] Combined with the exothermic nature, it would induce hot spots in the reactor, which makes this reaction difficult to control. Moreover, there also is a risk of explosion due to direct contact of methane with oxygen at elevated temperatures. Furthermore, it is also difficult to keep the catalyst in a reducing state and thus to lead to the rapid deactivation of the catalyst.[31–33] Apart from these, the POM process usually needs the construction of an accompanying oxygen plant to provide pure oxygen, which also imposes substantial investment. All these challenges hinder this process from being industrialized.

1.2.3. Dry reforming of methane (DRM)

$$CH_4 + CO_2 \longleftrightarrow 2H_2 + 2CO \qquad \Delta_r H^{\circ}_{298K} = +247 \text{ kJ/mol} \qquad \textbf{Equation 3}$$

With the increasing concerns on climate change, carbon neutrality, a concept dedicated to reducing and removing greenhouse gases (GHGs) emissions, has become the common goal of the international community. Dry reforming of methane (DRM) has aroused intensive attention since it provides a promising means of converting and offsetting two leading greenhouse gases, CO_2 and CH_4, as feedstock to produce syngas.[34–36] Typically, DRM was conducted at high temperatures, 600-900 °C, because of the strong endothermic nature to achieve high conversion levels and high syngas yields.[37,38] The DRM is a cheaper route compared to the SRM and POM processes due to the simpler separation of end products. Furthermore, as presented in

Equation 3, the H_2/CO ratio from DRM is near unity, which is suitable for producing oxygenated chemicals and long-chain hydrocarbons, considering that the high H_2/CO ratio would limit the carbon chain growth in F-T synthesis.[39,40]

However, this process is not commercially available due to the following limitations: (i) the high operating temperature of DRM would trigger the sintering of active metal of the employed catalyst, and thus fast catalyst deactivation; (ii) the ability of carbon dioxide to remove deposited carbon on the catalyst is weaker than steam and oxygen; therefore, the DRM reaction is also more likely to have severe coke content; (3) the requirement for pure CO_2 increases the investment.

1.2.4 Combined reforming of methane

In view of disadvantages and limitations of the separate methane reforming process, the combined reforming, which operates at various combinations of two or three processes and varying ratios of H_2O, O_2, and CO_2 to overcome the drawbacks of the single process and to regulate the H_2/CO ratio in the product gas, has attracted academic and industrial interests.

The most popular combined reforming is autothermal reforming (ATR), in which the endothermic process, SRM or DRM, is coupled with the exothermic POM process into one compact reactor[38,41,42]. In other words, the exothermic POM process could provide the heat for the endothermic process, resulting in a net reaction enthalpy of zero. The ATR shows some synergistic benefits. It can effectively improve heat transfer and energy efficiency, thus reducing the total energy input and cost, but also avoiding the hot spot of the reactor and operating more safely. Moreover, coke deposition can be mitigated because of the oxidation of carbon species, hence increasing the catalyst's lifetime. Furthermore, it can provide a flexible H_2/CO molar ratio to meet diverse applications by changing the feed's H_2O/O_2 or CO_2/O_2 ratio. However, combining several processes often also means more reactions and parameters are involved, indicating a more complex control system and more complicated operating conditions required.

Another attractive combined technology is the coupling of SRM and DRM (CSDRM).[25] As discussed earlier, the independent SRM or DRM process cannot produce syngas to meet different demands. Given this, in industry, carbon dioxide is sometimes co-fed to the SRM system to flexibly adjust the composition of the outlet gas. Additionally, combining dry reforming with steam reforming can alleviate the significant carbon formation problem for dry reforming. Unfavorably, CSDRM is an endothermic process and requires high energy input to sustain the reaction.

As for the tri-reforming technology[43–45], it integrates the synergetic effects of the great environmental value of DRM, the high economic benefit of SRM, and the high energy efficiency of POM, while it also encounters challenges of the combined reforming techniques mentioned above.

Table 1.2. The advantages and disadvantages of different methane reforming techniques

Technology	Advantages	Disadvantages
SRM	✓ Mature industrial technology ✓ Production of H_2-rich gas	■ High heat supply ■ Degradation of catalyst ■ H_2/CO ratio often higher than required
POM	✓ High energy efficiency ✓ Low carbon deposition ✓ Product gas is suitable for methanol and olefins synthesis	■ Hot spot ■ Hard to keep the catalyst in a reducing state ■ Require a costly air separation plant
DRM	✓ Convert two leading greenhouse gases ✓ Simpler separation of product gas ✓ Product gas is suitable for producing oxygenated chemicals and long chain hydrocarbons	■ High heat supply ■ Relatively high coke deposition ■ Require pure CO_2
ATR	✓ Lower energy input ✓ Thermodynamical neutrality ✓ Avoid the hot spot	■ More difficult control system ■ More complicated operating conditions
CSDRM	✓ Flexible H_2/CO ratio ✓ Suppress coke formation	■ High heat supply ■ More difficult control system ■ More complicated operating conditions
Tri-reforming	✓ Flexible H_2/CO ratio ✓ Lower energy input	■ More difficult control system ■ More complicated operating conditions

1.3. Brief on thermodynamics, kinetics, and mechanism of DRM

Last year, almost 200 countries came together in Glasgow, UK, to commit to taking action on climate change and forged the Glasgow Climate Pact. To deliver on the Pact, the world needs to halve emissions of greenhouse gases over the next decade and reach net zero carbon emissions by the middle of the century. In this sense[46], the DRM process is of great significance to achieving the carbon peaking and carbon neutrality goals. Therefore, in this research, the DRM is the target reaction. To overview the DRM reaction, the fundamental aspects of DRM reaction, including the thermodynamics, kinetics, and reaction mechanisms, will be discussed.

1.3.1. Thermodynamics

It is common knowledge that thermodynamics determines the extent to which reactions occur to achieve high conversion of CH_4 and CO_2, produce a high yield of syngas, and calculate the equilibrium composition.

Several researchers have systematically studied the thermodynamics of DRM reactions.[38,47–50] Based on their results and the actual situation of our lab, the thermodynamic analysis was performed using Gibbs free energy minimization method under a feed gas composition of $CH_4/CO_2/Ar/He = 2/2/4/1$ and pressure of 1 bar.

Generally, in parallel with the primary DRM reaction (**Equation 3**), various side reactions listed in **Table 1.3** can concurrently occur during the DRM process, such as reverse water-gas shift reaction (RWGS, **Equation 4**), coke formation reactions, e.g., CH_4 decomposition (**Equation 5**) and CO disproportionation (Boudouard reaction**,** **Equation 6**), and coke removal reactions, e.g., CO_2 gasification (**Equation 7**) and

Carbon-water reaction (**Equation 8**). Therefore, all these possible reactions are taken into account for thermodynamic calculation.

Reverse water-gas shift

$CO_2 + H_2 \longleftrightarrow H_2O + CO$ $\Delta_r H^\circ_{298K} = +41$ kJ/mol **Equation 4**

CH_4 decomposition:

$CH_4 \longleftrightarrow C(s) + 2H_2$ $\Delta_r H^\circ_{298K} = +75$ kJ/mol **Equation 5**

CO disproportionation (Boudouard reaction):

$2CO \longleftrightarrow C(s) + CO_2$ $\Delta_r H^\circ_{298K} = -173$ kJ/mol **Equation 6**

CO_2 gasification

$C(s) + CO_2 \longleftrightarrow 2CO$ $\Delta_r H^\circ_{298K} = +173$ kJ/mol **Equation 7**

Carbon-water reaction

$C(s) + H_2O \longleftrightarrow H_2 + CO$ $\Delta_r H^\circ_{298K} = +131$ kJ/mol **Equation 8**

As shown in **Table 1.3** and **Fig. 1.3**, the DRM reaction is highly endothermic. It takes place spontaneously at temperature, denoted as T_s, above 640 °C. The conversions of methane and carbon dioxide increase with reaction temperature. In other words, because CO_2 and CH_4 molecules have high stability and need high activation energy to dissociate, DRM process requires high temperature to realize the equilibrium conversion. However, the sintering of the catalyst's active site would be more severe at a higher temperature.[51,52] Additionally, for the DRM process, the coke deposition on the catalyst is another obstacle to hinder DRM commercialization.[53–55] It is widely accepted that coke is formed mainly from the CH_4 decomposition ($T_s \geq 546$ °C) and CO disproportionation ($T_s \leq 703$ °C). Whereas CO_2 gasification ($T_s \geq 703$ °C) and carbon-water reaction (T_s ≥670 °C), which consume accumulated carbon, would spontaneously occur at high temperatures. Overall, the maximum coke deposition is favorable in the temperature range of 550–700°C. The coke formation could be suppressed dramatically with the development of advanced catalysts. If without coke formation, as depicted in **Fig. 1.3b**, the H_2/CO ratio is generally lower than 1 due to the concurrent RWGS reaction, which results in a higher CO_2 conversion than CH_4 conversion and a higher amount of CO compared to H_2 in the product.[56] On the other hand, the H_2/CO ratio gradually increases as the reaction temperature increases. Given all results, the DRM reaction should be operated at a temperature above 700 °C to achieve a high yield of syngas and low carbon deposition.

Table 1.3. Thermodynamic analysis of the DRM process[48,49]

Reaction	$\Delta_r H^{\circ}_{298K}$ (kJ/mol)	T_s: $\triangle G_T \leq 0$ (°C)	Effect
DRM	+247	≥643	/
RWGS	+41	≥827	H_2/CO < 1
CH_4 decomposition	+75	≥546	Coke formation
CO disproportionation	-173	≤ 703	Coke formation
CO_2 gasification	+173	≥703	Coke removal
Carbon-water reaction	+131	≥670	Coke removal

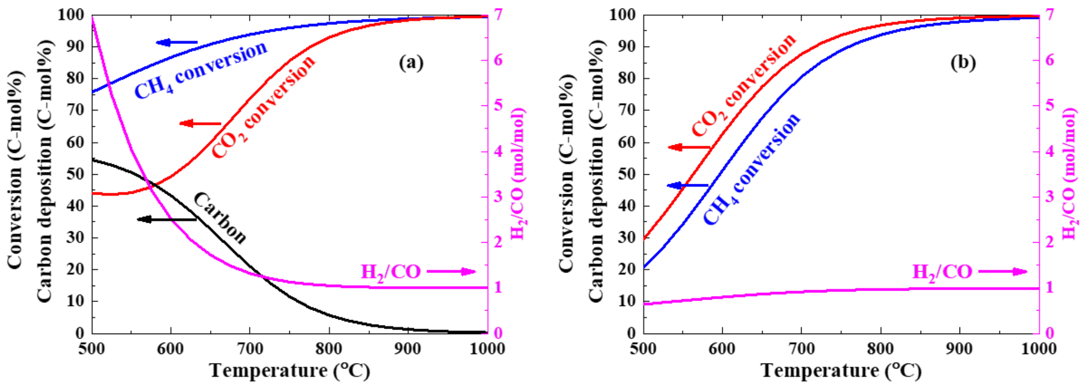

Figure 1.3. Thermodynamic equilibrium analysis of DRM reaction as a function of temperature: (a) with coke formation, (b) without coke formation.

(The reaction conditions: $CH_4/CO_2/Ar/He = 2/2/4/1$, 1 bar)

1.3.2 Kinetics and mechanism

Kinetic studies describe the reaction rate and how factors such as temperature, the concentration of the reactants, and catalysts affect it. Determining the reaction rate also helps to determine the reaction mechanism and thus can understand the dominant reaction pathways and rate-determining steps (RDS). Therefore, the kinetics and mechanism are always analyzed together. Based on the kinetics and mechanism results, researchers can further optimize catalyst and reactor design and improve overall DRM development.

The DRM reaction process is complex. The reaction mechanism is affected by many factors, such as catalyst property (acidity, promoter, and support) and reaction conditions. Although there is still some controversy about the kinetics and mechanism of the DRM reaction, as shown in **Fig. 1.4** and **Table 1.4**, it is generally accepted that the DRM reaction is composed of four parts: methane adsorption and dissociation, carbon dioxide adsorption and dissociation, formation of surface hydroxyls and water, and CH_x oxidation and formation and desorption of CO and H_2.[57–59]

i. Methane adsorption and dissociation:

The primary elementary step of the DRM reaction is the adsorption of CH_4 on the metallic surface. This step is fast and always at equilibrium. Then, the adsorbed CH_4 will be successively dissociated to form chemisorbed hydro-carbonate radicals S_1-CH_x ($0 \leq x < 4$), liberating hydrogen or forming chemisorbed S_1-H radicals. The intermediate S_1-CH_x can be further dissociated to form S_1-C and S_1-H radicals. The S_1-C radical is a significant source of coke formation. In consideration of that methane is very stable, so the initial C–H bond activation of methane needs to overcome a high energy barrier. Therefore, some researchers thought CH_4 dissociation is the rate-determining step (RSD) and determines the overall reaction rate.

ii. Carbon dioxide adsorption and dissociation:

CO_2 is preferentially adsorbed on the metal surface or metal-support interface to form either carbonate or bicarbonate species. Then, the activation and dissociation of CO_2 proceed. Commonly there are two possible routes for CO_2 activation and dissociation. First, the direct dissociation of CO_2 will occur to form adsorbed S_2-CO and S_2-O or to produce CO directly and leave an adsorbed oxygen atom, S_2-O. The second way is that the radical H* from the dissociation of CH_4 can activate the CO_2 to produce S_2-CO and S_2-OH.

iii. Formation of surface hydroxyls and water

Most kinetic models predict that the surface hydroxy groups can form in two ways:

the formed S_2-O will release the oxygen by oxygen spillover from the support to the metal surface, on which the oxygen will react with the S_1-H to generate the surface hydroxyls on the metal surface, denoted as S_1-OH; or the hydrogen will transfer from S_1-H on the metal surface to S_2-O on the support by hydrogen spillover to form S_2-OH; thus the occupied active site on the metallic surface will be free. Once the S_1-OH is formed, it will react with adjacent S_1-H to produce water, clearing two active sites.

iv. CH_x oxidation and formation and desorption of CO and H_2

The surface S_1-CH_x, including S_1-C, can react with the formed surface hydroxyls, S_1-OH, and oxygen from the CO_2 to form S_1-CH_xO or S_1-CO. Then, the decomposition of S_1-CH_xO will occur to yield CO and H_2. Considering that the desorption of CO and H_2 to the gas phase is very fast, some researchers considered that the decomposition of S_1-CH_xO to yield CO and H_2 would be the rate-determining steps.

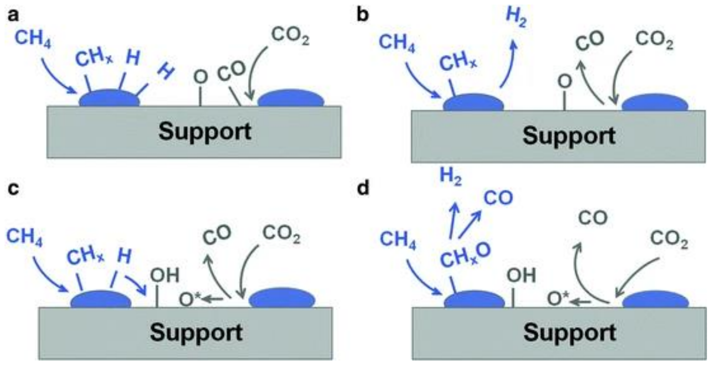

Figure 1.4. Reaction steps for the dry reforming of methane. (a) Adsorption and dissociation of CH_4 and CO_2 on the metal and the metal–support interface, respectively. (b) CO and H_2 desorption are fast steps. (c) Surface hydroxyls are formed from hydrogen and oxygen spillover. (d) Surface oxygen species or hydroxyls oxidize the hydrogen-depleted surface methyl-like species (S_1–CH_x), forming S_1–CH_xO species and finally CO and H_2.[57]

Table 1.4. Elementary DRM reaction steps occur on the catalysts' surface.[57,60]

Methane adsorption and dissociation		
$CH_4 + S_1 \longleftrightarrow S_1\text{-}CH_4$	Adsorption	
$S_1\text{-}CH_4 + (4\text{-}x)S_1 \longrightarrow S_1\text{-}CH_x + (4\text{-}x)S_1\text{-}H$	Dissociation	RDS
$S_1\text{-}CH_4 + S_1 \longrightarrow S_1\text{-}CH_3 + S_1\text{-}H$	Dissociation	
$S_1\text{-}CH_3 + S_1 \longrightarrow S_1\text{-}CH_2 + S_1\text{-}H$	Dissociation	
$S_1\text{-}CH_2 + S_1 \longrightarrow S_1\text{-}CH + S_1\text{-}H$	Dissociation	
$S_1\text{-}CH + S_1 \longrightarrow S_1\text{-}C + S_1\text{-}H$	Dissociation	
$2S_1\text{-}H \longleftrightarrow H_2 + 2S_1$	Dissociation	
Carbon dioxide adsorption and dissociation		
$CO_2 + S_2 \longleftrightarrow S_2\text{-}CO_2$	Adsorption	
$S_2\text{-}CO_2 + S_2 \longleftrightarrow S_2\text{-}CO + S_2\text{-}CO$	Dissociation	First route
$S_2\text{-}CO_2 \longrightarrow S_2\text{-}O + CO$	Dissociation	
$S_2\text{-}CO_2 + S_1\text{-}H \longleftrightarrow S_2\text{-}CO + S_2\text{-}OH$	Dissociation	Second route
Formation of surface hydroxyls and water		
$S_2\text{-}O + S_1\text{-}H \longleftrightarrow S_2\text{-}OH + S_1$		First route
$S_1\text{-}H + S_2\text{-}O \longleftrightarrow S_1\text{-}OH + S_2$		Second route
$S_1\text{-}H + S_1\text{-}OH \longleftrightarrow H_2O + 2S_1$		
CH_x oxidation and formation and desorption of CO and H_2		
$S_1\text{-}CH_x + S_1\text{-}OH \longleftrightarrow S_1\text{-}CH_xO + S_1\text{-}H$		
$S_1\text{-}C + S_1\text{-}OH \longleftrightarrow S_1\text{-}CO + S_1\text{-}H$		
$S_1\text{-}CH_x + S_2\text{-}O \longleftrightarrow S_1\text{-}CH_xO + S_2$		
$S_1\text{-}C + S_2\text{-}O \longleftrightarrow S_1\text{-}CO + S_2$		
$S_1\text{-}CH_xO + S_1\text{-}H \longleftrightarrow S_1\text{-}CO + x/2H_2$		RDS
$S_1\text{-}CO \longleftrightarrow S_1 + CO$		
$S_1\text{-}H \longleftrightarrow H_2 + 2S_2$		

S_1 and S_2 denote active sites on the metal and metal–support interface, respectively. In CH_x, $0 \leq x < 4$.

1.4. Discussion of DRM catalyst

As described above, the dissociation of CH_4 and CO_2 requires high activation energy and temperature to function, so using an efficient catalyst in the DRM process can remarkably reduce the reaction temperature, increase the reaction rate, and achieve high activity, selectivity, and stability.

1.4.1. Catalyst type

Numerous scientific publications reported that most group VIII transition metals, except osmium (Os), exhibited some activity in the DRM reaction.[61,62] Generally, DRM catalysts' main active components are grouped into noble and non-noble metals.

Noble metal-based catalysts (Rh, Ru, Ir, Pt, and Pd) are very active for DRM reaction owing to their high dispersion and small particle size. Among these noble metals, the order of catalytic activity has been reported as follows: Rh≈Ru> Ir > Pt > Pd.[6,63,64] On the other hand, the noble metal-based catalysts also showed high resistance to coke deposition due to small equilibrium constants for methane decomposition and low dissolution of carbon into their lattices. Nevertheless, the precious metals' low availability and high price restrict their application in large-scale industrial processes.

With an eye to this, developing stably available and cheap alternatives has caught researchers' eyes, especially Nickel (Ni) and Cobalt (Co). It has been revealed that the supported Co catalyst, especially over silica and alumina supports, showed considerable activity and stability for the DRM process.[34,65–68] However, the reducibility of Co-based catalysts is usually poor, e.g., the maximum reduction was only achieved at 50% reduction on Co/Al_2O_3 catalyst at temperature as high as 900 °C.[69,70] Hence, the activity of Co-supported catalysts is neither superior to noble metals nor nickel catalysts. Ni-based catalysts have been the only transition metal that exhibited catalytic activity comparable to precious metals, so Ni-based catalysts are the most promising candidate for the DRM process. However, Ni-based catalysts suffered from fast deactivation due to the heavy carbon deposition and metal sintering.[50,67,71] Therefore, significant efforts have been made to understand the mechanism and pathways of Ni-based catalyst deactivation in the DRM reaction. Plenty of studies have been devoted to finding the solution to overcome the obstacles.

1.4.2. Improving suppression of coke formation

As stated in the thermodynamics section, in parallel with the primary DRM reaction, two carbon deposition reactions, methane cracking and Boudouard reaction, can also occur. As cartoon in **Fig. 1.5**, coke accumulation would lead to the deactivation of the Ni catalyst via different mechanisms.[50,72,73] Firstly, coke deposited on and covered the surface of Ni particles and metal-support interface, thus deactivating their CH_4 and/or CO_2 activation and dissociation activity. Second, coke accumulated inside or on the mouth of the support pores and grew until sufficiently large to block the pores and inhibit both the reactants diffusing into the inner active sites and the formed products diffusing out of them into the gas phase. Additionally, filamentous carbon can form and grow on Ni catalyst during the DRM process as well. This strong filamentous carbon may build up in pores to the extent of ultimately causing the breakage of the catalyst, potentially with catastrophic consequences ranging from increased pressure drop and loss of activity to reactor blockage in reactors and hot spots that can lead to reactor failure. On the other hand, it has been confirmed that the growth of carbon filaments follows the tip-growth mechanism, whereby the Ni particles detached from its support during the growth process, which then migrated to the tip of the carbon nanotubes. As a result, the loss of Ni active sites would become unavoidable after catalyst regeneration.

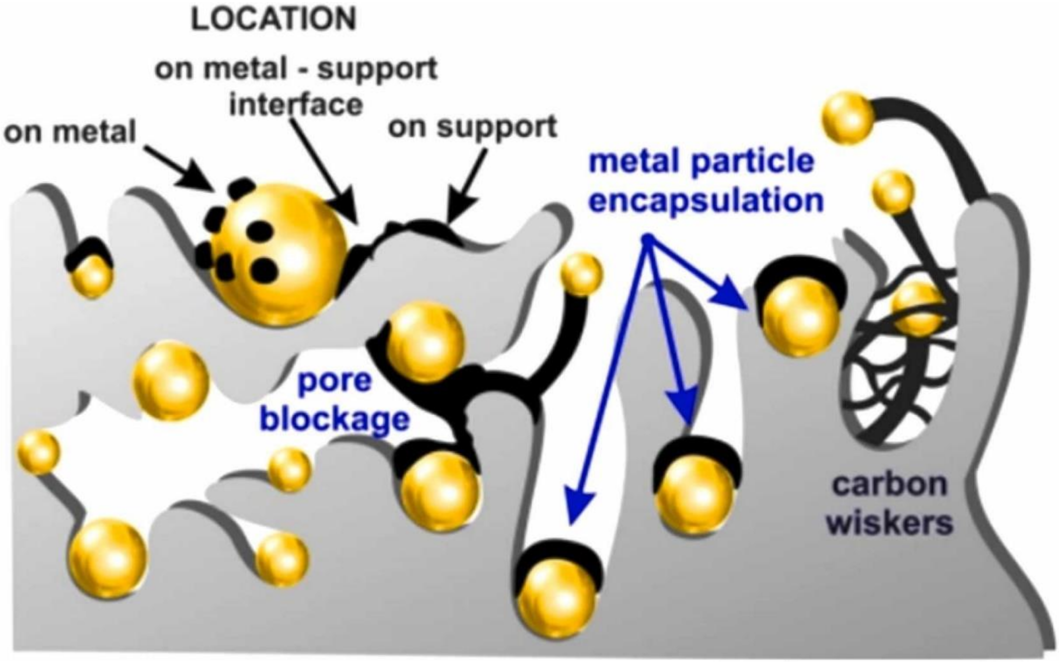

Figure 1.5. Chemical and mechanical mechanisms of catalyst deactivation owing to coke deposition.[72,73]

Different kinds of carbon species that vary in morphology and reactivity would form during the DRM process[74] (see **Fig. 1.6** and **Table 1.5**). For example, CH_4 and CO dissociation would directly form atomic carbon, Cα, adsorbed and dispersed on the surface of Ni particle as surface carbide. Typically, the Cα is highly reactive, which can be further converted to other carbon. For instance, vermicular, polymeric amorphous whisker or fibrous carbon, Cv; bulk Ni carbide, Cγ; polymeric amorphous carbon films and filaments, Cβ, that again react to give a fully grown, highly ordered, crystalline, highly stable graphitic carbon platelets and layers, Cc.

It should also be emphasized that not all forms of carbon can form or affect catalytic activity. The carbon formation and accumulation depend greatly on reaction conditions—especially temperature.[75] For instance, the surface carbide (Cα) and polymeric carbon films (Cβ) are prone to form at low reaction temperatures (<500 °C). In comparison, graphitic carbon films (Cc) accumulate in the intermediate temperature range of 500–550 °C. As described in the deactivation mechanism owing to carbon deposition, if the carbon species encapsulate the surface of Ni, they can block active sites for adsorption and reaction. At high temperatures above 600 °C, the most notorious type of carbon on nickel catalysts for DRM reaction, the filamentous carbon or whisker carbon, Cv, could form and accumulate. Therefore, in practice, regions of carbon-forming potential during the DRM process must be carefully avoided. Operating the DRM process at temperatures above 700 °C can greatly inhibit carbon formation from the thermodynamic point of view. However, the DRM is a strongly endothermic reaction, if the same large vertical fixed-bed reactor for commercial SRM reformer is employed to constitute a DRM reactor system, the temperature of the catalyst bed in the center and downstream may be well below 700 °C. In other words, forming carbon deposits is still possible in these areas. In light of this, preparing a catalyst with superior coking suppression is essential.

A. Methane (hydrocarbon) decomposition

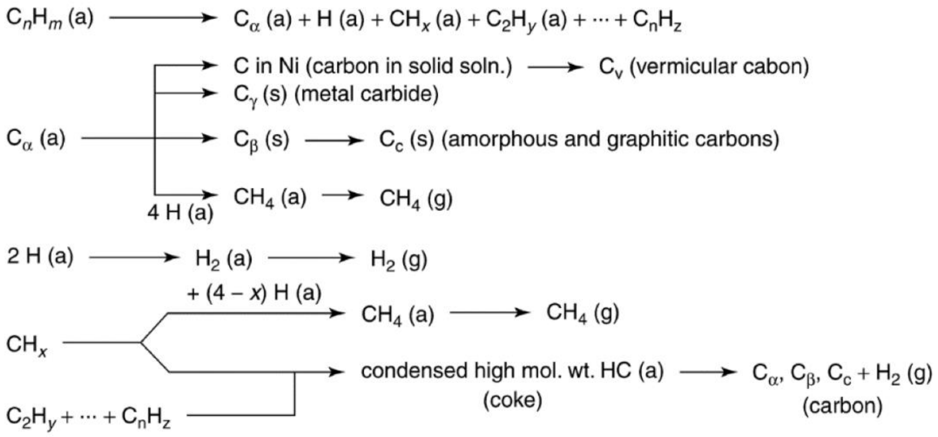

B. Carbon monoxide dissociation

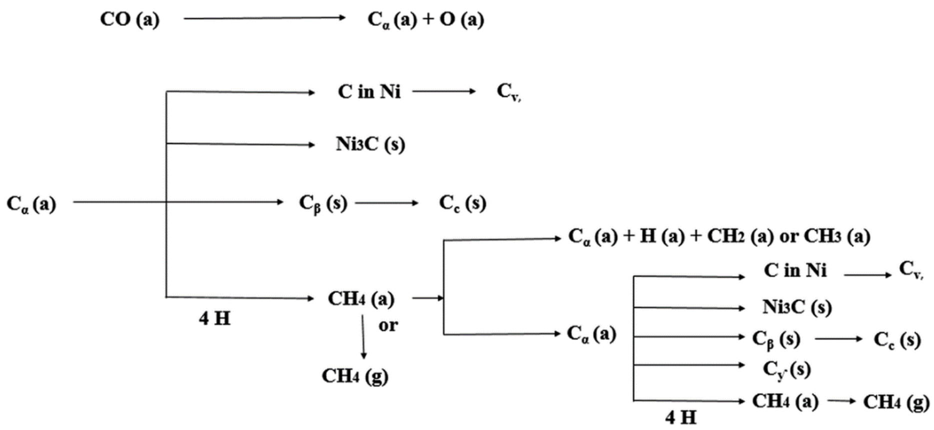

Figure 1.6. Mechanism of formation of various coke species on Ni particle surface by: (A) methane (hydrocarbon) decomposition, and (B) carbon monoxide dissociation. States of coke: a= adsorbed, g = gas, s= solid.[74,75]

Table 1.5. Formation of different carbon species on Ni catalyst surface[11,74].

Carbon structure	Notation	Formation temperature (°C)
Surface-adsorbed, atomic carbon	$C\alpha$	200 – 400
Polymeric amorphous films	$C\beta$	250 – 500
Vermicular filaments or whiskers	Cv	300 – 1000
Bulk Ni carbide	$C\gamma$	150 – 250
Crystalline, graphitic platelets film layers	Cc	500 – 550

Evidently, the coke accumulation rate is determined by the difference in rates of formation and gasification of coke precursors. If the gasification rate is equal to or greater than that of formation, coke is not accumulated. Thus, improving the carbon gasification and/or decreasing the coke formation of the Ni catalyst are effective ways to reduce coke deposition. It is well known that the coke formation and gasification rate under given conditions can vary significantly with catalyst structure, including promoter, catalyst support, and Ni particle size.

As mentioned earlier, noble metals can drastically inhibit coke formation and improve catalyst performance. A common and financially feasible way to prevent coke formation is the addition of small amounts of noble metals to Ni catalysts. Both experimental studies and DFT calculation have verified the benefits of Ni-promoted catalysts with noble metals (Rh, Ru, Ir, Pt, Pd, and Au) in terms of their higher activity and coke resistance compared to the non-promoted Ni catalysts. [65,76] Notably, the loading of noble metals is very critical. The optimal concentrations are typically below 0.5wt% as promoters.

Another vastly chosen strategy is incorporating Co onto the Ni catalyst to reduce methane dissociation and enhance the surface reaction of carbon removal.[77,78] Combining Ni and Co could increase metal dispersion, enhance the hydrogenation of atomic carbon and/or inhibit the formation of carbide species in the metal crystal compared to the Ni and Co monometallic catalysts.

Many methods have been investigated to increase the rate of carbon gasification. As illustrated in the earlier reaction mechanism, the reaction between surface oxygen species and coke precursor is vital to remove the carbon on the catalyst. Since the surface oxygen species are derived from the CO_2 dissociation, one prevalent approach is the use of the alkaline metal (Na_2O and K_2O) and alkaline earth metal (MgO and CaO) as a modifier in Ni catalyst to increase the catalyst's basicity for improved adsorption and dissociation of CO_2. This approach contributes further to providing oxygen species that can react with coke intermediates such as CH_x [79–81]and Ni carbide, strengthening the resistance to carbon formation. However, it is worth noting that adding alkaline or earth-alkaline metals to the Ni catalyst can cut down carbon formation. However, this advantage could be compensated with the low conversion of CH_4.

Noticeably, the catalyst with high oxygen mobility, vacancy, and storage capacities can increase the number and availability of mobile surface oxygen species on the catalyst.[72] These mobile oxygen species aid in the oxidation of accumulated carbon, promoting the carbon gasification process and lowering the deactivation rate during the DRM reaction. Cerium oxide (CeO_2) has been demonstrated to be a good support or promoter of Ni catalyst because of its remarkable oxygen storage capacities and unique redox properties.[82,83] It can store and deliver active oxygen with the Ce^{4+}/Ce^{3+} redox cycles by filling the oxygen vacancy defects. As a result, it can enhance catalytic stability in terms of reducing carbon deposition.[84,85] In addition to CeO_2, ZrO_2 is reportedly a good candidate with high oxygen storage support for Ni catalysts in like manner.[23,86–88]

Interestingly, several authors stressed that the nucleation and growth process of the carbon was greatly affected by the Ni particles size. Generally, a decrease in the particle size of nickel could increase the DRM activity and limit coke formation. It was observed by TEM that the Ni particle size on the Ni-alumina aerogel catalyst significantly influenced the formation of filamentous carbon. Most whisker carbons were formed over metal particles larger than 7 nm.[89] This phenomenon was also verified on Ni-Co bimetallic catalyst. Ni-Co catalysts with active metal particles smaller than 6 nm generated negligible carbon and showed superior resistance to coking.[90] DFT calculations[91] endorse the experimental conclusion. The theoretical studies indicated that if the surfaces or step edges of Ni clusters are too small, the nucleation of filamentous carbon cannot proceed, thus inhibiting coke formation. Based on these investigations, high suppression of carbon formation could be achieved by preparing a catalyst with ultrafine Ni particles (< 6~7 nm) that maintain their particle size during the DRM reaction.

1.4.3. Increasing Ni sintering resistance and thermal stability

In industry, high single-pass conversion of CH_4 and CO_2 is necessary. According to the thermodynamic equilibrium result in **Fig. 1.3b**, the DRM reaction temperature should be above 750 °C to achieve 90% conversion of CH_4 and CO_2. However, the Ni metal is also favorable of thermal sintering due to its low Tammann temperature (~590 °C).[92,93] Such sintering would diminish the catalytic performance due to the decrease in Ni active sites and irreversibly deactivate the catalyst. On the other hand, sintering of originally ultrafine Ni particles to large aggregates would aggravate coke deposition. Therefore, improvement of resistance to Ni sintering is crucial in developing commercially viable Ni catalysts for the DRM process to achieve long-term operation.

Preparing a Ni-based catalyst with strong metal-support interaction (SMSI) can effectively restrain the migration and aggregation of Ni particles. Perovskite, a series of complexes with the formula ABX_3, has been widely applied in catalysis due to its easy preparation, tunable composition, good oxygen mobility, and high stability.[6] $LaNiO_3$ perovskite[5,94–96] can be the precursor to prepare a highly dispersed Ni/La_2O_3 catalyst. This catalyst showed high activity and stability for DRM reaction. The good anti-sintering performance is attributed to the fact that Ni can be partially reduced and remain within the crystal structure. Therefore, Ni/La_2O_3 catalysts from the reduction of $LaNiO_3$ perovskite have strong interaction between Ni and the perovskite structure, suppressing the sintering of Ni. Spinel materials have also been intensively explored for DRM reaction due to their high-temperature stability and strong metal-support interaction. For instance, the $MgAl_2O_4$-supported Ni catalyst[97], which led to the partial insertion of Ni into $MgAl_2O_4$, showed good sintering-resistance compared to Ni/γ-Al_2O_3. The Ni-containing $NiAl_2O_4$ spinel[98–101] also exhibited good resistance to Ni sintering owing to the SMSI. Notably, the reduction of $NiAl_2O_4$ is not easy. That is to say, $NiAl_2O_4$-derived catalysts showed low DRM activity. The SMSI was detected over the catalysts with sandwich structures, in which active metals were firstly supported on a substrate and then coated by another layer of the support substrate, which can effectively inhibit the aggregation of active nanoparticles due to the confinement effect of support. For example, the sandwich-structured Ni/kaolinite catalyst maintains its high DRM catalytic stability at 800 °C for 300 h.[71]

Recently, the encapsulation of Ni particles in rigid support materials to efficiently restrict Ni sintering has drawn much concern. It has been confirmed that the porous support-encapsulated Ni catalyst showed excellent sintering resistance attributed to the spatial confinement effect of the support to the metal nanoparticles to suppress their migration and coalescence and/or strong metal-support interaction.[55,67,102] On this basis, immobilization of ultrafine Ni nanoparticles (NPs) inside various porous materials, such as SiO_2, Al_2O_3, TiO_2, ZrO_2, CeO_2, carbon, zeolite, etc., with core-shell and yolk-shell structure have significantly been explored.[103] These catalysts showed high DRM activity and good coking-/ sintering-resistant abilities. However, as mentioned above, considering the strong endothermicity nature of the DRM reaction, it generally proceeds at relatively high temperatures (>750 °C) to achieve high efficiency. However, most encapsulated Ni catalysts reported to date suffered from the partial structure collapse or phase transformation of the porous support at temperatures higher than 800 °C. This side effect may lead to decreased support surface area, exposure of Ni particles, and thus gradual Ni sintering. Apart from this, such a high temperature would induce chemical transformations of catalytic phases to noncatalytic phases, e.g., the formation of low-active $NiAl_2O_4$ in $Ni@Al_2O_3$[104]. Therefore, encapsulation of Ni NPs inside thermally stable support is fundamental for application at high temperatures.

1.5. Zeolite-encapsulated Ni catalyst (Ni@Zeolite)

Featured by the high thermal stability (especially siliceous zeolites such as Silicalite-1), rigid framework, regular channels, and high specific surface area, zeolite has been a better candidate to confine Ni NPs.[105] In the last two decades, the fixation of the metal particles inside the zeolite crystals to form metal@zeolite structure has been significantly developed in designing a new generation of catalysts.[106–110] As a result, a new class of catalysts with remarkable catalytic performances has been successfully prepared.

Recently, the preparation of metal@zeolite catalysts with more advantages has been intensively investigated. The ion-exchange method is frequently applied and introduces the metal sites into the zeolites. This strategy is based on the existence of guest extra-framework cations (Na^+, NH_4^+, and H^+) located in zeolite channels for charge balancing with negatively charged frameworks of aluminosilicate zeolites. These charge-balancing cations could be exchanged with other metal cations in aqueous solutions. Halliche et al.[111] successfully prepared a series of Ni-exchanged zeolites by ion-exchange method. Among these catalysts, the catalytic performance for DRM reaction was found to vary in the following sequence at 650 °C: NiUSY > NiZSM-5 > NiMOR. However, this method is only applicable to the zeolite with exchangeable extra-framework cations zeolites. For the zeolites with a neutral framework, this method is infeasible. Moreover, the exchanged metal sites may locate inside zeolite channels, and on the external surface, so the distribution of the metal sites is uncontrollable.

Due to capillary force, metal precursors can fill the micropore system by capillary action and thus be distributed within the zeolite matrix. Therefore, the impregnation method, especially the incipient wetness impregnation method, has gained much popularity in preparing Ni@zeolite catalysts. In the early research, Ni NPs were successfully confined within HZSM-5 zeolite via the incipient wetness impregnation method.[112,113] The as-synthesized HZSM-5-encapsulated Ni catalyst (Ni@HZSM-5) exhibited superior catalytic activity in various reactions. Unfortunately, like the ion-exchange method, the incipient wetness impregnation method also cannot control the location of metal species. The random distribution of the metal may lead to metal agglomeration after heat treatment.

Some post-treatment strategies were designed to solve the metal particles on the outer surface of zeolite by the impregnation method. Rasmussen et al.[114] designed an effective two-step dry-gel-conversion synthesis route to prepare Ni@ZSM-5 catalyst with almost Ni NPs enveloped inside the zeolites. Firstly, the as-synthesized meso-ZSM-5 was impregnated with an aqueous solution of $Ni(NO_3)_2$. Then, a nickel-containing ZSM-5 sample ($NiOx$/meso-ZSM-5) was collected after drying and calcination. The NiO_x/meso-ZSM-5 sample was then subjected to steam-assisted recrystallization to grow a shell around the NiO_x/meso-ZSM-5 to obtain a Ni@ZSM-5 catalyst. When the material was applied in catalysis, the Ni@ZSM-5 was a highly active, selective, and stable catalyst for CO_2 methanation.

Xiao and coworkers [66,115] developed the seed-directed growth method. As a typical run, the nickel nanoparticles were loaded onto ZSM-5 seeds through a conventional impregnation method. Next, the resultant Ni/HZSM-5 seed was introduced to the zeolite synthetic gel. The mixture was then transferred into an autoclave and thermally treated at 180 °C for 3 days. After post-synthesis treatments, the Ni@HZSM-5 sample was synthesized. This Ni@HZSM-5 sample showed amazing utilization of CO_2 relative to DRM. In addition, the rigid zeolite framework could minimize coke formation and prevent Ni sintering, outperforming conventional supported metal catalysts prepared by the impregnation method.

The redissolution-recrystallization method is another technique that started from the impregnation method. Ma and coworkers[116] began with impregnating the parent S-1 zeolites into aqueous solutions of $Ni(NO_3)_2.6H_2O$, followed by dissolution-recrystallization with TPAOH solution. Finally, the Ni@S-1 catalyst with high Ni loading (3%-20%) and hollow structure was synthesized. The sizes of Ni NPs maintained at ca. 4–5 nm and its embedded structure also endowed an excellent activity and stability for DRM reaction.

Hydrothermal synthesis (HTS) is a convenient and universal method for preparing metal-containing zeolites. The more desirable method of constructing a metal@zeolite catalyst is the one-pot HTS method, say, direct addition of metal species into the zeolite synthesis mixture. Nonetheless, the one-pot method has presented several problems. Because the hydrothermal synthesis of zeolite generally needs the basic reagent as the mineralizer, the zeolite mother liquor pH is usually greater than 11. In addition, the high temperature (>100 °C) was performed to facilitate the crystallization of zeolite. Most of the metal ions would agglomerate and precipitate very fast under harsh zeolite synthesis conditions because of metal species' high surface free energy. In contrast, the crystallization of zeolites typically takes a much longer time. Therefore, the loss of metal species due to premature precipitation is hard to overcome.[117] To this end, one strategy is to stabilize the metal species with organic ligands[118], e.g., mercapto silane ligands, polyvinyl pyrrolidone (PVP), 3-aminopropyl-trimethoxysilane (APTMS), and ethylenediamine (EN) which strongly coordinate with the metal species to reduce the surface free energy. Spurred by this, Wang et al.[119] mixed nickel nitrate solution and excessive ethylenediamine (>99 %, EN) to acquire $[Ni(EN)_3](NO_3)_2$ mixture in the first step. After that, these ligand-stabilized Ni-containing complexes were added to zeolite mother liquor and subjected to HTS. Finally, the Silicalite-2-encapsulated Ni (Ni@S-2) catalyst was obtained with ultrafine Ni NPs (~2.7 nm). This Ni@S-2 catalyst presented superior DRM activity and stability with no carbon deposition under 650 °C for 50 h. After long-term evaluation, the spent Ni@S-2 catalyst maintained its ultrafine Ni NPs in size, indicating its strong anti-sintering performance. However, Xu et al.[39] observed that the Silicalite-1-encapsulated Ni catalyst (Ni@S-1) prepared by ethylenediamine-protected method showed the incomplete encapsulation of Ni, being prone to deactivation due to the presence of Ni phases on their external surface for DRM reaction. Furthermore, the use of organic ligands would increase the cost.

Another effective way to protect metal species without precipitation during the zeolite formation process is the formation of an amorphous silica sheath around the metal nanoparticles (metal@SiO_2)[120,121]. Then, the metal@SiO_2 was added to the zeolite mother liquor, and the amorphous silica sheath would be crystallized into S-1 zeolite under hydrothermal conditions. Sparked by this, our group successfully developed Pt@S-1[122] and Ni@S-1[123] catalysts from Pt@$SiO_2$and Ni@SiO_2 as the precursor, respectively. These two catalysts showed much better performance than the conventional impregnated Ni catalyst regarding the activity and anti-coking ability for DRM reaction due to the ultrafine metal NPs fixed and maintained within the rigid zeolite framework. Although preparation of Ni@S-1 from Ni@SiO_2 was feasible and active for DRM, it must note that the synthesis of Ni@SiO_2 involves several steps and needs careful control of the synthesis conditions such as the concentration of Ni precursor, organic solvents, ligands, and surfactants as well as temperature, etc.

1.6. Research motivation and objective

It is clear from the above-background review and discussion that dry reforming of methane to produce syngas is of great significance and potential owing to its remarkable environmental and economic value. However, DRM process has yet to be commercially available because of the lack of highly active and long-lived catalysts that can be used on a wide scale. Ni-based catalyst is the most promising candidate for the DRM process due to its high activity and availability. Nevertheless, the major obstacles of Ni catalysts are coking and metal sintering under harsh DRM conditions, which cause the quick and irreversible deactivation of the catalysts.

Researchers have made a great effort and considerable progress in overcoming these limitations. Reportedly, the coke is significantly suppressed on the ultrafine Ni NPs with a size smaller than 7 nm. At the same time, encapsulation of Ni NPs within porous support can achieve high resistance to Ni sintering. Thanks to excellent thermal stability, high surface area, and regular channel, siliceous Silicalite-1 zeolite is an appropriate and widely used support for high-temperature reactions in the presence of steam. Accordingly, fixation of ultrafine Ni NPs (< 7 nm) inside Silicalite-1 zeolite should be a feasible route to realize high DRM activity, good suppression of coke formation, and outstanding resistance to Ni sintering. This strategy provides a viable method for designing a highly active and stable catalyst for DRM reaction. Besides, as mentioned above, our group synthesized a Silicalite-1-encapsulated Ni nanoparticle catalyst using amorphous silica-coated Ni as the precursor. Interestingly, after hydrothermal synthesis, it was confirmed that the needle-like Ni phyllosilicate (Ni-PS) was observed in **Fig. 1.7a** on the primary crystal grain boundary of Silicalite-1 particles (Ni-PS@S-1) and that it was converted to Ni NPs by the reduction process. In other words, Ni-PS was formed and served as the intermediate during the synthesis process.

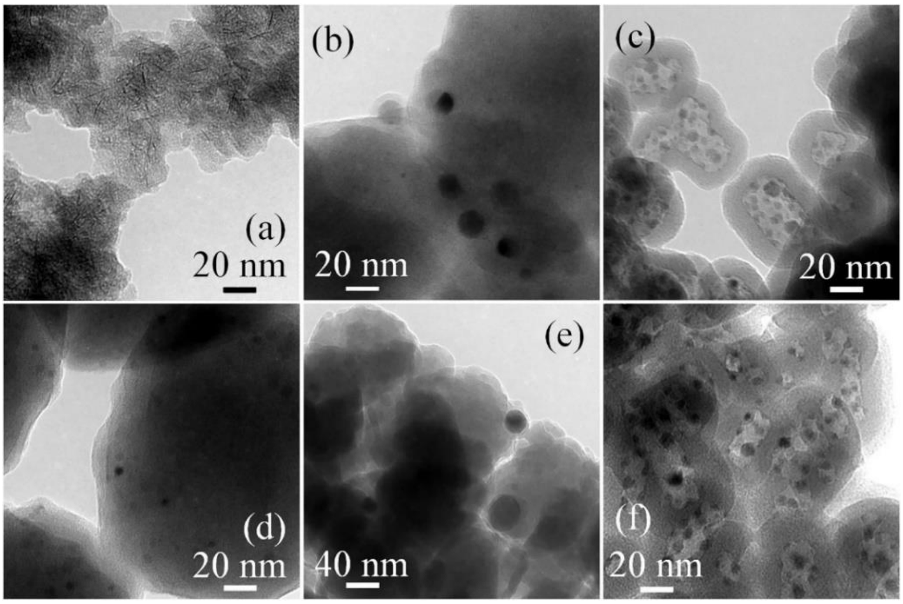

Figure 1.7. TEM images of the prepared Ni-loaded catalysts (a)–(c) before H_2 reduction and (d)–(f) after H_2 reduction at 850 °C for 1 h. ((a) and (d) Ni@Silicalite-1, (b) and (e) Ni/Silicalite-1, and (c) and (f) Ni@SiO_2).[123]

Ni phyllosilicate contains continuous tetrahedral sheets (Si coordinated to four oxygen atoms) and octahedral sheets (Ni coordinated to six oxygen atoms or hydroxyl groups).[124,125] As shown in **Fig. 1.8a**, the tetrahedral sheet is based on interconnected six-member rings of SiO_4^{-4} tetrahedra extending outward in infinite sheets. Each tetrahedra shared three out of the four oxygens with other neighboring tetrahedra. In the octahedral sheet, as illustrated in **Fig. 1.8b**, each octahedron consists of a central nickel cation coordinated with six anions which can be O or OH and connects to adjacent octahedrons by sharing edges. The free corner oxygen atoms of all tetrahedra point to the same side of the sheet and connect to the octahedral sheet to form a common plane in **Fig. 1.8C**.

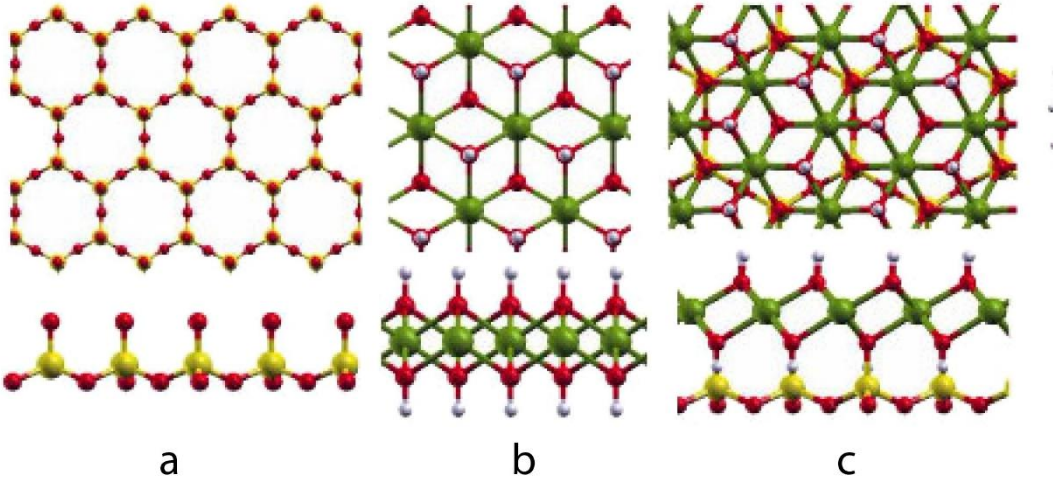

Figure 1.8. top view and side view of (a) tetrahedral SiO_4 sheet, (b) octahedron NiO_6 sheet, (C) tetrahedral SiO_4 sheet connected with octahedron NiO_6 sheet.[124]

Ni-PS was reportedly synthesized under hydrothermal conditions in an alkaline solution.[126,127] More importantly, the formation of needle-like Ni-PS was observed within Silicailte-1 after HTS in our previous work. To bring DRM to a stage where the development of a commercial process can be considered, in this work, we developed Silicalite-1-encapsulated ultrafine Ni NPs catalyst (Ni@S-1) by a new method. In this method, the Ni-PS was synthesized and direct used as Ni source into the zeolite mother liquid, followed by hydrothermal synthesis. The Ni-PS was riveted within the S-1 zeolite, and ultrafine Ni particles were formed in the inter-crystalline pore of the S-1 particle after reduction (Ni@S-1). In addition, the answers of how Ni-PS is converted to Ni@S-1 and what the critical factors in the transformation process are vital for clarifying the formation mechanism and achieving controllable synthesis. Therefore, the investigation of the formation mechanism was also carried out in this thesis. Then, the as-synthesized Ni@S-1 was applied to DRM reaction to evaluate its DRM activity, suppression of coke formation, and resistance to Ni sintering and thermal stability. Furthermore, considering that higher Ni loading is crucial to ensure a higher mass-specific reaction rate in practical DRM process, the attempt to get a Ni@S-1 catalyst with high Ni loading was also done.

1.7. Scope of this thesis

In this thesis, we developed a new method to prepare Ni@S-1 catalyst with encapsulation structure and ultrafine Ni nanoparticles. Firstly, the Ni-PS was synthesized by a simple hydrothermal synthesis method. Then, for the first time, the as-prepared Ni-PS powder was directly used as the Ni source and added into zeolite mother liquor, followed by second hydrothermal treatment. The Ni-PS species were encapsulated within the zeolite particles. After the H_2 reduction, the ultrafine Ni nanoparticles were successfully immobilized in the Silicalite-1 zeolite. We demonstrated the high suppression of coke deposition, good resistance to Ni sintering, and excellent durability of the resulting Ni@S-1 catalyst for DRM reaction. Thus, this work provides a wealth of scientific information on catalyst design to achieve a commercially feasible DRM process.

In **Chapter 2**, the Silicalite-1-encapsulated Ni catalyst (Ni@S-1) with encapsulation structure and ultrafine Ni NPs was prepared using Ni-PS as a Ni source, and its formation mechanism was clarified. Firstly, the 3 wt% Ni-PS was synthesized by the HTS method. Then, the as-prepared 3 wt% Ni-PS was added to the zeolite mother liquor. The resulting mixture was transferred to the autoclave reactor and subjected to different temperatures (100, 150, and 180 °C) and time (1-5 days) treatment. The obtained samples were characterized by different techniques and DRM reaction to detect the morphology, Ni particle size, and Ni location. Accordingly, the formation mechanism and model were proposed.

Chapter 3 compared the optimal Ni@S-1 catalyst with Ni/S-1 prepared by impregnation method and Ni-PS without further transformation to zeolite for DRM reaction. Different characterizations unraveled the structure of these catalysts. Then, the coking suppression for DRM was evaluated at 600 °C, and the sintering resistance and thermal stability were estimated at 850 °C. According to the characterization results and DRM test data, the superiority of Ni@S-1 in terms of suppression of coke formation and resistance to Ni sintering was confirmed.

Chapter 4 focused on preparing Ni@S-1 from Ni-PS with high Ni loading. Firstly, a series of Ni@S-1 samples with Ni loadings of 1, 1.5, 2.0, 2.5, and 3.0 wt% were synthesized, and the preparation conditions were further optimized. Consequently, Ni loading could be increased to 2 wt% without degradation of the catalytic performance. In addition, the poor performance of Ni@S-1 with higher Ni loading, say, > 2 wt.%, was illuminated.

Finally, **Chapter 5** summarized the work of the previous parts and shed light on the tremendous potential of Ni@S-1 from Ni-PS. In addition, it also discussed the possible improvements and prospects for the Ni@S-1 catalyst.

Reference

(1) Rostrup-Nielsen, J. R. New Aspects of Syngas Production and Use. *Catal Today* **2000**, *63* (2–4), 159–164.

(2) Chaouki, G.; Abrar, I. *Sustainable Alternative Syngas Fuel*, IntechOpen.; 2019.

(3) Moulijn, J. A.; Makkee, M.; Diepen, A. E. van. *Chemical Process Technology*, Second edition; WILEY, 2013.

(4) Wilhelm, D. J.; Simbeck, D. R.; Karp, A. D.; Dickenson, R. L. Syngas Production for Gas-to-Liquids Applications: Technologies, Issues and Outlook. *Fuel Processing Technology* **2001**, *71* (1–3), 139–148. 0.

(5) Chen, Y.; Li, M.; Li, Z.; Liu, F.; Song, G.; Kawi, S. Efficient Syngas Production via CO2 Reforming and Electroreduction Reactions through Catalyst Design. *Energy Convers Manag* **2022**, *265*, 115744.

(6) Wang, C.; Wang, Y.; Chen, M.; Liang, D.; Yang, Z.; Cheng, W.; Tang, Z.; Wang, J.; Zhang, H. Recent Advances during CH4 Dry Reforming for Syngas Production: A Mini Review. *Int J Hydrogen Energy* **2021**, *46* (7), 5852–5874..

(7) CHIYODA CORPORATION, Synthesis Gas and Derivatives. https://www.chiyodacorp.com/en/service/gtl/

(8) Casleton, K. H.; Breault, R. W.; Richards, G. A. System Issues and Tradeoffs Associated with Syngas Production and Combustion. *Combustion Science and Technology* **2008**, *180* (6), 1013–1052.

(9) Farniaei, M.; Abbasi, M.; Rahnama, H.; Rahimpour, M. R.; Shariati, A. Syngas Production in a Novel Methane Dry Reformer by Utilizing of Tri-Reforming Process for Energy Supplying: Modeling and Simulation. *J Nat Gas Sci Eng* **2014**, *20*, 132–146.

(10) Taherian, Z.; Khataee, A.; Han, N.; Orooji, Y. Hydrogen Production through Methane Reforming Processes Using Promoted-Ni/Mesoporous Silica: A Review. *Journal of Industrial and Engineering Chemistry* **2022**, *107*, 20–30.

(11) Minh, D. P.; Siang, T. J.; Vo, D. V. N.; Phan, T. S.; Ridart, C.; Nzihou, A.; Grouset, D. Hydrogen Production from Biogas Reforming: An Overview of Steam Reforming, Dry Reforming, Dual Reforming, and Tri-Reforming of Methane. In *Hydrogen Supply Chain: Design, Deployment and Operation*; Elsevier, 2018; pp 111–166.

(12) Frazão, C. J. R.; Walther, T. Syngas and Methanol-Based Biorefinery Concepts. *Chemie Ingenieur Technik* **2020**, *92* (11), 1680–1699.

(13) Tian, P.; Wei, Y.; Ye, M.; Liu, Z. Methanol to Olefins (MTO): From Fundamentals to Commercialization. *ACS Catal* **2015**, *5* (3), 1922–1938.

(14) Rostrup-Nielsen, J. R. Syngas in Perspective. *Catal Today* **2002**, *71* (3–4), 243–247.

(15) Verykios, X. E. Catalytic Dry Reforming of Natural Gas for the Production of Chemicals and Hydrogen. *Int J Hydrogen Energy* **2003**, *28* (10), 1045–1063.

(16) Pei, P.; Korom, S. F.; Ling, K.; Nasah, J. Cost Comparison of Syngas Production from Natural Gas Conversion and Underground Coal Gasification. *Mitig Adapt Strateg Glob Chang* **2016**, *21* (4), 629–643.

(17) Lavoie, J. M. Review on Dry Reforming of Methane, a Potentially More Environmentally Friendly Approach to the Increasing Natural Gas Exploitation. *Front Chem* **2014**, *2* (NOV), 81.

(18) Wang, Y.; Hu, P.; Yang, J.; Zhu, Y. A.; Chen, D. C–H Bond Activation in Light Alkanes: A Theoretical Perspective. *Chem Soc Rev* **2021**, *50* (7), 4299–4358.

(19) Korobitsyn, M. A.; van Berkel, F. P. F.; Christie, G. M. Review of Synthesis Gas Processes. **2000**, December.

(20) Schwach, P.; Pan, X.; Bao, X. Direct Conversion of Methane to Value-Added Chemicals over Heterogeneous Catalysts: Challenges and Prospects. *Chem Rev* **2017**, *117* (13), 8497–8520.

(21) Challiwala, M. S.; Ghouri, M. M.; Linke, P.; El-Halwagi, M. M.; Elbashir, N. O. A Combined Thermo-Kinetic Analysis of Various Methane Reforming Technologies: Comparison with Dry Reforming. *Journal of CO2 Utilization* **2017**, *17*, 99–111.

(22) Rostrup-Nielsen, J. R.; Sehested, J.; Nørskov, J. K. Hydrogen and Synthesis Gas by Steam- and C02 Reforming. *Advances in Catalysis* **2002**, *47*, 65–139.

(23) Al-Fatesh, A.; Singh, S. K.; Kanade, G. S.; Atia, H.; Fakeeha, A. H.; Ibrahim, A. A.; El-Toni, A. M.; Labhasetwar, N. K. Rh Promoted and ZrO2/Al2O3 Supported Ni/Co Based Catalysts: High Activity for CO2 Reforming, Steam–CO2 Reforming and Oxy–CO2 Reforming of CH4. *Int J Hydrogen Energy* **2018**, *43* (27), 12069–12080.

(24) Nguyen, L. Q.; Abella, L. C.; Gallardo, S. M.; Hinode, H. Effect of Nickel Loading on the Activity of Ni/ZrO2 for Methane Steam Reforming at Low Temperature. *Reaction Kinetics and Catalysis Letters* **2008**, *93* (2), 227–232.

(25) Koo, K. Y.; Lee, S. H.; Jung, U. H.; Roh, H. S.; Yoon, W. L. Syngas Production via Combined Steam and Carbon Dioxide Reforming of Methane over Ni–Ce/MgAl2O4 Catalysts with Enhanced Coke Resistance. *Fuel Processing Technology* **2014**, *119*, 151–157.

(26) Taniguchi, T.; Nakasaka, Y.; Yoneta, K.; Tago, T.; Masuda, T. Size-Controlled Synthesis of Metallosilicates with MTW Structure and Catalytic Performance for Methanol-to-Propylene Reaction. *Catal Letters* **2016**, *146* (3), 666–676.

(27) Wang, C.; Fang, W.; Liu, Z.; Wang, L.; Liao, Z.; Yang, Y.; Li, H.; Liu, L.; Zhou, H.; Qin, X.; Xu, S.; Chu, X.; Wang, Y.; Zheng, A.; Xiao, F. S. Fischer–Tropsch Synthesis to Olefins Boosted by MFI Zeolite Nanosheets. *Nature Nanotechnology 2022 17:7* **2022**, *17* (7), 714–720.

(28) Li, J.; He, Y.; Tan, L.; Zhang, P.; Peng, X.; Oruganti, A.; Yang, G.; Abe, H.; Wang, Y.; Tsubaki, N. Integrated Tuneable Synthesis of Liquid Fuels via Fischer–Tropsch Technology. *Nat Catal* **2018**, *1* (10), 787–793.

(29) Pantaleo, G.; Parola, V. la; Deganello, F.; Singha, R. K.; Bal, R.; Venezia, A. M. Ni/CeO2 Catalysts for Methane Partial Oxidation: Synthesis Driven Structural and Catalytic Effects. *Appl Catal B* **2016**, *189*, 233–241.

(30) Vernon, P. D. F.; Green, M. L. H.; Cheetham, A. K.; Ashcroft, A. T. Partial Oxidation of Methane to Synthesis Gas. *Catal Letters* **1990**, *6* (2), 181–186.

(31) Faraday, D. Partial Oxidation of Methane to Synthesis Gas. *Catal Letters* **1990**, *6*, 181–182.

(32) Ruckenstein, E.; Hu, Y. H. Methane Partial Oxidation over NiO/MgO Solid Solution Catalysts. *Appl Catal A Gen* **1999**, *183* (1), 85–92.

(33) York, A. P. E.; Xiao, T.; Green, M. L. H. Brief Overview of the Partial Oxidation of Methane to Synthesis Gas. *Top Catal* **2003**, *22* (3–4), 345–358.

(34) Huang, Q.; Fang, X.; Cheng, Q.; Li, Q.; Xu, X.; Xu, L.; Liu, W.; Gao, Z.; Zhou, W.; Wang, X. Synthesis of a Highly Active and Stable Nickel-Embedded Alumina Catalyst for Methane Dry Reforming: On the Confinement Effects of Alumina Shells for Nickel Nanoparticles. *ChemCatChem* **2017**, *9* (18), 3563–3571.

(35) Er-rbib, H.; Bouallou, C.; Werkoff, F. Dry Reforming of Methane - Review of Feasibility Studies. *Chem Eng Trans* **2012**, *29* (January), 163–168.

(36) Aziz, M. A. A.; Setiabudi, H. D.; Teh, L. P.; Annuar, N. H. R.; Jalil, A. A. A Review of Heterogeneous Catalysts for Syngas Production via Dry Reforming. *J Taiwan Inst Chem Eng* **2019**, *101*, 139–158.

(37) Usman, M.; Wan Daud, W. M. A.; Abbas, H. F. Dry Reforming of Methane: Influence of Process Parameters - A Review. *Renewable and Sustainable Energy Reviews* **2015**, *45*, 710–744.

(38) Li, Y.; Wang, Y.; Zhang, X.; Mi, Z. Thermodynamic Analysis of Autothermal Steam and CO2 Reforming of Methane. *Int J Hydrogen Energy* **2008**, *33* (10), 2507–2514.

(39) Xu, S.; Slater, T. J. A.; Huang, H.; Zhou, Y.; Jiao, Y.; Parlett, C. M. A.; Guan, S.; Chansai, S.; Xu, S.; Wang, X.; Hardacre, C.; Fan, X. Developing Silicalite-1 Encapsulated Ni Nanoparticles as Sintering-/Coking-Resistant Catalysts for Dry Reforming of Methane. *Chemical Engineering Journal* **2022**, *446*, 137439.

(40) Bian, Z.; Kawi, S. Sandwich-Like Silica@Ni@Silica Multicore-Shell Catalyst for the Low-Temperature Dry Reforming of Methane: Confinement Effect Against Carbon Formation. *ChemCatChem* **2018**, *10* (1), 320–328.

(41) Ni, C.; Pan, L.; Yuan, Z.; Cao, L.; Wang, S. Study of Methane Autothermal Reforming Catalyst. *Journal of Rare Earths* **2014**, *32* (2), 184–188.

(42) Zahedi nezhad, M.; Rowshanzamir, S.; Eikani, M. H. Autothermal Reforming of Methane to Synthesis Gas: Modeling and Simulation. *Int J Hydrogen Energy* **2009**, *34* (3), 1292–1300.

(43) Arab Aboosadi, Z.; Jahanmiri, A. H.; Rahimpour, M. R. Optimization of Tri-Reformer Reactor to Produce Synthesis Gas for Methanol Production Using Differential Evolution (DE) Method. *Appl Energy* **2011**, *88* (8), 2691–2701.

(44) Kang, J. S.; Kim, D. H.; Lee, S. D.; Hong, S. I.; Moon, D. J. Nickel-Based Tri-Reforming Catalyst for the Production of Synthesis Gas. *Appl Catal A Gen* **2007**, *332* (1), 153–158.

(45) Soleimani, S.; Lehner, M. Tri-Reforming of Methane: Thermodynamics, Operating Conditions, Reactor Technology and Efficiency Evaluation-A Review. *Energies* **2022**, *15* (19), 7159.

(46) *Glasgow Climate Pact*. https://unfccc.int/

(47) Jafarbegloo, M.; Tarlani, A.; Mesbah, A. W.; Sahebdelfar, S. Thermodynamic Analysis of Carbon Dioxide Reforming of Methane and Its Practical Relevance. *Int J Hydrogen Energy* **2015**, *40* (6), 2445–2451.

(48) Cao, P.; Adegbite, S.; Zhao, H.; Lester, E.; Wu, T. Tuning Dry Reforming of Methane for F-T Syntheses: A Thermodynamic Approach. *Appl Energy* **2018**, *227*, 190–197.

(49) Nikoo, M. K.; Amin, N. A. S. Thermodynamic Analysis of Carbon Dioxide Reforming of Methane in View of Solid Carbon Formation. *Fuel Processing Technology* **2011**, *92* (3), 678–691.

(50) Ginsburg, J. M.; Piña, J.; el Solh, T.; de Lasa, H. I. Coke Formation over a Nickel Catalyst under Methane Dry Reforming Conditions: Thermodynamic and Kinetic Models. *Ind Eng Chem Res* **2005**, *44* (14), 4846–4854.

(51) Zhang, C.; Zhu, W.; Li, S.; Wu, G.; Ma, X.; Wang, X.; Gong, J. Sintering-Resistant Ni-Based Reforming Catalysts Obtained via the Nanoconfinement Effect. *Chemical Communications* **2013**, *49* (82), 9383–9385.

(52) Wang, F.; Han, B.; Zhang, L.; Xu, L.; Yu, H.; Shi, W. CO2 Reforming with Methane over Small-Sized Ni@SiO2 Catalysts with Unique Features of Sintering-Free and Low Carbon. *Appl Catal B* **2018**, *235* (January), 26–35.

(53) Zhang, J.; Li, F. Coke-Resistant Ni@SiO2 Catalyst for Dry Reforming of Methane. *Appl Catal B* **2015**, *176–177*, 513–521.

(54) Kosari, M.; Askari, S.; Seayad, A. M.; Xi, S.; Kawi, S.; Borgna, A.; Zeng, H. C. Strong Coke-Resistivity of Spherical Hollow Ni/SiO2 Catalysts with Shell-Confined High-Content Ni Nanoparticles for Methane Dry Reforming with CO2. *Appl Catal B* **2022**, *310*, 121360.

(55) Li, Z.; Wang, Z.; Kawi, S. Sintering and Coke Resistant Core/Yolk Shell Catalyst for Hydrocarbon Reforming. *ChemCatChem* **2019**, *11* (1), 202–224.

(56) Ayodele, B. v.; Cheng, C. K. Process Modelling, Thermodynamic Analysis and Optimization of Dry Reforming, Partial Oxidation and Auto-Thermal Methane Reforming for Hydrogen and Syngas Production. *Chemical Product and Process Modeling* **2015**, *10* (4), 211–220.

(57) Papadopoulou, C.; Matralis, H.; Verykios, X. Utilization of Biogas as a Renewable Carbon Source: Dry Reforming of Methane. *Catalysis for Alternative Energy Generation* **2012**, 57–127.

(58) Quiroga, M. M. B.; Luna, A. E. C. Kinetic Analysis of Rate Data for Dry Reforming of Methany. *Ind Eng Chem Res* **2007**, *46* (16), 5265–5270.

(59) Sandoval-Bohórquez, V. S.; Morales-Valencia, E. M.; Castillo-Araiza, C. O.; Ballesteros-Rueda, L. M.; Baldovino-Medrano, V. G. Kinetic Assessment of the Dry Reforming of Methane over a Ni-La2O3Catalyst. *ACS Catal* **2021**, *11*, 11478–11493.

(60) Omran, A.; Yoon, S. H.; Khan, M.; Ghouri, M.; Chatla, A.; Elbashir, N. Mechanistic Insights for Dry Reforming of Methane on Cu/Ni Bimetallic Catalysts: DFT-Assisted Microkinetic Analysis for Coke Resistance. *Catalysts 3* **2020**, *10* (9), 1043.

(61) Aramouni, N. A. K.; Touma, J. G.; Tarboush, B. A.; Zeaiter, J.; Ahmad, M. N. Catalyst Design for Dry Reforming of Methane: Analysis Review. *Renewable and Sustainable Energy Reviews* **2018**, *82*, 2570–2585.

(62) Yoon, Y.; You, H. M.; Kim, H. J.; Curnan, M. T.; Kim, K.; Han, J. W. Computational Catalyst Design for Dry Reforming of Methane: A Review. *Energy and Fuels* **2022**, *36* (17), 9844–9865.

(63) Aziz, M. A. A.; Setiabudi, H. D.; Teh, L. P.; Annuar, N. H. R.; Jalil, A. A. A Review of Heterogeneous Catalysts for Syngas Production via Dry Reforming. *J Taiwan Inst Chem Eng* **2019**, *101*, 139–158.

(64) Jang, W.; Shim, J.; Kim, H.; Yoo, S.; Roh, H. A Review on Dry Reforming of Methane in Aspect of Catalytic Properties. *Catal Today* **2019**, *324* (June 2018), 15–26.

(65) Bian, Z.; Das, S.; Wai, M. H.; Hongmanorom, P.; Kawi, S. A Review on Bimetallic Nickel-Based Catalysts for CO2 Reforming of Methane. *ChemPhysChem* **2017**, *18* (22), 3117–3134.

(66) Zhu, Q.; Zhou, H.; Wang, L.; Wang, L.; Wang, C.; Wang, H.; Fang, W.; He, M.; Wu, Q.; Xiao, F.-S. Enhanced CO2 Utilization in Dry Reforming of Methane Achieved through Nickel-Mediated Hydrogen Spillover in Zeolite Crystals. *Nat Catal* **2022**, 5, 1030-1037

(67) Majewski, A. J.; Wood, J.; Bujalski, W. Nickel–Silica Core@shell Catalyst for Methane Reforming. *Int J Hydrogen Energy* **2013**, *38* (34), 14531–14541.

(68) Budiman, A. W.; Song, S. H.; Chang, T. S.; Shin, C. H.; Choi, M. J. Dry Reforming of Methane Over Cobalt Catalysts: A Literature Review of Catalyst Development. *Catalysis Surveys from Asia* **2012**, *16* (4), 183–197.

(69) Benguerba, Y.; Virginie, M.; Dumas, C.; Ernst, B. Methane Dry Reforming over Ni-Co/Al2O3: Kinetic Modelling in a Catalytic Fixed-Bed Reactor. *International Journal of Chemical Reactor Engineering* **2017**, *15* (6).

(70) Horváth; Baán, K.; Varga, E.; Oszkó, A.; Vágó; Törő, M.; Erdőhelyi, A. Dry Reforming of CH4 on Co/Al2O3 Catalysts Reduced at Different Temperatures. *Catal Today* **2017**, *281*, 233–240.

(71) Qu, H.; Yang, H.; Han, L.; He, S.; Liu, J.; Hu, R.; Su, H.; Su, Y. Sandwich-Structured Nickel/Kaolinite Catalyst with Boosted Stability for Dry Reforming of Methane with Carbon Dioxide. *Chemical Engineering Journal* **2023**, *453*, 139694.

(72) Baharudin, L.; Rahmat, N.; Othman, N. H.; Shah, N.; Syed-Hassan, S. S. A. Formation, Control, and Elimination of Carbon on Ni-Based Catalyst during CO2 and CH4 Conversion via Dry Reforming Process: A Review. *Journal of CO2 Utilization* **2022**, *61*, 102050.

(73) Grams, J.; Ruppert, A. M. Catalyst Stability—Bottleneck of Efficient Catalytic Pyrolysis. *Catalysts* **2021**, *11* (2), 265.

(74) Arora, S.; Prasad, R. An Overview on Dry Reforming of Methane: Strategies to Reduce Carbonaceous Deactivation of Catalysts. *RSC Adv* **2016**, *6* (110), 108668–108688.

(75) Argyle, M. D.; Bartholomew, C. H. Heterogeneous Catalyst Deactivation and Regeneration: A Review. *Catalysts* **2015**, *5* (1), 145–269.

(76) Sasson Bitters, J.; He, T.; Nestler, E.; Senanayake, S. D.; Chen, J. G.; Zhang, C. Utilizing Bimetallic Catalysts to Mitigate Coke Formation in Dry Reforming of Methane. *Journal of Energy Chemistry* **2022**, *68*, 124–142.

(77) Duan, X.; Pan, J.; Yang, X.; Wan, C.; Lin, X.; Li, D.; Jiang, L. Nickel–cobalt Bimetallic Catalysts Prepared from Hydrotalcite-like Compounds for Dry Reforming of Methane. *Int J Hydrogen Energy* **2022**, *47* (58), 24358–24373.

(78) Ergazieva, G. E.; Telbayeva, M. M.; Popova, A. N.; Ismagilov, Z. R.; Dossumov, K.; Myltykbayeva, L. K.; Dodonov, V. G.; Sozinov, S. A.; Niyazbayeva, A. I. Effect of Preparation Method on the Activity of Bimetallic Ni-Co/Al2O3 Catalysts for Dry Reforming of Methane. *Chemical Papers* **2021**, *75* (6), 2765–2774.

(79) Liu, X.; Zhang, L.; Zheng, X.; Zhang, Y.; He, D.; Luo, Y. Highly Dispersed Ni/Al2O3 Catalysts for Dry Reforming of Methane Prepared by Alkaline-Induced Adsorption Process. *Int J Hydrogen Energy* **2022**, *47* (72), 30937–30949.

(80) Choudhary, V. R.; Rajput, A. M.; Mamman, A. S. NiO-Alkaline Earth Oxide Catalysts for Oxidative Methane-to-Syngas Conversion: Influence of Alkaline Earth Oxide on the Surface Properties and Temperature-Programmed Reduction/Reaction by H2 and Methane. *J Catal* **1998**, *178* (2), 576–585.

(81) Delir Kheyrollahi Nezhad, P.; Bekheet, M. F.; Bonmassar, N.; Gili, A.; Kamutzki, F.; Gurlo, A.; Doran, A.; Schwarz, S.; Bernardi, J.; Praetz, S.; Niaei, A.; Farzi, A.; Penner, S. Elucidating the Role of Earth Alkaline Doping in Perovskite-Based Methane Dry Reforming Catalysts. *Catal Sci Technol* **2022**.

(82) Araiza, D. G.; Gómez-Cortés, A.; Díaz, G. Effect of Ceria Morphology on the Carbon Deposition during Steam Reforming of Ethanol over Ni/CeO2 Catalysts. *Catal Today* **2020**, *349*, 235–243.

(83) Ang, M. L.; Oemar, U.; Saw, E. T.; Mo, L.; Kathiraser, Y.; Chia, B. H.; Kawi, S. Highly Active Ni/XNa/CeO2 catalyst for the Water-Gas Shift Reaction: Effect of Sodium on Methane Suppression. *ACS Catal* **2014**, *4* (9), 3237–3248.

(84) Wang, Y.; Zhang, R.; Yan, B. Ni/Ce0.9Eu0.1O1.95 with Enhanced Coke Resistance for Dry Reforming of Methane. *J Catal* **2022**, *407*, 77–89.

(85) Teh, L. P.; Setiabudi, H. D.; Timmiati, S. N.; Aziz, M. A. A.; Annuar, N. H. R.; Ruslan, N. N. Recent Progress in Ceria-Based Catalysts for the Dry Reforming of Methane: A Review. *Chem Eng Sci* **2021**, *242*, 116606.

(86) Jin, B.; Li, S.; Liu, Y.; Liang, X. Engineering Metal-Oxide Interface by Depositing ZrO2 Overcoating on Ni/Al2O3 for Dry Reforming of Methane. *Chemical Engineering Journal* **2022**, *436*, 135195.

(87) Rosdin, R. D. binti; Yusuf, M.; Abdullah, B. Dry Reforming of Methane over Ni-Based Catalysts: Effect of ZrO2 and MgO Addition as Support. *Mater Lett* **2021**, *12*, 100095.

(88) Meiliefiana, M.; Nakayashiki, T.; Yamamoto, E.; Hayashi, K.; Ohtani, M.; Kobiro, K. One-Step Solvothermal Synthesis of Ni Nanoparticle Catalysts Embedded in ZrO2 Porous Spheres to Suppress Carbon Deposition in Low-Temperature Dry Reforming of Methane. *Nanoscale Research Letters* **2022**, *17* (1), 1–12.

(89) Kim, J. H.; Suh, D. J.; Park, T. J.; Kim, K. L. Effect of Metal Particle Size on Coking during CO2 Reforming of CH4 over Ni–Alumina Aerogel Catalysts. *Appl Catal A Gen* **2000**, *197* (2), 191–200.

(90) Osojnik Črnivec, I. G.; Djinović, P.; Erjavec, B.; Pintar, A. Effect of Synthesis Parameters on Morphology and Activity of Bimetallic Catalysts in CO2–CH4 Reforming. *Chemical Engineering Journal* **2012**, *207–208*, 299–307.

(91) Bengaard, H. S.; Nørskov, J. K.; Sehested, J.; Clausen, B. S.; Nielsen, L. P.; Molenbroek, A. M.; Rostrup-Nielsen, J. R. Steam Reforming and Graphite Formation on Ni Catalysts. *J Catal* **2002**, *209* (2), 365–384.

(92) Trimm, D. L. Catalysts for the Control of Coking during Steam Reforming. *Catal Today* **1999**, *49* (1–3), 3–10.

(93) Xu, L.; Wang, F.; Chen, M.; Yang, H.; Nie, D.; Qi, L.; Lian, X. Alkaline-Promoted Ni Based Ordered Mesoporous Catalysts with Enhanced Low-Temperature Catalytic Activity toward CO 2 Methanation. *RSC Adv* **2017**, *7* (30), 18199–18210.

(94) Salaev, M. A.; Liotta, L. F.; Vodyankina, O. v. Lanthanoid-Containing Ni-Based Catalysts for Dry Reforming of Methane: A Review. *Int J Hydrogen Energy* **2022**, *47* (7), 4489–4535.

(95) Batiot-Dupeyrat, C.; Gallego, G. A. S.; Mondragon, F.; Barrault, J.; Tatibouët, J. M. CO2 Reforming of Methane over LaNiO3 as Precursor Material. *Catal Today* **2005**, *107–108*, 474–480.

(96) Bonmassar, N.; Bekheet, M. F.; Schlicker, L.; Gili, A.; Gurlo, A.; Doran, A.; Gao, Y.; Heggen, M.; Bernardi, J.; Klötzer, B.; Penner, S. In Situ-Determined Catalytically Active State of LaNiO3 in Methane Dry Reforming. *ACS Catal* **2020**, *10* (2), 1102–1112.

(97) Guo, J.; Lou, H.; Zhao, H.; Chai, D.; Zheng, X. Dry Reforming of Methane over Nickel Catalysts Supported on Magnesium Aluminate Spinels. *Appl Catal A Gen* **2004**, *273* (1–2), 75–82.

(98) Littlewood, P.; Liu, S.; Weitz, E.; Marks, T. J.; Stair, P. C. Ni-Alumina Dry Reforming Catalysts: Atomic Layer Deposition and the Issue of Ni Aluminate. *Catal Today* **2020**, *343*, 18–25.

(99) Karam, L.; Reboul, J.; el Hassan, N.; Nelayah, J.; Massiani, P. Nanostructured Nickel Aluminate as a Key Intermediate for the Production of Highly Dispersed and Stable Nickel Nanoparticles Supported within Mesoporous Alumina for Dry Reforming of Methane. *Molecules* **2019**, *24* (22), 4107.

(100) Zhou, L.; Li, L.; Wei, N.; Li, J.; Basset, J. M. Effect of NiAl2O4 Formation on Ni/Al2O3 Stability during Dry Reforming of Methane. *ChemCatChem* **2015**, *7* (16), 2508–2516.

(101) Aghaali, M. H.; Firoozi, S. Enhancing the Catalytic Performance of Co Substituted NiAl2O4 Spinel by Ultrasonic Spray Pyrolysis Method for Steam and Dry Reforming of Methane. *Int J Hydrogen Energy* **2021**, *46* (1), 357–373.

(102) Li, Z.; Li, M.; Bian, Z.; Kathiraser, Y.; Kawi, S. Design of Highly Stable and Selective Core/Yolk–Shell Nanocatalysts—A Review. *Appl Catal B* **2016**, *188*, 324–341.

(103) Gao, C.; Lyu, F.; Yin, Y. Encapsulated Metal Nanoparticles for Catalysis. *Chem Rev* **2020**.

(104) Han, J. W.; Park, J. S.; Choi, M. S.; Lee, H. Uncoupling the Size and Support Effects of Ni Catalysts for Dry Reforming of Methane. *Appl Catal B* **2017**, *203*, 625–632.

(105) Wang, L.; Xu, S.; He, S.; Xiao, F. Rational Construction of Metal Nanoparticles Fixed in Zeolite Crystals as Highly Efficient Heterogeneous Catalysts. *Nano Today* **2018**, *20*, 74–83.

(106) Hauberg, K. Novel Methods for Synthesis of Zeolites and Zeolite-Encapsulated Metal Particles, Technical University of Denmark, 2020.

(107) Wu, S.; Yang, X.; Janiak, C. Confinement Effects in Zeolite-Confined Noble Metals. *Angewandte Chemie* **2019**, *131* (36), 12468–12482.

(108) Cui, W. G.; Li, Y. T.; Yu, L.; Zhang, H.; Hu, T. L. Zeolite-Encapsulated Ultrasmall Cu/ZnOx Nanoparticles for the Hydrogenation of CO2 to Methanol. *ACS Appl Mater Interfaces* **2021**, *13* (16), 18693–18703.

(109) Limlamthong, M.; Yip, A. C. K. Recent Advances in Zeolite-Encapsulated Metal Catalysts: A Suitable Catalyst Design for Catalytic Biomass Conversion. *Bioresource Technology* **2020**, *297*, 122488.

(110) Zhang, Q.; Gao, S.; Yu, J. Metal Sites in Zeolites: Synthesis, Characterization, and Catalysis. *Chemical Reviews*. **2022**.

(111) Halliche, D.; Cherifi, O.; Taarit, Y. B.; Auroux, A. Catalytic Reforming of Methane by Carbon Dioxide over Nickel-Exchanged Zeolite Catalysts. *Kinetics and Catalysis* **2008**, *49* (5), 667–675.

(112) Li, W.; Wang, H.; Wu, X.; Betancourt, L. E.; Tu, C.; Liao, M.; Cui, X.; Li, F.; Zheng, J.; Li, R. Ni/Hierarchical ZSM-5 Zeolites as Promising Systems for Phenolic Bio-Oil Upgrading: Guaiacol Hydrodeoxygenation. *Fuel* **2020**, *274*, 117859.

(113) Ren, X. Y.; Cao, J. P.; Zhao, S. X.; Zhao, X. Y.; Liu, T. L.; Feng, X. B.; Li, Y.; Zhang, J.; Bai, H. C. Encapsulation Ni in HZSM-5 for Catalytic Hydropyrolysis of Biomass to Light Aromatics. *Fuel Processing Technology* **2021**, *218*, 106854.

(114) Rasmussen, K. H.; Goodarzi, F.; Christensen, D. B.; Mielby, J.; Kegnæs, S. Stabilization of Metal Nanoparticle Catalysts via Encapsulation in Mesoporous Zeolites by Steam-Assisted Recrystallization. *ACS Appl Nano Mater* **2019**, *2* (12), 8083–8091.

(115) Zhang, J.; Wang, L.; Zhang, B.; Zhao, H.; Kolb, U.; Zhu, Y.; Liu, L.; Han, Y.; Wang, G.; Wang, C.; Su, D. S.; Gates, B. C.; Xiao, F. S. Sinter-Resistant Metal Nanoparticle Catalysts Achieved by Immobilization within Zeolite Crystals via Seed-Directed Growth. *Nat Catal* **2018**, *1* (7), 540–546.

(116) Liu, Y.; Chen, Y.; Gao, Z.; Zhang, X.; Zhang, L.; Wang, M.; Chen, B.; Diao, Y.; Li, Y.; Xiao, D.; Wang, X.; Ma, D.; Shi, C. Embedding High Loading and Uniform Ni Nanoparticles into Silicalite-1 Zeolite for Dry Reforming of Methane. *Appl Catal B* **2022**, *307*.

(117) Zhu, J.; Osuga, R.; Ishikawa, R.; Shibata, N.; Ikuhara, Y.; Kondo, J. N.; Ogura, M.; Yu, J.; Wakihara, T.; Liu, Z.; Okubo, T. Ultrafast Encapsulation of Metal Nanoclusters into MFI Zeolite in the Course of Its Crystallization: Catalytic Application for Propane Dehydrogenation. *Angewandte Chemie - International Edition* **2020**, *59* (44), 19669–19674.

(118) Chai, Y.; Shang, W.; Li, W.; Wu, G.; Dai, W.; Guan, N.; Li, L. Noble Metal Particles Confined in Zeolites: Synthesis, Characterization, and Applications. *Advanced Science* **2019**, *6* (16).

(119) Wang, J.; Fu, Y.; Kong, W.; Jin, F.; Bai, J.; Zhang, J.; Sun, Y. Design of a Carbon-Resistant Ni@S-2 Reforming Catalyst: Controllable Ni Nanoparticles Sandwiched in a Peasecod-like Structure. *Appl Catal B* **2021**, *282* .

(120) Meng, X.; Wu, Q.; Chen, F.; Xiao, F.-S. Solvent-Free Synthesis of Zeolite Catalysts. *Science China Chemistry* **2014**, *58* (1), 6–13.

(121) Wu, Q.; Meng, X.; Gao, X.; Xiao, F.-S. Solvent-Free Synthesis of Zeolites: Mechanism and Utility. *Acc Chem Res* **2018**, *51* (6), 1396–1403.

(122) Kobayashi, T.; Furuya, T.; Fujitsuka, H.; Tago, T. Synthesis of Birdcage-Type Zeolite Encapsulating Ultrafine Pt Nanoparticles and Its Application in Dry Reforming of Methane. *Chemical Engineering Journal* **2019**, *377*, 120203.

(123) Fujitsuka, H.; Kobayashi, T.; Tago, T. Development of Silicalite-1-Encapsulated Ni Nanoparticle Catalyst from Amorphous Silica-Coated Ni for Dry Reforming of Methane: Achieving Coke Formation Suppression and High Thermal Stability. *Journal of CO2 Utilization* **2021**, *53*, 101707.

(124) Duarte, H. A.; Lourenço, M. P.; Heine, T.; Guimarães, L.; Duarte, H. A.; Lourenço, M. P.; Heine, T.; Guimarães, L. Clay Mineral Nanotubes: Stability, Structure and Properties. *Stoichiometry and Materials Science* **2012**.

(125) Bian, Z.; Kawi, S. Preparation, Characterization and Catalytic Application of Phyllosilicate: A Review. *Catal Today* **2018**, *339,*3-23.

(126) Sivaiah, M. v.; Petit, S.; Barrault, J.; Batiot-Dupeyrat, C.; Valange, S. CO2 Reforming of CH4 over Ni-Containing Phyllosilicates as Catalyst Precursors. *Catal Today* **2010**, *157* (1–4), 397–403.

(127) Sivaiah, M. v.; Petit, S.; Beaufort, M. F.; Eyidi, D.; Barrault, J.; Batiot-Dupeyrat, C.; Valange, S. Nickel Based Catalysts Derived from Hydrothermally Synthesized 1:1 and 2:1 Phyllosilicates as Precursors for Carbon Dioxide Reforming of Methane. *Microporous and Mesoporous Materials* **2011**, *140* (1–3), 69–80.

Chapter 2. Preparation of Ni@S-1 catalyst from Ni-PS and investigation of the formation mechanism

2.1. Introduction

Dry (CO_2) reforming of methane (DRM) provides an efficient way to consume and convert two leading greenhouse gases, CH_4 + CO_2, into syngas (CO and H_2).[1–3] Therefore, the industrial application of DRM reaction possesses excellent environmental and economic potential.

The Nickel (Ni) based catalysts are believed to be the most promising for DRM reaction.[4–6] However, the Ni-loaded catalyst prepared by the conventional impregnation method cannot meet the commercial requirement because of the severe Ni sintering and coke deposition under harsh DRM conditions, which would lead to the fast deactivation of the catalyst.[7–9]

It has been confirmed that encapsulation of ultrafine Ni NPs (< 7 nm) within porous support could effectively suppress coke formation and be resistant to Ni sintering during the DRM process.[10–13] Accordingly, our group successfully prepared Silicalite-1-encapsulated Ni catalyst (Ni@S-1) using amorphous silica-encapsulated Ni-oxide ($NiO_x@SiO_2$) as the Ni precursor.[14] This $NiO_x@SiO_2$ was first formed in the microemulsion solution, followed by adding the powdery $NiO_x@SiO_2$ into zeolite mother liquor. After hydrothermal synthesis (HTS), it was confirmed that the needle-like Ni phyllosilicate (Ni-PS) was formed on the primary crystal grain boundary of Silicalite-1 particles (Ni-PS@S-1) and that it was converted to Ni NPs by the reduction process. Thus, the Ni@S-1 catalyst exhibited high DRM activity with excellent inhibition of carbon deposition and high thermal stability due to the immobilization of ultrafine Ni particles within the thermally stable Silicalite-1. Ni-PS was reportedly synthesized under hydrothermal conditions in an alkaline solution.[9,15–17]

Hence, this chapter explored and developed a new preparation method for encapsulating ultrafine Ni nanoparticles in Silicalite-1 zeolite using Ni-PS as the Ni source. Furthermore, transforming Ni-PS into Ni@S-1 by hydrothermal synthesis is a rather complicated process involving a variety of possible mechanisms. It can be described in briefest terms as follows: the hydrolysis and condensation of the raw materials, nucleation, and crystal growth steps. Therefore, clarification of the formation mechanism of Ni@S-1 catalyst from Ni-PS plays a significant role in the controllable synthesis of Ni@S-1 with desired structure and catalytic performances. Many variables affect the zeolite morphology, crystal size distribution, and heteroatom location. These parameters include composition-dependent parameters (reactant mixture concentration, pH, and the ratio between framework-forming elements), the crystallization time, and synthesis temperature.[18,19] Thus, this chapter also studied the appropriate preparation conditions and formation mechanism by varying different synthesis parameters, such as the water-to-silica ratio (reactant mixture concentration), crystallization time, and crystallization temperature.

2.2. Experimental

2.2.1. Chemicals

Nickel (II) nitrate hexahydrate ($Ni(NO_3)_2.6H_2O$, > 99%), ammonia solution (> 28 wt.%), tetraethyl orthosilicate (TEOS, > 95.0%,), tetrapropylammonium hydroxide aqueous solution (TPAOH, 10% in H_2O), and distilled water were purchased from

FUJIFILM Wako Pure Chemical Industries, Ltd., Japan. In this study, all chemicals were purchased commercially without further purification. Distilled water was used throughout the experiment.

2.2.2. Catalyst Preparation

The Ni@S-1 catalysts with theoretical Ni loading of 1 wt% were prepared by a two-step method. Firstly, as shown in **Fig. 2.1**, 3 wt% Ni-PS/SiO_2 was prepared by hydrothermal synthesis. Then, the 1 wt% Ni@S-1 catalyst was prepared using the as-synthesized 3 wt.% Ni-PS/SiO_2 as the precursor by second hydrothermal treatment.

Step 1. Preparation of 3 wt% Ni-PS/SiO_2 by HTS method

Table 2.1. Preparation conditions of 3wt% Ni-PS/SiO_2

Parameter	Theoretical value
Ni loading	3 wt%
H_2O/Si	34 mol/mol
NH_3/Ni	60 mol/mol
HTS temperature	100 °C
HTS time	3 d

1) added calculated amounts of 1M of $Ni(NO_3)_2$ aqueous solution to diluted 3.0 M of ammonia solution to form the nickel ammonia complex solution.

2) Si source, TEOS, was added to the above nickel ammonia complex solution and stirring for 2 h.

3) transferred the mixture into Teflon-lined autoclave reactor and hydrothermal treated at 100 °C for three days.

4) washed samples with distilled water three times and recovered the samples by centrifugation.

5) dried at 110 °C overnight.

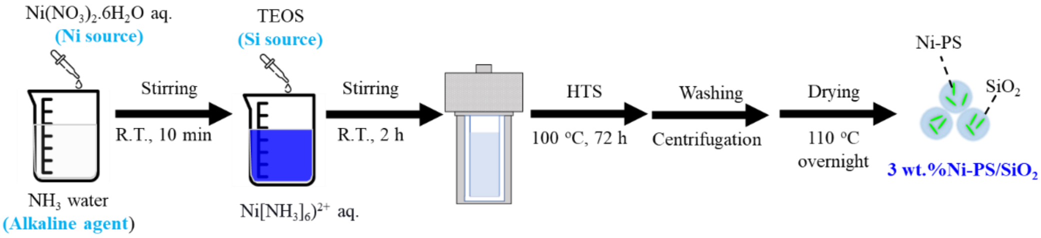

Figure 2.1. Preparation procedures of 3 wt.% Ni-PS/SiO_2

Step 2. Preparation of 1 wt% Ni@S-1 catalyst using the as-prepared 3 wt% Ni-PS/SiO_2 as the Ni source by HTS method

Then, the Silicalite-1-encapsulated Ni nanoparticle catalysts were prepared under different hydrothermal conditions to determine the appropriate synthesis conditions and investigate the formation mechanism. The preparation procedures and conditions are shown in the below and **Fig. 2.2**.

1) preparation of zeolite mother liquor by mixing calculated amounts of TEOS, TPAOH, and distilled water at room temperature for 24 h to form a homogenous gel.

2) added designated amount of the 3 wt.% Ni-PS/SiO_2 precursor to the zeolite mother liquor and stirring for 2 h.

3) transferred into a Teflon-sealed autoclave and hydrothermally treated at 100 °C for different time in a tumbling oven.

4) washed samples with distilled water three times and recovered the samples by centrifugation.

5) drying at 110 °C overnight and calcined at 550 °C for 12 h.

6) reduced in 50 vol% H_2 at 850 °C for 1 h.

Table 2.2. Preparation conditions of study on effect of H_2O/SiO_2 ratio

Parameter	Theoretical value
Ni loading	1 wt%
Si/TPAOH	3 mol/mol
Si_{PS}/Si_{TEOS}	0.49 mol/mol
H_2O/Si	**34, 50, and 100 mol/mol**
Volume of zeolite mother liquor	75 mL (100 mL of autoclave reactor)
HTS temperature	100 °C
HTS time	3 d

Table 2.3. Preparation conditions of study on effect of HTS time

Parameter	Theoretical value
Ni loading	1 wt%
Si/TPAOH	3 mol/mol
Si_{PS}/Si_{TEOS}	0.49 mol/mol
H_2O/Si	50 mol/mol
Volume of zeolite mother liquor	75 mL (100 mL of autoclave reactor)
HTS temperature	100 °C
HTS time	**1d, 2d, 3d, 5d, and 7d**

Table 2.4. Preparation conditions of study on effect of HTS temperature

Parameter	Theoretical value
Ni loading	1 wt%
Si/TPAOH	3 mol/mol
Si_{PS}/Si_{TEOS}	0.49 mol/mol
H_2O/Si	50 mol/mol
Zeolite mother liquor volume	75 mL (100 mL of autoclave reactor)
HTS temperature	**100, 150, and 180 °C**
HTS time	3 d

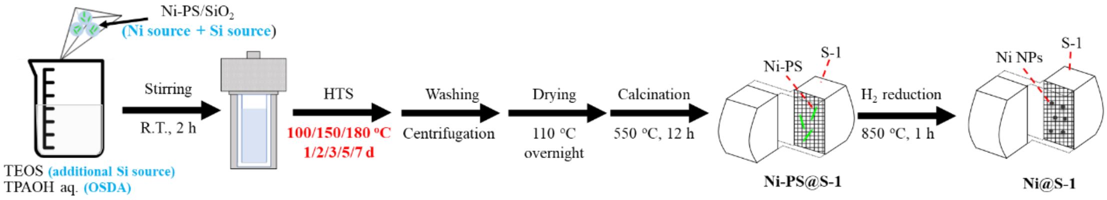

Figure 2.2. Preparation procedures of Ni@S-1

2.2.3 Catalyst Characterization

The characterization methods and corresponding acquired information are listed in **Table 2.5**. The detailed measurement conditions are shown below.

The Ni loading of the as-synthesized samples was detected by X-ray fluorescence (XRF, Supermini, Rigaku Co., Ltd., Japan). The crystallinity and phase identification were evaluated using X-ray diffraction (XRD, SmartLab, Rigaku Co., Ltd., Japan) with Cu Kα radiation (λ =0.154 nm), operating at 30 kV and 10 mA, a scanning rate of 4°/min, and a step size of 0.02°. Diffraction peaks were recorded in a 2θ range of 5–60°.

The morphology of the samples was observed by a field-emission scanning electron microscope (FE-SEM, S-5200, Hitachi Ltd., Japan) with an acceleration voltage of 1 kV. The shape and size of the Ni species in the prepared samples were observed using a field-emission transmission electron microscope (FE-TEM, H-7650 Zero A, Hitachi Ltd., Japan) operated at an acceleration voltage of 120 kV.

The porosity of the catalysts was studied via the nitrogen adsorption-desorption isotherms (BELSORP mini X, Microtrac MRB, USA) at 77 K. The specific surface area was analyzed using Brunauer-Emmett-Teller (BET) method. The micropore volume and mesopore volume were calculated by the t-plot method and BJH method, respectively.

The redox property of the samples was measured by H_2-temperature programmed reduction (H_2-TPR). The measurement was carried out using a fixed-bed reactor equipped with a mass spectrometer (BELMASS, MicrotracBEL, Inc., Japan). Typically, 0.4 g of the shaped sample was pre-calcined in the air at 400 °C for 1 h and then cooled down in Ar stream to 100°C. After the temperature was maintained for 90 min, the gas stream was switched to 5% H_2/Ar gas. Subsequently, the sample was heated from 100 to 900 °C at a ramping rate of 10°C/min and then held there for 1 h. The hydrogen consumption and reduction temperature of the Ni species were estimated by the decrease in the intensity of m/z =2 of the mass spectrometer.

Finally, the amount of carbon deposition on the spent catalysts was analyzed by the Thermogravimetric analysis (TG-DTA, TG 8120, Rigaku Co., Ltd., Japan). The spent catalyst sample was heated in the air (100 mL/min) at a ramp rate of 10 °C/min to 900 °C and kept for 1 h.

Table 2.5. Characterization techniques and corresponding acquired information

Characterization	Acquired information
XRF	Ni loading
XRD	Crystallographic information
SEM	Catalyst morphology
TEM	Ni NPs location and size, and carbon formation
N_2-sorption	Porosity, surface area, and pore volume
H_2-TPR	The reducibility of Ni
TG-DTA	Coke content

2.2.4 Catalytic Performance Evaluation

The catalytic performances and Ni location of the prepared catalysts were evaluated by DRM reaction at 600 °C in a down-flow fixed bed reactor. The schematic diagram of the DRM apparatus is cartooned in **Fig. 2.3**. The evaluation conditions are listed in **Table 2.6**.

Typically, 270 mg of the pelleted Ni@S-1 catalyst with the size of 300-600μm (or 90 mg of 3 wt% Ni-PS mixed with quartz sand) was packed into a quartz tube reactor and then reduced in 60 mL/min of 50 vol.% H_2/N_2 at 850 °C for 1 h. Subsequently, adjusting the system to 600 °C in the N_2 stream and then subject to 80 mL/min of the reaction gas (CH_4: CO_2: Ar = 20: 20:40 mL/min) and 10 mL/min of He gas (functioned as internal standard gas) into the reactor. The gas hourly space velocity (GHSV) was calculated on the mass basis of nickel contained in the catalysts and was fixed at 2,000 L/g-Ni/h for each evaluation.

The effluent gases analysis was carried out using online gas chromatographs (GC-8A, Shimadzu Co., Ltd., Japan) equipped with an active carbon column connected to a thermal conductivity detector (TCD). The CH_4, CO_2, H_2, CO, and He gases were detected in all the experiments. The conversion of methane (X_{CH4}), CO_2 (X_{CO2}), the H_2/CO molar ratio, and carbon balance were defined as follows:

$$X_{CH4}\ (\%) = (1 - F_{CH4,out}/\ F_{CH4,in}) \times 100\%$$

$$X_{CO2}\ (\%) = (1 - F_{CO2,out}/\ F_{CO2,in})\ \times 100\%$$

$$H_2/CO = F_{H2\text{-}out}/\ F_{CO\text{-}out}$$

$$\text{Gaseous carbon recovery (\%)} = \frac{F_{CO-out} + F_{CH4-out} + F_{CO2-out}}{F_{CH4-in} + F_{CO2-in}} \times 100\%$$

Table 2.6. Catalytic evaluation conditions for the DRM reaction

Pressure	1 bar
H_2 reduction	60 mL/min of 50 vol.% H_2/N_2, 850°C, 1h
DRM temperature	600 °C
Reactant gas	CH_4: CO_2: Ar: He = 20: 20: 40: 10 mL/min
GHSV	2,000 L/g-Ni/h.

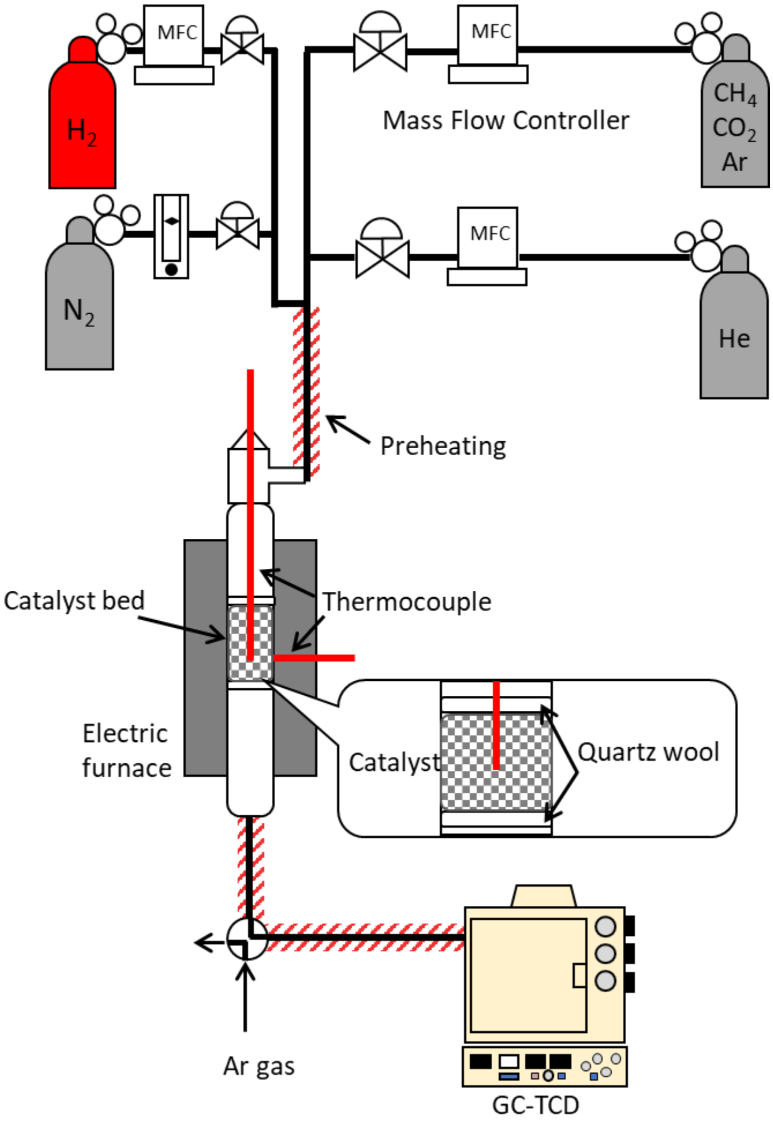

Figure 2.3. Schematic of DRM apparatus

2.3. Effect of H_2O/SiO_2 ratio

It is apparent that the water content alters and determines the concentration and supersaturation of the reactant mixture and alkalinity of the zeolite mother liquor. Thus, it significantly affects the hydrolysis, nucleation, and crystallization processes, resulting in zeolite formation with different morphologies and properties.

2.3.1. Catalyst characterization

As first, the collected Ni phyllosilicate was measured by various characterization techniques to verify the feasibility of the preparation method and the state and structure of the obtained sample. As shown in **Fig. 2.4a**, the needle-like Ni-PS species with a length of ca. 10 nm and a width of ca. 2nm were observed by TEM. Additionally, the H_2-TPR profile in **Fig. 2.4b** shows that the H_2 reduction peak at 650 °C was ascribed to the reduction of 1:1 Ni-PS to Ni^0.[16,20] This reduction temperature was higher than 550 °C of reduction of NiO to Ni^0 due to formation of strong -Ni-O-Si- chemical bond in the Ni-PS structure.[21,22] The actual Ni loading measured by XRF listed in the **Table 2.7** was 3.01 wt%, which is equal to the theoretical value, suggesting no nickel loss during the preparation. The XRD and N_2-physisorption results verify that the obtained sample was the non-porous amorphous silica with high dispersion of Ni species. These characterization results verified that the Ni-PS was successfully formed by the simple HTS method. Then, the obtained 3 wt.% Ni-PS/SiO_2 powder was added to zeolite mother liquor with different H_2O/SiO_2 ratios and hydrothermally treated at 100 °C for three days to prepare 1 wt% Ni@S-1 catalyst.

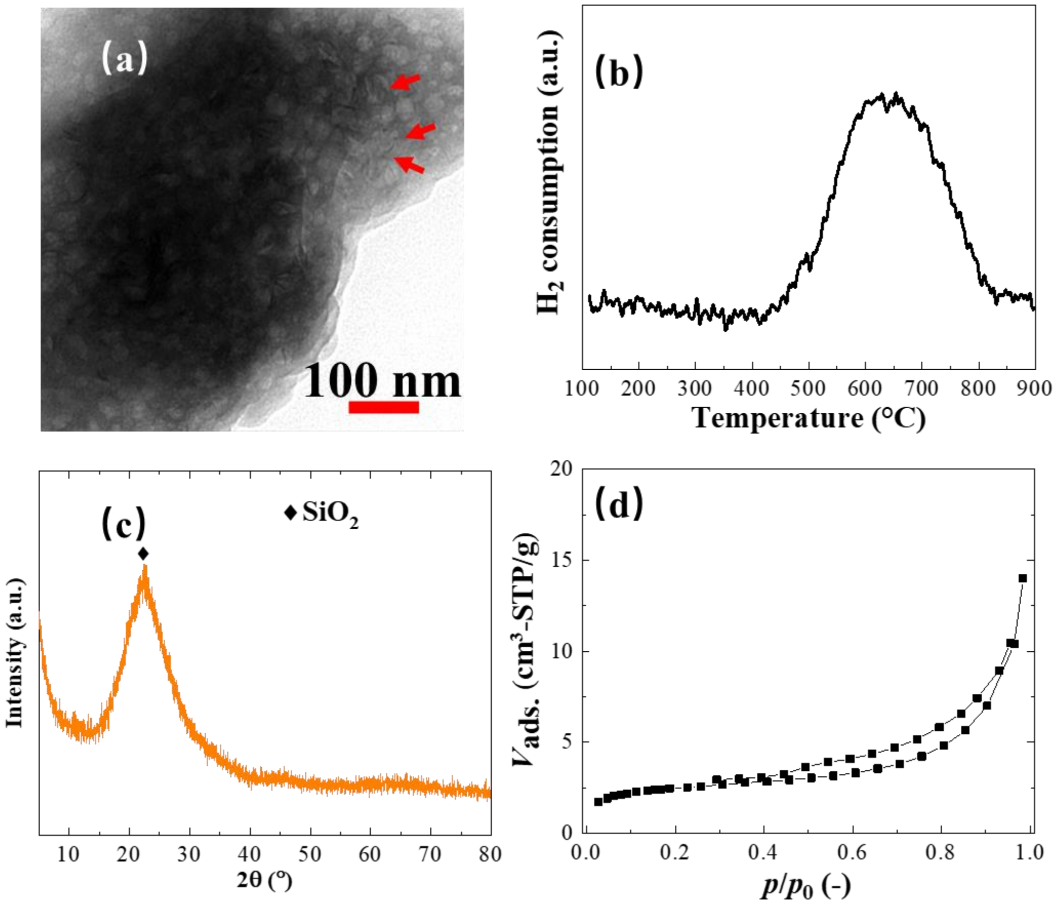

Figure 2.4. The characterization results of the as-prepared 3 wt.% Ni-PS/SiO_2: (a) TEM image, (b) H_2-TPR profile, (c) XRD pattern, and (d) N_2-physisorption isotherms.

Table 2.7. Properties of the as-prepared samples after H_2-reduction at 850 °C for 1 h.

Sample	Ni loading[a] (wt%)	S_{BET}[b] (m^2/g)	V_{micro}[c] (cm^3/g)
3 wt% Ni-PS/SiO_2	3.01	9.3	0.002

[a] Measured by XRF

[b]. Calculated by BET equation.

[c]. Calculated by t-plot method.

The compositions of zeolite mother liquor to prepare Ni@S-1 catalyst were listed in **Table 2.8.** As can be seen, the zeolite synthesis with lower water content had a higher alkalinity and reactant concentration. As measured by XRF, compared to the samples from the higher H_2O/SiO_2 ratios, the Ni loading was 0.93 wt% for the sample prepared with H_2O/SiO_2 ratio of 34. This value was lower than the nominal value, 1 wt%. The Ni loss may be because the higher alkalinity of the synthetic mixture in the case of low water content increased the solubility of the reactants, which leads to more nickel species dissolved in water.

The XRD patterns in **Fig. 2.5** confirmed that the high crystalline Silicalite-1 zeolites were synthesized in all the cases after hydrothermal treatment. The relative crystallinities of the as-prepared samples were 92.4%, 105.3, and 117.4 for Ni@S-1-34, Ni@S-1-50, and Ni@S-1-100, respectively, indicating the higher water content was favorable to the formation of crystals with higher crystallinity. The SEM images in **Fig. 2.6** supported the observation in XRD. The crystal length increased with the increase in H_2O/SiO_2 ratio. In general, the dilution of the synthetic mixture causes lower supersaturation, which leads to a low nucleation frequency. Consequently, fewer nuclei can be formed, and larger crystals can be obtained.[23,24] In addition, quite a few unconverted amorphous silica was observed over the Ni@S-1-34 sample, suggesting the crystallization was not fully completed.

Table 2.8. The compositions of zeolite mother liquor and properties of the as-prepared Ni@S-1 samples.

Catalyst		Ni@S-1-34	Ni@S-1-50	Ni@S-1-100
Composition of zeolite mother liquor	H_2O/Si	34	50	100
	pH	12.5	12.1	11.7
	[Si] (mol/L)	1.21	0.89	0.49
Ni loading (wt%)[a]		0.93	0.99	0.98
Relative crystallinity (%)[b]		92.4	105.3	117.4
Crystal length (nm)[c]		220	230	330
S_{BET} (m^2/g)[d]		449.3	459.5	428.4
V_{micro} (cm^3/g)[e]		0.129	0.132	0.125
V_{meso} (cm^3/g)[f]		0.351	0.316	0.2934

[a]. Measured by XRF.

[b] Measured by XRD, the relative crystallinity was calculated on the basis of the height of the peak at around 23.1° and assumed that the crystallinity of Silicalite-1 prepared at 100°C for three days was 100%.

[c]. Measured by SEM.

[d]. Calculated by BET equation.

[e]. Calculated by t-plot method.

[f]. Calculated by BJH method.

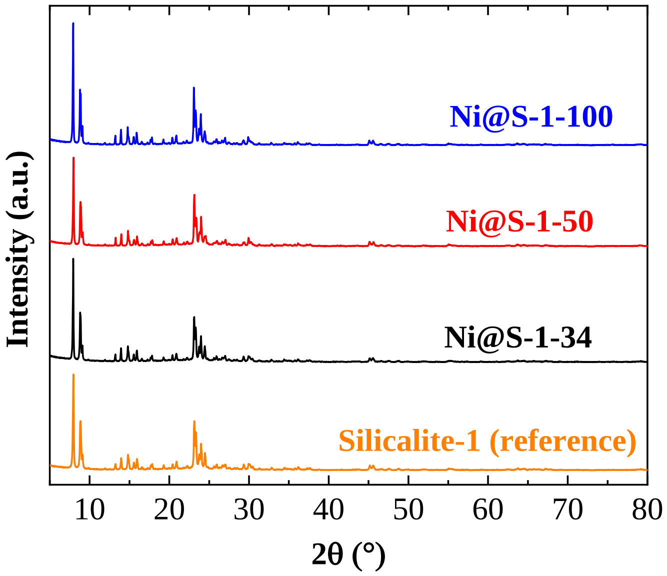

Figure 2.5. (a) XRD patterns of the as-prepared Ni@S-1 samples after calcination at 550 °C for 12 h.

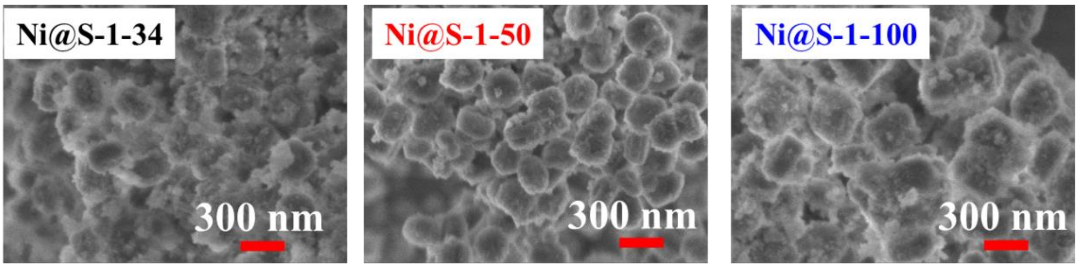

Figure 2.6. SEM images of the as-prepared Ni@S-1 samples after calcination at 550 °C for 12 h.

As shown in **Fig. 2.7**, all the Ni@S-1 samples showed remarkable N_2 uptake at the relative pressure of 0.0, revealing that significant micropores were developed during the transformation. More importantly, the adsorption of N_2 still increased between the relative pressure of 0.3 and 0.8, implying all the synthesized Ni@S-1 catalysts possessed mesopores to some extent. As listed in **Table 2.8**, **t**he mesopore volumes of the resulting catalysts decreased with increasing H_2O/SiO_2 ratio. It has been confirmed in **Fig. 2.4** that the size of Ni-PS was 2 nm × 10nm. In other words, the Ni-PS with such size should be immobilized within the inter-crystalline mesopores between the primary Silicalite-1 crystals. Given the reduction of mesopore volume of the samples in the cases of higher H_2O/SiO_2 ratio, less Ni-PS should be encapsulated in the Silicalite-1 zeolite in the Ni@S-1-100 compared to the other two.

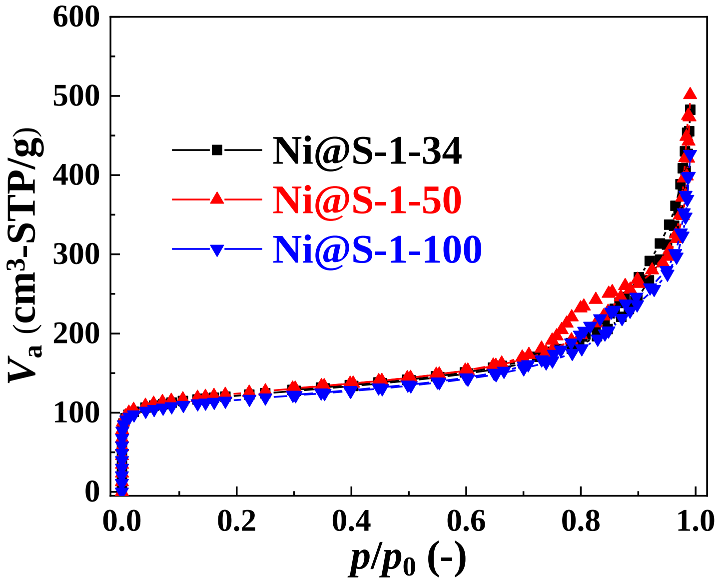

Figure 2.7. N_2-physisorption isotherms of the as-prepared samples after H_2 reduction at 850 °C for 1h.

It is evident that the zeolite morphology of Ni@S-1-34 observed by TEM was worse than that of the other two samples; the amorphous silica was easily found around the zeolite particles. This observation of amorphous silica was consistent with the XRD and SEM results revealing that the Ni@S-1-34 was not fully crystallized. The statistical results of nickel particle size in **Fig. 2.8** show that some Ni particles were located on the amorphous silica in the Ni@S-1-34, and the Ni sintering to generate larger particles was more accessible than that of encapsulating inside zeolite. Accordingly, some Ni particles with a diameter larger than 7 nm were produced in this catalyst after H_2 reduction at 850 °C for 1 h. On the contrary, most Ni particles were highly dispersed and encapsulated within Silicalite-1 zeolite for the Ni@S-1-50 catalyst due to the formation of total crystalline zeolite. Therefore, the Ni@S-1 catalyst with encapsulation structure and ultrafine Ni particles, 2.9 nm in mean size, was obtained. On the other hand, the aggregation of Ni particles was detected over the Ni@S-1-100 sample. Combined with the above characterization results, we inferred that the larger crystal with fewer mesopores could lead to more Ni species not immobilized within the Silicalite-1 zeolite. Therefore, the larger Ni particles were produced after H_2 reduction.

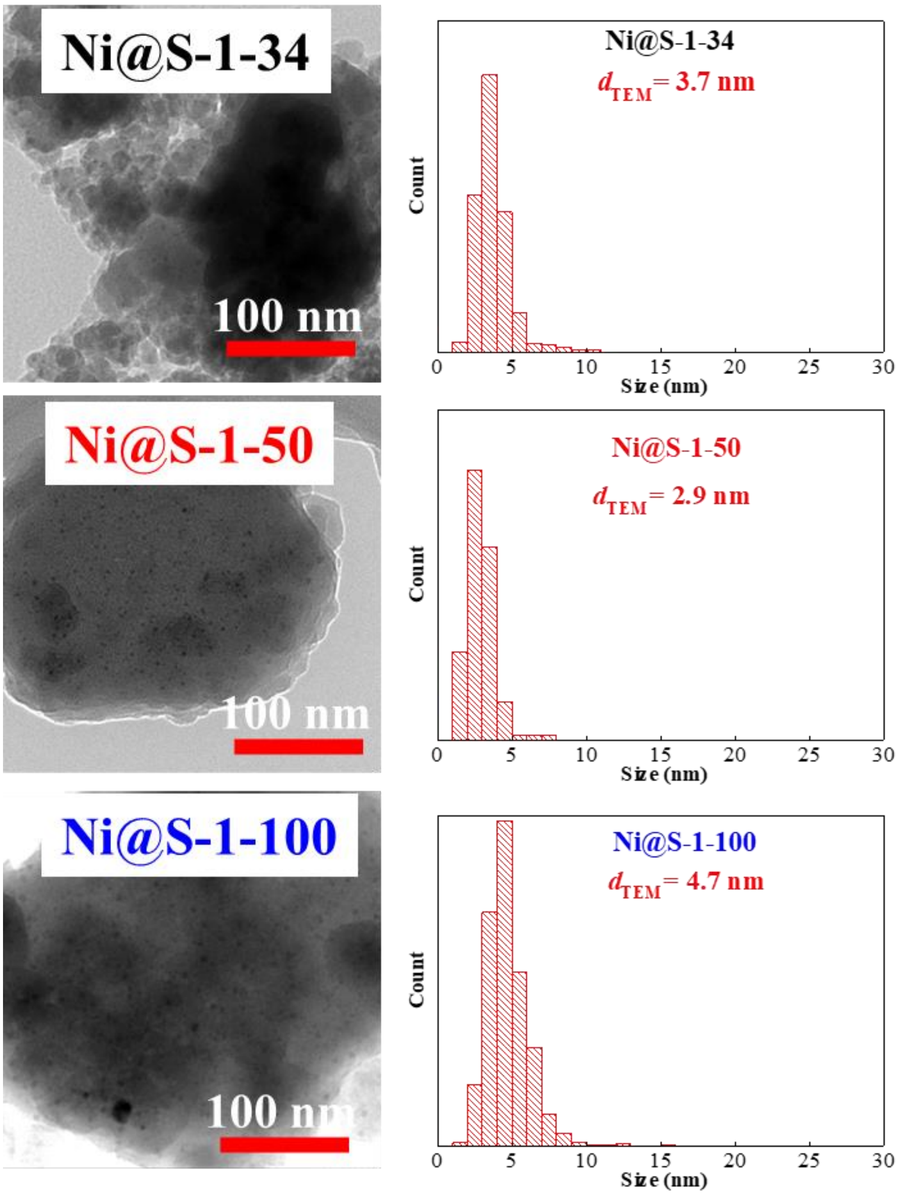

Figure 2.8. TEM images and corresponding Ni particle size distribution of the as-prepared samples after H_2 reduction at 850 °C for 1 h.

2.3.2. Confirmation of catalytic performance and Ni location by the DRM reaction at 600 °C

According to the overview in Chapter 1, if the Ni NPs were fixed inside Silicalite-1 zeolite, the internal space of zeolite would be very limited for the coke deposition. Hence, the coke content of the Ni@S-1 with encapsulation structure should be low after the DRM reaction. On the contrary, a large amount of carbon could form on nickel particles (>7 nm) without spatial constraints on the external surface of the zeolite support during the DRM process. If so, evaluation of the catalyst under a reaction temperature favorable for carbon buildup would confirm the location of nickel particles by its activity and the coke content after the reaction. From a thermodynamic point of view, carbon could accumulate favorably at temperatures less than 700 °C. Accordingly, all the samples were evaluated by DRM reaction at 600 °C.

Fig.2.9 shows the DRM reaction results, in which the dashed lines represent the thermodynamic equilibrium values estimated by the assumption that the DRM and concurrent RWGS reached equilibrium without coke formation. All three catalysts could reach equilibrium activity for DRM reaction, demonstrating the excellent catalytic performances of the Ni@S-1 catalyst using the Ni-PS as the Ni source. Notably, the Ni@S-1-34 and Ni@S-1-100 catalysts could not achieve 100% gaseous carbon recovery, implying that some solid coke was deposited during the DRM reaction. The coke content results measured by TG were listed in the inset of **Fig.2.9d**. As expected, the Ni@S-1-34 and Ni@S-1-100 had some deposited coke, while negligible carbon was accumulated on the Ni@S-1-50 catalyst. Accordingly, for Ni@S-1-34 and Ni@S-1-100 catalysts, some Ni NPs were not fixed inside Silicalite-1. In contrast, most Ni NPs were immobilized within Silicalite-1 in the case of the Ni@S-1-50 catalyst.

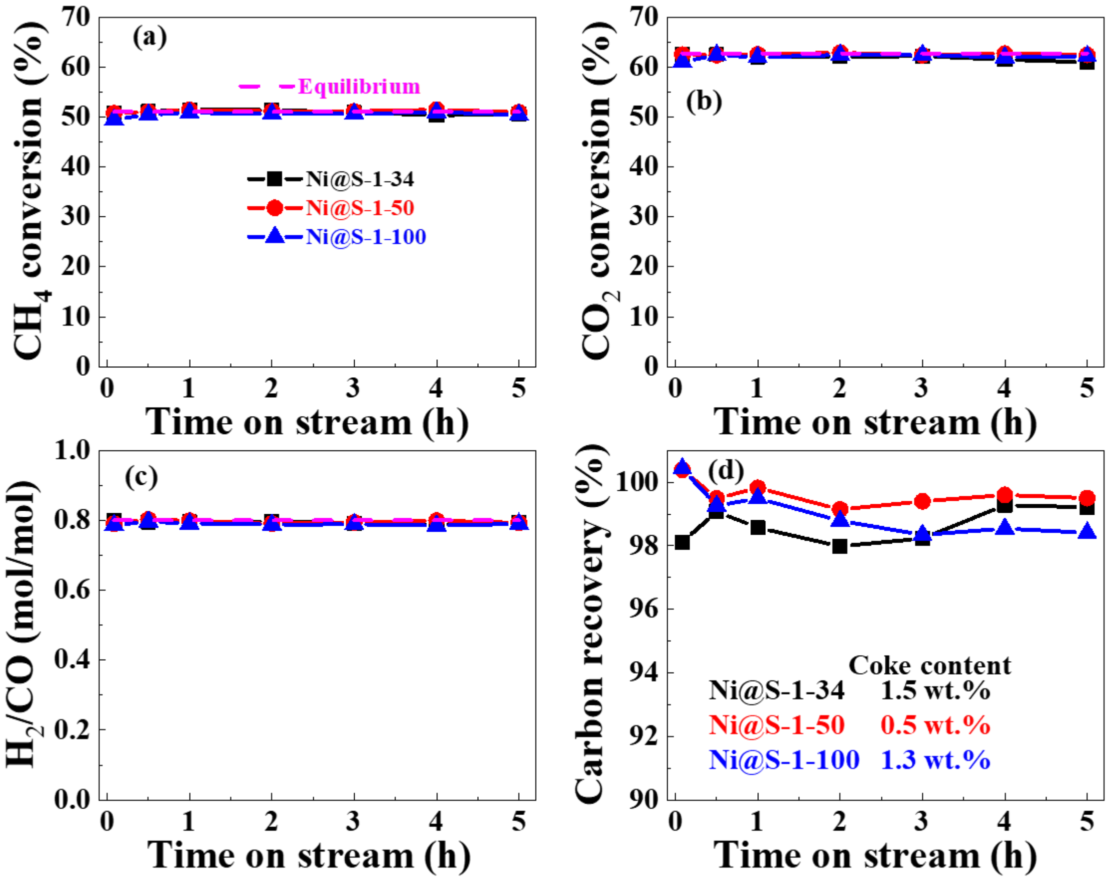

Figure 2.9. Catalytic performances of the as-prepared catalysts for DRM reaction at 600ºC as function of time on stream: (a) CH_4 conversion, (b) CO_2 conversion, (c) H_2/CO ratio, and (d) gaseous carbon recovery (reaction conditions: T= 600 ºC, 1 bar, CH_4/CO_2/Ar/ He= 20/20/40/10mL/min, GHSV= 2,000 L/g-Ni/h)

Then, the TEM characterized the spent catalyst after the DRM reaction. As can be seen in **Fig.2.10,** the filamentous carbon was observed over the spent Ni@S-1-34 and Ni@S-1-100 samples, whereas no discernible carbon could be detected on the spent Ni@S-1-50 catalyst. This phenomenon verifies the encapsulation structure and good suppression of coke formation in the Ni@S-1-50 catalyst. An increase in Ni size was found for Ni@S-1-34 and Ni@S-1-100 samples after the DRM reaction. This Ni sintering affirmed again that some Ni particles were not anchored in the Silicalite-1 in these two catalysts. By contrast, no noticeable increase in the size of Ni particles was monitored for Ni@S-1-50 after the reaction. That is to say, encapsulating ultrafine Ni NPs in thermally stable Silicalite-1 zeolite using the Ni-PS as the Ni source was achievable with a H_2O/SiO_2 ratio of 50.

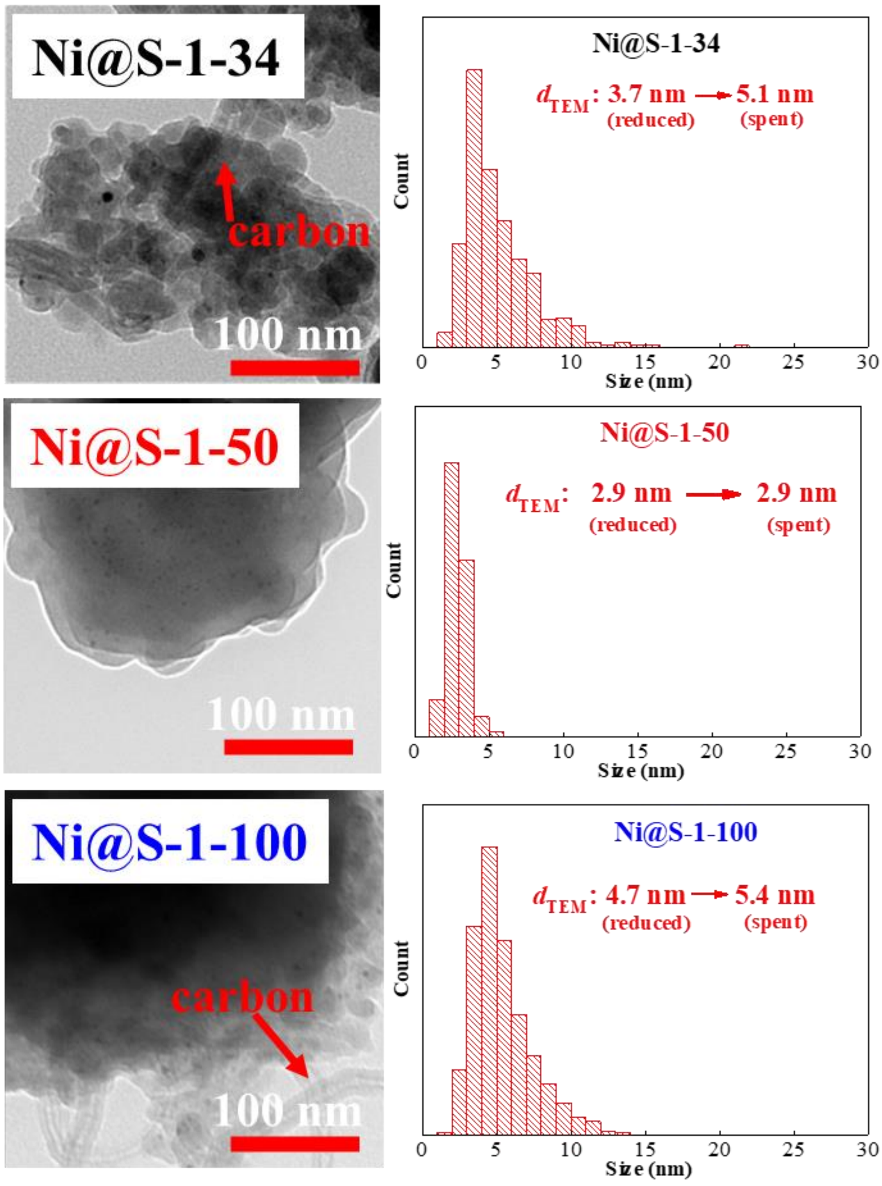

Figure 2.10. TEM images and corresponding Ni particle size distribution of the samples after the DRM reaction at 600 °C for 5 h.

In short, H_2O/SiO_2 ratio directly determines the reactants concentration, which had an important impact on the Ni@S-1 morphology and structure. For the low H_2O/SiO_2 ratio of 34, the higher reactants concentration would lead to higher supersaturation, thus forming more nuclei. Then, after crystallization, smaller crystals with unconverted amorphous silica were observed after crystallization under the employed hydrothermal treatment conditions. As a result, some Ni-PS species were loaded on the amorphous silica. So, the larger Ni NPs would be formed on the amorphous silica after H_2 reduction. That is the reason why this catalyst showed lower DRM activity and higher coke content. Comparatively, too high H_2O/SiO_2 ratio of 100, the low reactants concentration would cause formation of larger crystals with fewer inter-crystalline mesopores for anchoring Ni-PS. Thereof, some Ni species were located on the external surface of zeolite instead. Consequently, the as-prepared Ni@S-1 catalyst had the larger Ni NPs in size after H_2 reduction and exhibited some activity loss and coke accumulation. On the contrary, the zeolite mother liquor with a water-to-silica ratio of 50 was the appropriate condition to prepare Ni@S-1 with most Ni NPs encapsulated within the zeolite. Consequently, it showed good DRM activity as well as high coking suppression.

2.4. Effect of hydrothermal synthesis time and study on the formation mechanism

It is widely accepted that the hydrothermal synthesis time is of significance for the zeolite transformation. The product may be amorphous or not fully crystalline with too short a crystallization time. At the same time, impurities (low-porosity zeolite or non-porous dense phases) may begin to form at too long a crystallization time.[18,25] In addition, the structure of the resulting catalyst dynamically changes with the synthesis time. Consequently, preparation of Ni@S-1 from Ni-PS under H_2O/SiO_2 ratios of 50 and 100 °C for different hydrothermal synthesis time can obtain an insight into the Ni@S-1 structural evolution and thus clarify the formation mechanism.

2.4.1. Catalyst characterization

The as-synthesized 1 wt% Ni@S-1 catalysts were measured by several characterization methods and compared to the precursor, 3 wt% Ni-PS/SiO_2. As shown in **Table 2.9**, all the prepared samples presented actual nickel loadings very close to the theoretical values. The product yield was also almost equal to the nominal yield (not listed here). It represented that almost all the nickel species were taken from the 3 wt% Ni-PS/SiO_2 to 1 wt% Ni@S-1.

XRD patterns of the obtained samples are displayed in **Fig. 2.11a**. There was only one broad and weak peak at 2θ of 15~30° for 3 wt% Ni-PS/SiO_2, which was attributed to the amorphous silica. No Ni-PS characteristic peaks could be seen due to the Ni species' high dispersion and low content. Notably, strong characteristic XRD peaks corresponding to MFI zeolite were observed for all the Ni@S-1 catalysts, suggesting the MFI zeolite was formed after hydrothermal treatment. It can be seen from **Fig. 2.11b** and **Table 2.3** that the relative crystallinity increased from 58.1% for Ni@S-1-100°C-1d to 94.0% for Ni@S-1-100°C-2d and 100.0% for Ni@S-1-100°C-3d. Then the relative crystallinity did not further improve with the HTS time extending to five and seven days, which confirmed that highly crystalline Silicalite-1 zeolite could be prepared at 100 °C for three days.

Table 2.9. Properties of the as-prepared samples after H_2-reduction at 850 °C for 1 h.

Sample	Ni loading[a] (wt%)	RC[b] (%)	Crystal length[c] (nm)	S_{BET}[d] (m^2/g)	V_{micro}[e] (cm^3/g)	V_{meso}[f] (cm^3/g)
Ni-PS/SiO_2	3.01	/	/	9.3	0.002	/
Ni@S-1-100°C-1d	1.00	58.1	180	307.5	0.082	0.377
Ni@S-1-100°C-2d	1.03	94.0	230	429.5	0.127	0.322
Ni@S-1-100°C-3d	0.99	100.0	230	459.5	0.132	0.316
Ni@S-1-100°C-5d	1.01	99.8	270	465.4	0.135	0.310
Ni@S-1-100°C-7d	1.02	100.8	320	473.3	0.140	0.302

[a]. Measured by XRF.

[b] Relative crystallinity was calculated on the basis of the height of the peak at around 23.1° and assumed that the crystallinity of Ni@S-1 prepared at 100°C for three days was 100%.

[c]. Measured by SEM

[d]. Calculated by BET equation.

[e]. Calculated by t-plot method.

[f]. Calculated by BJH method.

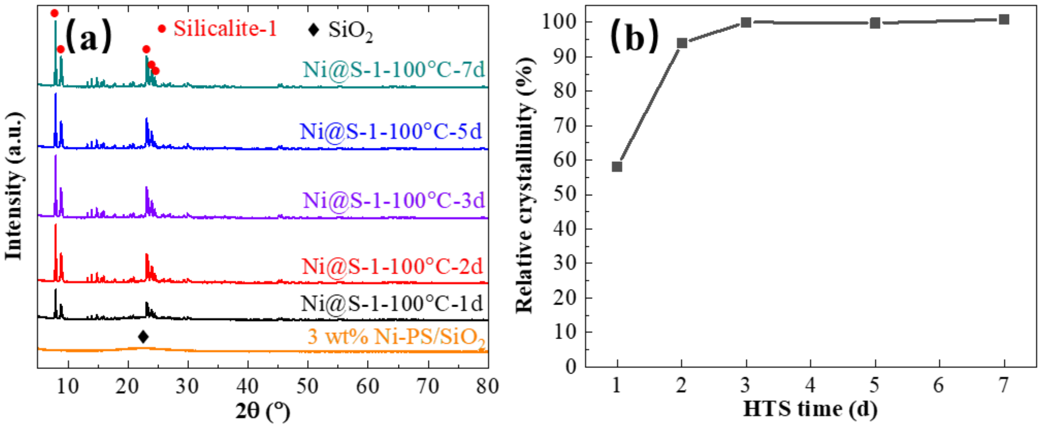

Figure 2.11. (a) XRD patterns and (b) relative crystallinity of the as-prepared samples after calcination at 550 °C for 12 h

SEM measured the morphology of all the samples in **Fig.2.12**. The 3 wt% Ni-PS/SiO$_2$ showed the morphology of the non-porous amorphous matter with viable size. In contrast, the ellipsoid-shaped particles were detected for all the Ni@S-1 samples after crystallization, which were ascribed to the formation of Silicalite-1 zeolite. It is noteworthy that many amorphous lumps with irregular shapes were found in the Ni@S-1-100°C-1d catalyst. These amorphous species decreased with HTS time, while the zeolite particles gradually increased, verifying that zeolite growth comes at the expense of the amorphous matter. Furthermore, the zeolite crystal length increased as the HTS time increased. It is commonly accepted that zeolite crystals are in metastable state in high temperatures and strong alkaline solution, so they could be redissolved in the solution. In addition, according to the Ostwald ripening theory, the small crystals have a higher solubility and lower stability than the larger ones. Therefore, the small crystals formed initially gradually were redissolved into the solution, and act as the nutrient and redeposit onto larger crystals. After the secondary nucleation and recrystallization, the crystals with larger diameter and higher purity would form.[26,27] Overall, the SEM findings were consistent with the XRD results; the total transformation of 3 wt% Ni-PS/SiO_2 into Ni@S-1 needed time to finish. In the case of insufficient crystallization time, one day and two days, the resulting samples still contained unconverted amorphous matter. Then, the fully crystalline zeolite could be obtained when the crystallization time was enough, namely, three days. After that, the redissolution-recrystallization proceeded resulting in formation of bigger crystals in the cases of excessive crystallization time.

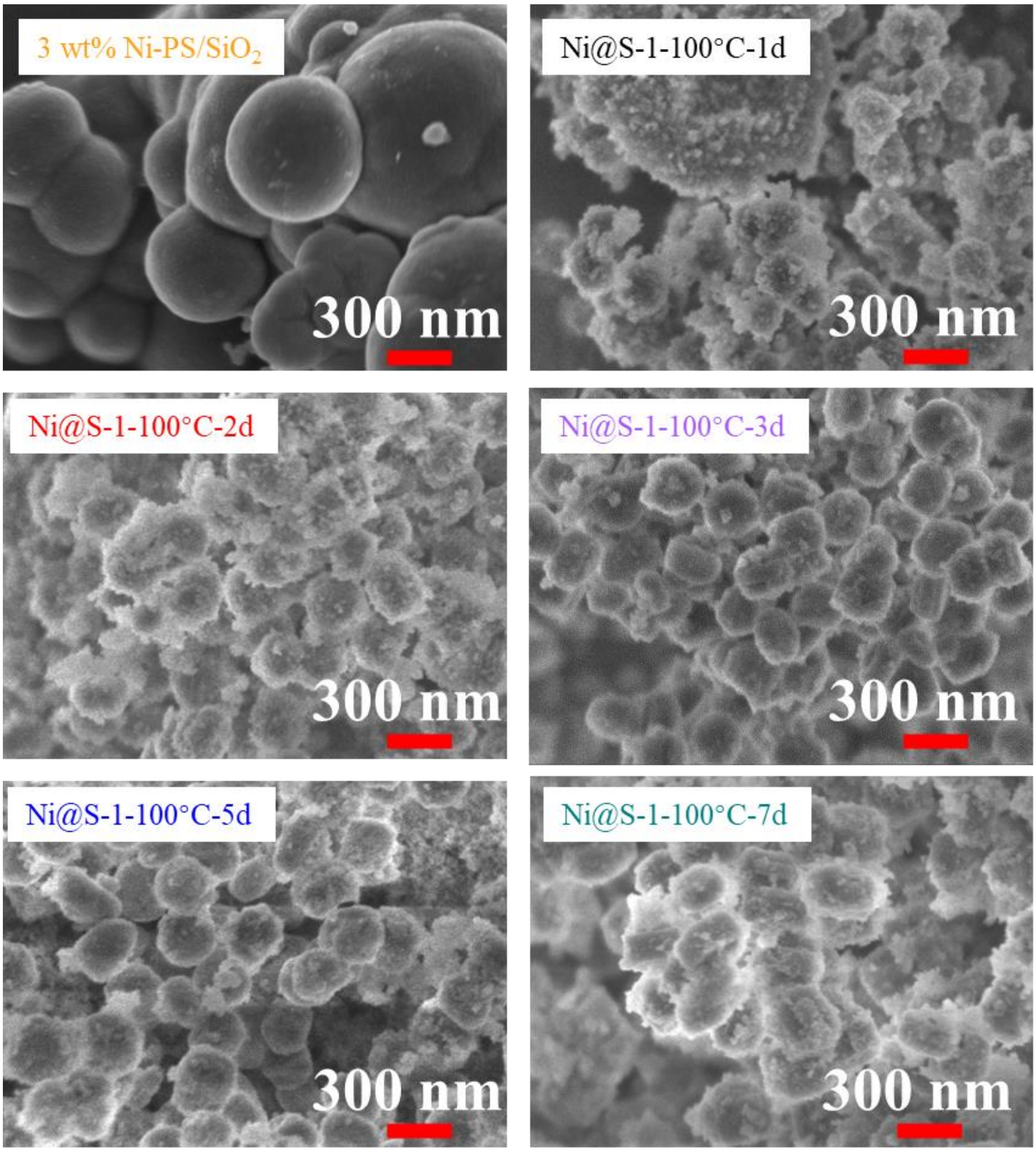

Figure 2.12. SEM images of the as-prepared 3 wt% Ni-PS and 1 wt% Ni@S-1 samples

after calcination at 550 °C for 12 h

The nitrogen-physisorption isotherms of the samples after H_2-reduction are presented in **Fig. 2.13**, and the relevant BET surface area and micropore volume results are summarized in **Table 2.9**. The 3 wt% Ni-PS/SiO_2 exhibited almost flat isotherms and no adsorbed nitrogen during the measurement. Its S_{BET} was 9.3 m^2/g, and V_{micro} was only 0.002 cm^3/g, saying that the 3 wt% Ni-PS/SiO_2 was the non-porous material. Compared to 3 wt% Ni-PS/SiO_2, all the Ni@S-1 showed remarkable nitrogen uptake at a relative pressure of 0.0, representing that significant micropores were formed after the second HTS treatment. In addition, the nitrogen adsorption volume at the micropore filling stage of Ni@S-1 grew as the HTS time increased from one day to three days. As can be seen, the BET surface area and micropore volume increased from 307.5 m^2/g and 0.082 cm^3/g for Ni@S-1-100°C-1d to 429.5 m^2/g and 0.127 cm^3/g for Ni@S-1-100°C-2d, and further rose to 459.5 m^2/g and 0.132 cm^3/g for Ni@S-1-100°C-3d. These results elucidated that the amorphous species was increasingly converted into porous Silicalite-1 zeolite with the proceeding of hydrothermal treatment. Additionally, the nitrogen uptake and the calculated BET surface area and micropore volume of did not significantly increase when the hydrothermal treatment time increased from three days to seven days. Once again, verifying that the fully crystalline zeolite could be synthesized after hydrothermal treatment at 100 °C for three days. Notably, as listed in **Table 2.9**, the mesopore volume decreased with the increase of HTS time. This reduction in mesopore volume might be because the redissolution-recrystallization of small crystals resulted in the formation of larger crystals with fewer mesopores and higher purity. This may also lead to the migration of the impurity, Ni-PS, immobilized in the mesopores within the zeolite crystal to the outer surface of the zeolite.

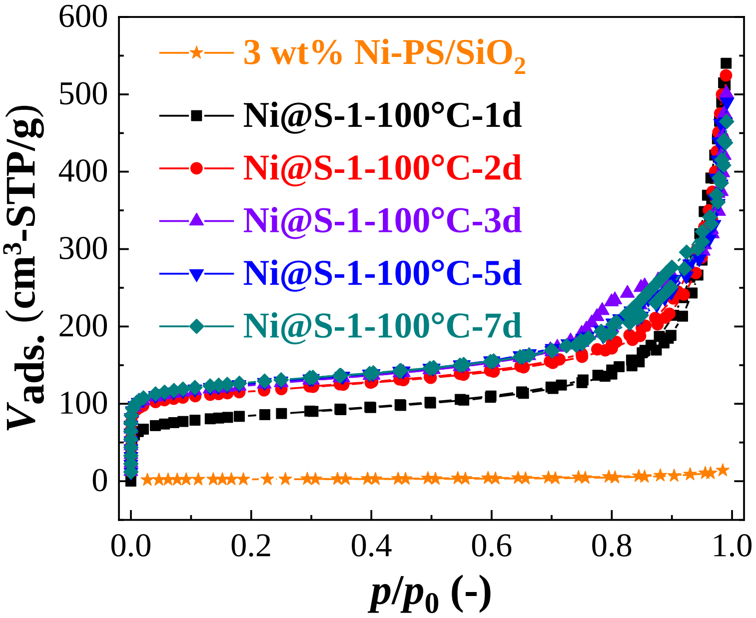

Figure 2.13. N_2-physisorption isotherms of the as-prepared samples after H_2 reduction at 850 °C for 1h.

The reducibility of the resulting samples was measured by H_2-TPR and depicted in **Fig.2.14**. As explained in the last section, the 3 wt% Ni-PS/SiO_2 showed one reduction peak at 450-800 °C corresponded to reduction of 1:1 Ni-PS to Ni^0. After crystallization, the reduction temperature of all the Ni@S-1 samples shifted to the higher temperature region, 600-900 °C. It was owing to the formation of more thermally stable 2:1 Ni-PS in Ni@S-1.[16,28] In comparison with 3 wt% Ni-PS/SiO_2, the Ni@S-1 catalysts possessed stronger metal-support interaction.

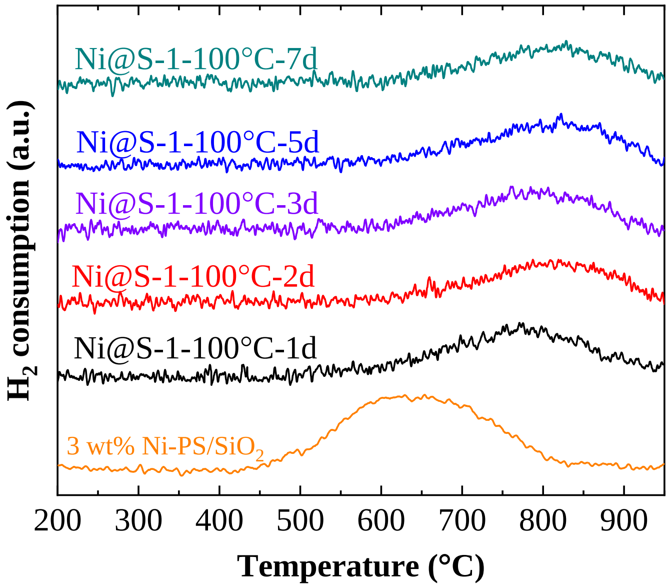

Figure 2.14. H_2-TPR profiles of the as-prepared samples

Then, the TEM characterization was performed to observe the size and distribution of Ni particles after H_2 reduction at 850 °C for 1 h. As shown in **Fig.2.15**, Ni NPs in the 3 wt% Ni-PS/SiO_2 were randomly distributed over the silica support and had an average diameter of 5.6 nm and broad size distribution of 1 to 30 nm. Evidently, various aggregated Ni NPs with sizes larger than 10 nm were observed over 3 wt% Ni-PS/SiO_2 after H_2 reduction, revealing the poor thermal stability of amorphous silica, and thus showing poor resistance to Ni sintering. In contrast, after transformation, the mean size of Ni NPs for Ni@S-1-100°C-1d decreased to 4.0 nm with a size distribution of 1 to 14 nm. Increasing HTS time from one day to three days, the average diameter of Ni NPs further decreased, and the size distribution tended to concentrate in the smaller region. Remarkably, for the Ni@S-1-100°C-3d catalyst, the average Ni NPs in size were 2.9 nm and highly dispersed in the Silicalite-1 host, and no Ni NPs greater than 7 nm were detected. Such discrepancy gives clear evidence that growing number of Ni NPs were confined into the matrix of Silicate-1 zeolite with the increase of crystallinity and were protected from sintering into larger particles. Interestingly, the agglomerated Ni NPs larger than 10 nm were generated at the edge of the Silicalite-1 support in Ni@S-1 catalysts with excessive crystallization time. To be more specific, the average sizes of Ni NPs were 4.6 nm for Ni@S-1-100°C-5d and 4.9 nm for Ni@S-1-100°C-7d. As discussed earlier, the metastable state of the crystals and Ostwald ripening process would lead to the redissolution-recrystallization of the small zeolite crystals to form the larger crystals with fewer inter-crystalline mesopores and higher purity. Consequently, the Ni-PS initially embedded in the mesopores of small crystals would be released into the solution due to the destruction of zeolite shell. Then, the free Ni-PS would be redeposited onto the surface of the larger crystals. Therefore, the Ni-PS located on the external surface of Silicalite-1 would sinter and aggregate into large Ni particles after H_2-reduction at 850 °C for 1 h.[29–32] Thus, Ni NPs size increased over Ni@S-1-100°C-5d and Ni@S-1-100°C-7d after H_2 reduction.

Based on the characterization results, preparation of Siliclaite-1-encapsulated ultrafine Ni nanoparticles catalyst using 3 wt% Ni-PS/SiO_2 as the Ni source was achievable. Most Ni NPs could be immobilized inside the support after hydrothermal treatment at 100 °C for three days, and thereof the obtained Ni@S-1 catalyst exhibited a strong metal-support interaction and good resistance to Ni sintering into larger particles.

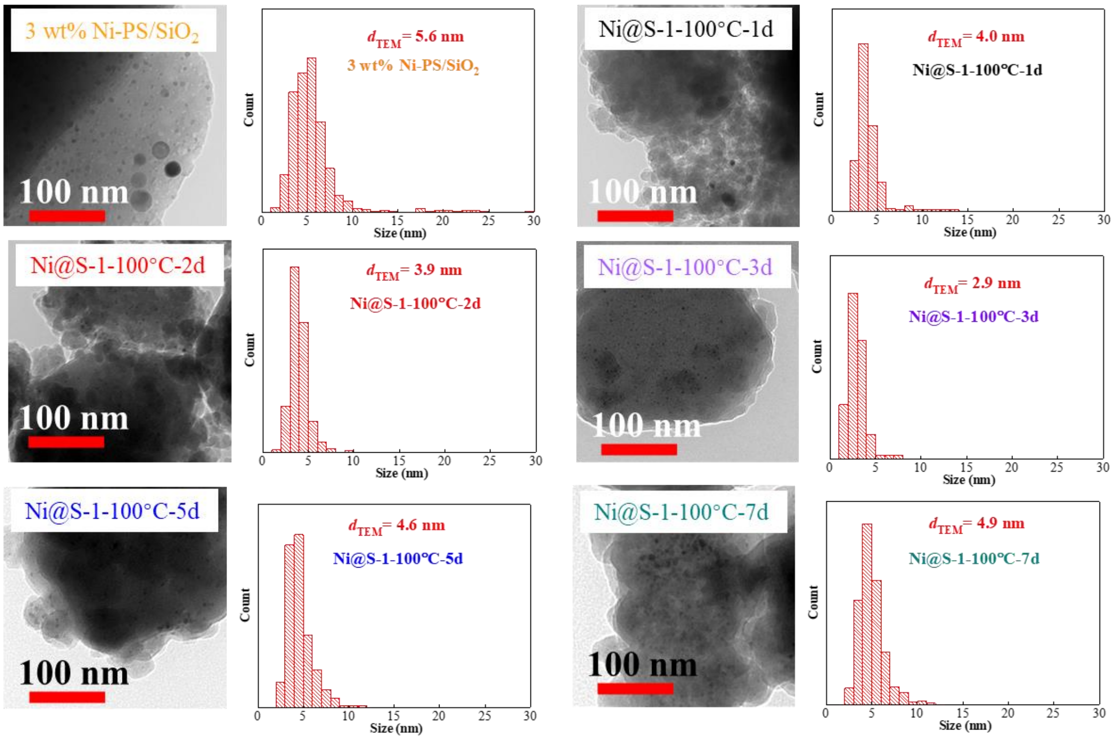

Figure 2.15. TEM images and corresponding Ni particle size distribution of the as-prepared samples after H_2 reduction at 850 °C for 1 h.

2.4.2. Confirmation of Ni location by DRM at 600 °C

To confirm the Ni location, all the samples were evaluated by the DRM reaction at 600 °C for 5h. As decribed in **Fig.2.16**, the 3 wt% Ni-PS/SiO_2 exhibited the lowest DRM activity. Its poorer catalytic performance is because larger nickel particles generated result in fewer active sites. On the contrary, all the Ni@S-1 catalysts showed the better DRM activity than that of the 3 wt% Ni-PS/SiO_2. Not surprisingly, as mentioned above, more Ni NPs were encapsulated inside the Silicalite-1 zeolite with the increase of zeolite crystallinity, and the resulting catalysts could control Ni NPs in smaller size, so CH_4 and CO_2 conversion over Ni@S-1 catalysts improved with the HTS time from one day to three days. Remarkably, the Ni@S-1-100°C-3d could reach the equilibrium activity. Considering the redissolution-recrystallization occurred and caused the relocation and aggregation of Ni NPs on the exterior of Silicalite-1 when the HTS time is excessive. Consequently, the following order of catalytic activity was found Ni@S-1-100°C-3d > Ni@S-1-100°C-5d > Ni@S-1-100°C-7d. In addition, as shown in **Fig. 2.16d**, except the Ni@S-1-100°C-3d, all the rest of the samples employed were not able to achieve 100% recovery of carbon in the gas products, implying that solid carbon deposited on the catalysts.

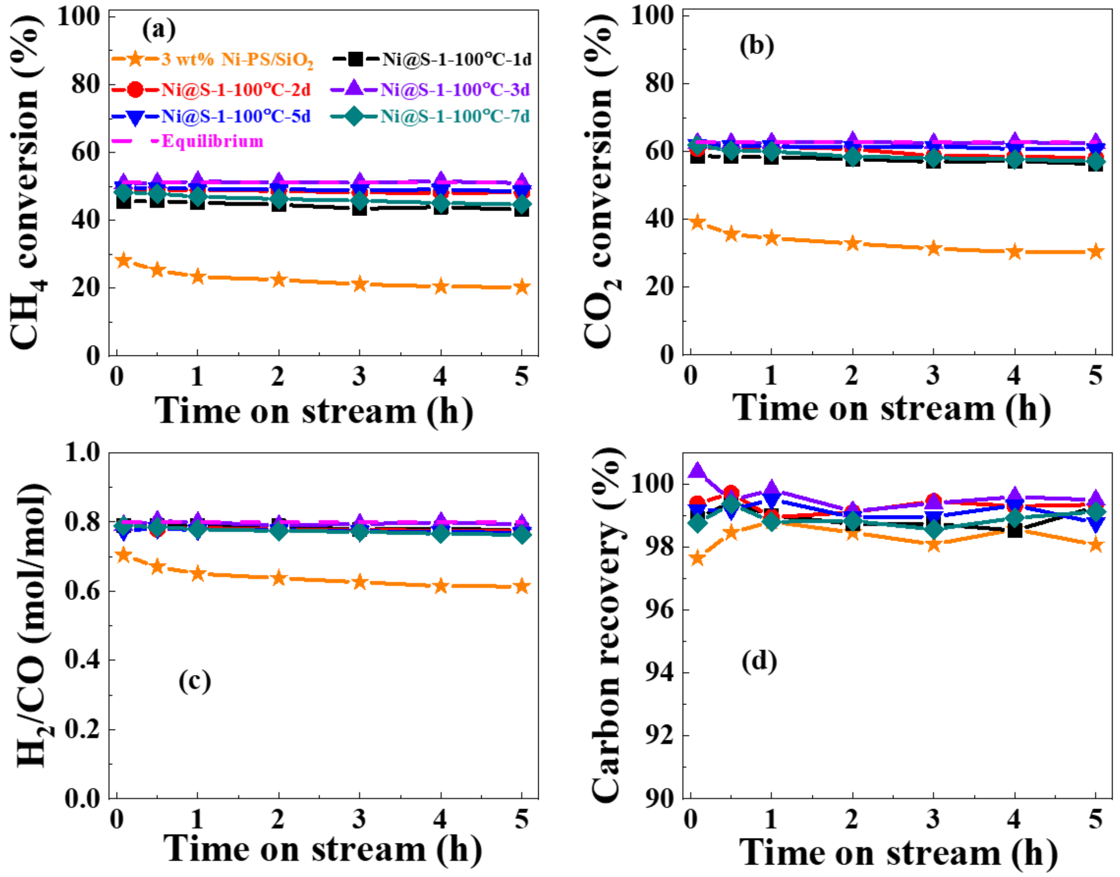

Figure 2.16. Catalytic performances of the as-prepared catalysts for DRM reaction at 600°C as function of time on stream: (a) CH_4 conversion, (b) CO_2 conversion, (c) H_2/CO ratio, and (d) gaseous carbon recovery (reaction conditions: T= 600 °C, 1 bar, CH_4/CO_2/Ar/ He= 20/20/40/10mL/min, GHSV= 2,000 L/g-Ni/h)

Then, the TG test was carried out to measure the amount of accumulated coke after the DRM reaction. As listed in **Table. 2.10**, 3 wt% Ni-PS/SiO_2 had coke content of 2.9 wt%. Then, coke content over Ni@S-1 catalysts decreased as the crystallinity and encapsulation degree improved. Notably, the accumulated carbon was only 0.5 wt.% for Ni@S-1-100°C-3d, verifying its excellent suppression of coke formation due to the encapsulation structure. The anti-coking behavior became deteriorated over the Ni@S-1 prepared by excessive HTS time. To be specific , the coke contents were 1.5 wt% and

1.7 wt% for Ni@S-1-100°C-5d and Ni@S-1-100°C-7d, respectively. The SEM images in **Fig. 2.17** of the spent catalysts agrees with the TG results. Among all the catalysts employed, only Ni@S-1-100°C-3d no filamentous carbon was observed, indicating that most Ni NPs in this catalyst should be encapsulated inside the Silicalite-1 zeolite, and therefore it exhibited a good suppression of carbon accumulation.

Table 2.10. Properties of the evaluated catalysts after the DRM reaction.

Sample	Coke content[a] (wt%)	S_{BET}[b] (m^2/g)	V_{micro}[c] (cm^3/g)
3 wt% Ni-PS/SiO_2	2.9[d]	4.7	0.001
Ni@S-1-100°C-1d	2.0	295.4	0.075
Ni@S-1-100°C-2d	1.5	408.5	0.115
Ni@S-1-100°C-3d	0.5	454.8	0.133
Ni@S-1-100°C-5d	1.5	460.9	0.132
Ni@S-1-100°C-7d	1.7	471.7	0.137

[a]. Measured by TG

[b]. Calculated by BET equation.

[c]. Calculated by t-plot method.

[d]. The coke content was estimated on the net weight of Ni-PS/SiO_2 without including the weight of quartz sand for dilution.

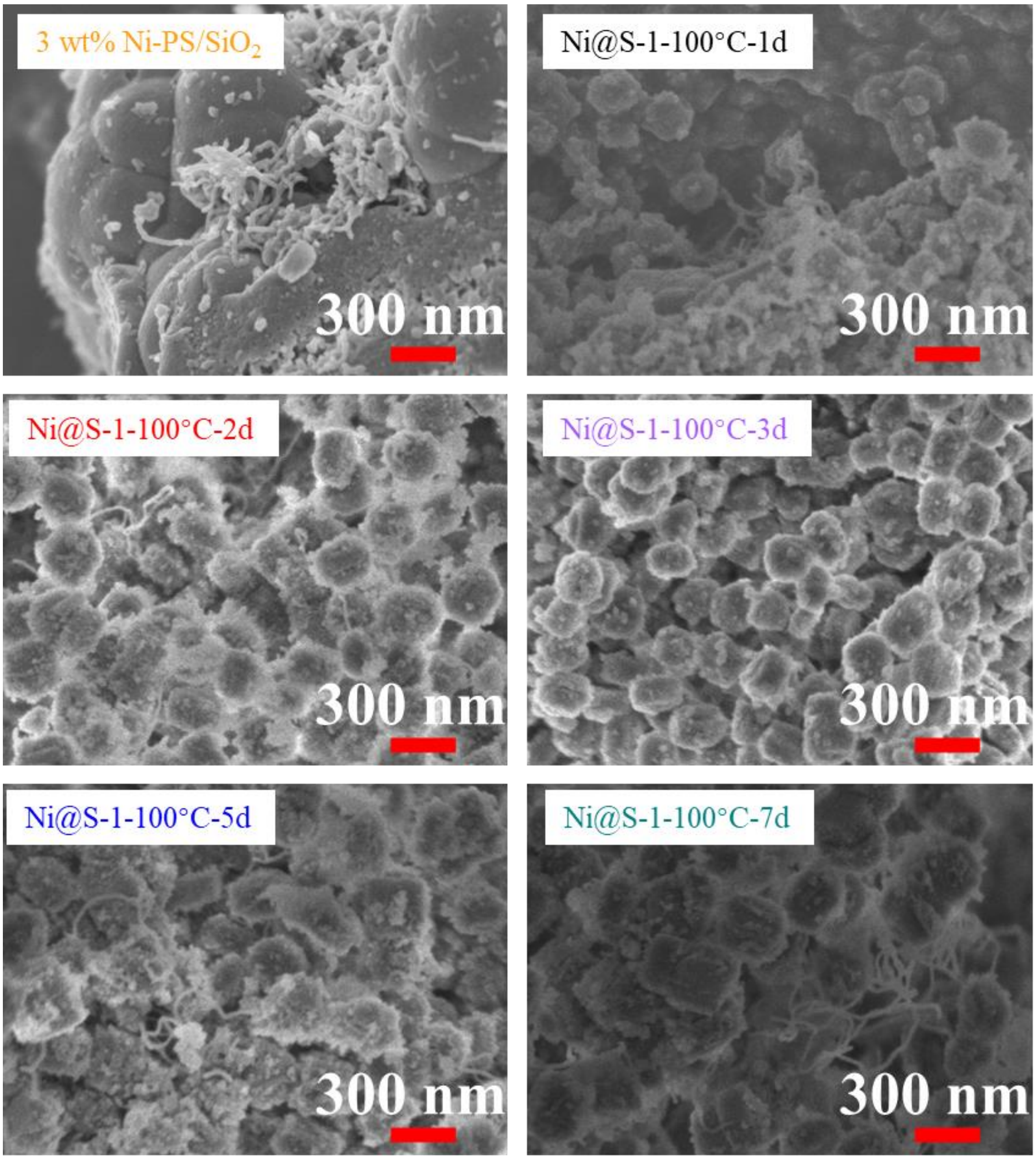

Figure 2.17. SEM images of spent catalysts after the DRM reaction.

Fig. 2.18 shows the TEM images of the catalysts after the DRM reaction. In agreement with the TG and SEM results, carbon nanotubes were discovered in all spent catalysts with carbon content greater than 1.0 wt%, whilst the morphology of Ni@S-1-100°C-3d was same as that before the reaction. More importantly, for spent 3 wt% Ni-PS/SiO$_2$, Ni@S-1-100°C-1d, and Ni@S-1-100°C-2d, the average size of the nickel particles became larger after the reaction, and the proportion of particles larger than 7 nm increased. This variation may be attributed to the presence of amorphous silica in these samples and the collapse of the amorphous species when subjected to high-temperature treatment. The Ni@S-1-100°C-3d maintained its ultrafine Ni NPs, proving that most Ni NPs were enveloped in the matrix of zeolite. Noticeably, big Ni particles larger than 20 nm were detected over Ni@S-1-100°C-5d and Ni@S-1-100°C-7d after the reaction. It suggested that some nickel particles were loaded on the external surface of the support, and their sintering caused the particles to become larger, which leads to carbon generation.

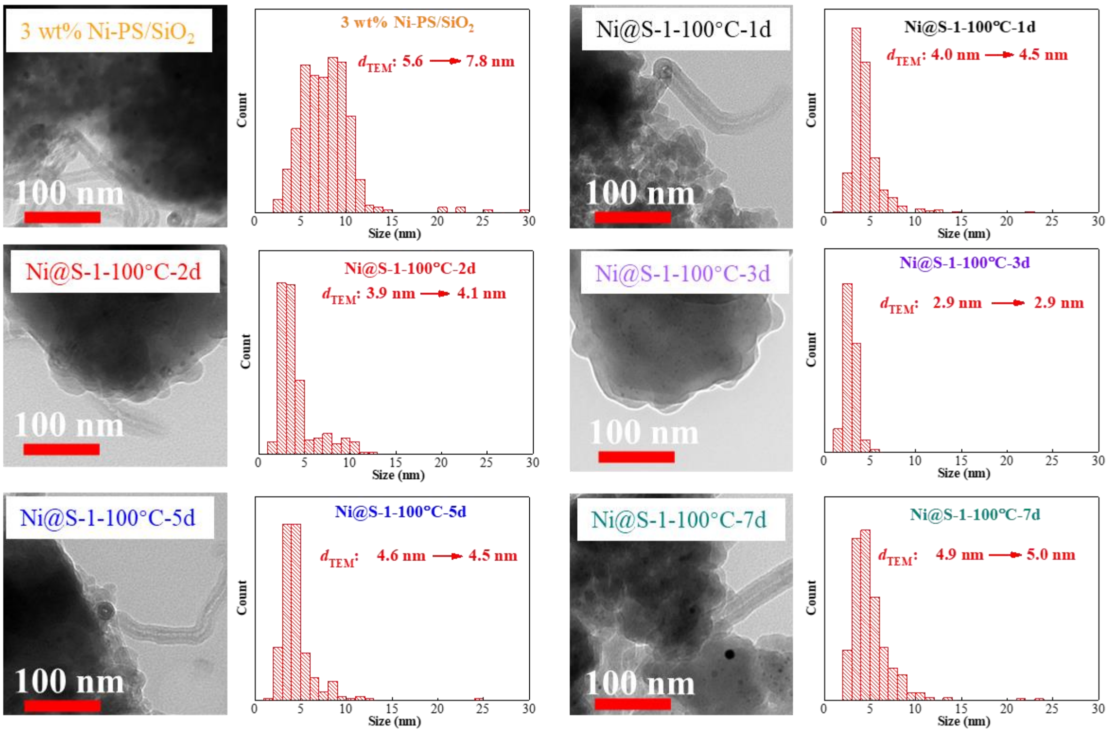

Figure 2.18. TEM images and corresponding Ni particle size distribution of spent catalysts after the DRM reaction.

The N_2-physisorption measurement was performed to confirm whether the collapse of support took place during the DRM reaction. **Fig. 2.19** and **Table 2.10** show that the BET surface area and micropore volume of 3 wt% Ni-PS/SiO_2, Ni@S-1-100°C-

1d, and Ni@S-1-100°C-2d declined after reaction, verifying that structure collapse of amorphous silica coexisted in these samples occurred and thus giving rise to the Ni sintering during DRM reaction. In contrast, the Ni@S-1-3d, Ni@S-1-5d, and Ni@S-1-7d catalysts without amorphous matter exhibited no significant change in the BET surface area and micropore volume after DRM reaction, unveiling the good thermal stability of Silicalite-1 zeolite.

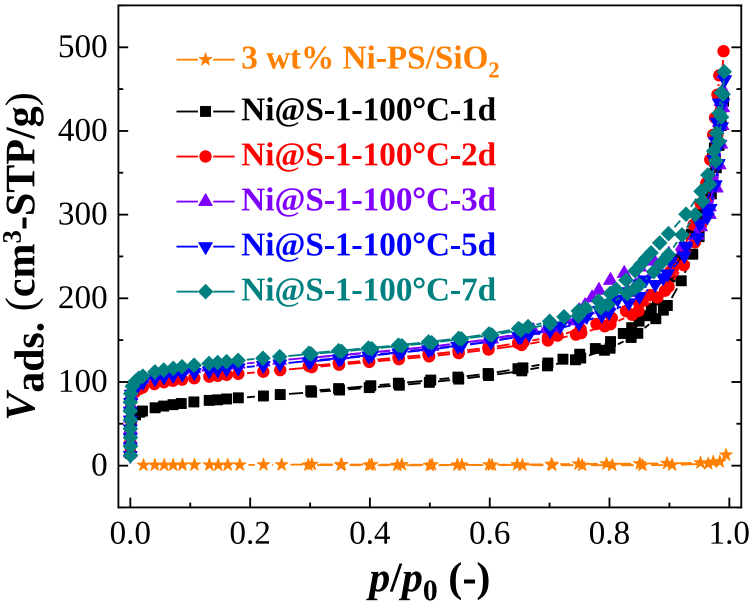

Figure 2.19. N_2-physisorption isotherms of the spent samples after the DRM reaction

According to the characterization and DRM results, the formation mechanism can be assumed and illustrated in **Fig. 2.20**. Generally, the transformation process can be described as follows: the reactants were firstly hydrolyzed and condensed. Considering that the unique layered structure of Ni-PS, characterized by the presence of nickel and silicon atoms interconnected by strong -Ni-O-Si- chemical bonds, grants Ni-PS exceptional structure stability during the transformation. After the hydrolysis and condensation, the autoclave reactor was heating to a high temperature (⩾100°C). Following that, the process of zeolite crystal nucleation ensued. It has been documented that nucleation can either occur homogeneously, in the absence of foreign particles in the solution, or heterogeneously, with the influence of foreign particles. These two mechanisms of nucleation are collectively referred to as primary nucleation. Typically, heterogeneous nucleation occurs more rapidly as foreign particles serve as a platform for the growth of crystals, thus eliminating the need to establish a new surface and reducing the surface energy requirements.[33] This implies that the formation of zeolite nuclei is favored on the Ni-PS surface. After that, zeolite crystals grew, leading to the formation of Ni species within inter-crystalline mesopores between primary zeolite crystals.

However, if the hydrothermal time was insufficient, some Ni-PS remained on the unconverted amorphous silica and sintered to form large Ni NPs during H_2-reduction, resulting in lower DRM activity and higher coke content. Comparatively, most Ni-PS were immobilized in the zeolite matrix if the crystallization time was appropriate, forming ultrafine Ni NPs after H_2-reduction and maintaining their size during the DRM reaction. Accordingly, this catalyst showed high DRM activity and good suppression of coke formation. However, in the case of excessive time, the metastable state of zeolite crystals in high temperatures and strong alkaline solution would lead to the redissolution of the as-formed crystals. Furthermore，as per the Ostwald ripening law, larger crystals exhibit greater thermodynamic and energetic stability compared to smaller crystals. This means that the spontaneous process of dissolution of small crystals, followed by the redeposition of the dissolved species onto the surfaces of larger crystals, leading to the formation of even larger ones, is driven by thermodynamic forces.[27,34,35] Accordingly, the redissolution-recrystallization of zeolite proceeded. During this process, small crystals were redissolved, freeing the Ni-PS previously immobilized within small crystals back into the solution. Then, secondary nucleation occurred, facilitated by the presence of zeolite crystals. This process took place on the surface of the existing crystals, leading to a lower energy barrier for crystal formation compared to primary nucleation.[33,35] As a result, a greater number of nuclei were generated on the surface of the remaining crystals. After recrystallization, some Ni-PS were redeposited onto the external surface of larger crystals with fewer inter-crystalline mesopores and higher purity. Consequently, these Ni-PS without encapsulation would be aggregated on the external surface of zeolite after H_2-reduction to produce the larger Ni NPs, leading to lower DRM activity and higher coke accumulation in comparison to the catalyst with most Ni NPs immobilized in the zeolite,

(a) Insufficient crystallization time

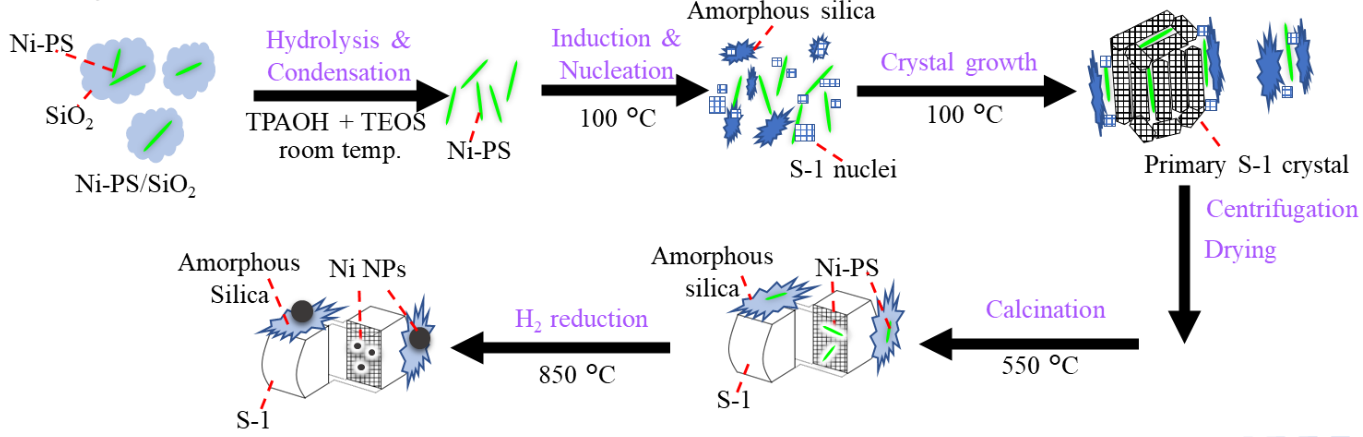

(b) Suitable crystallization time

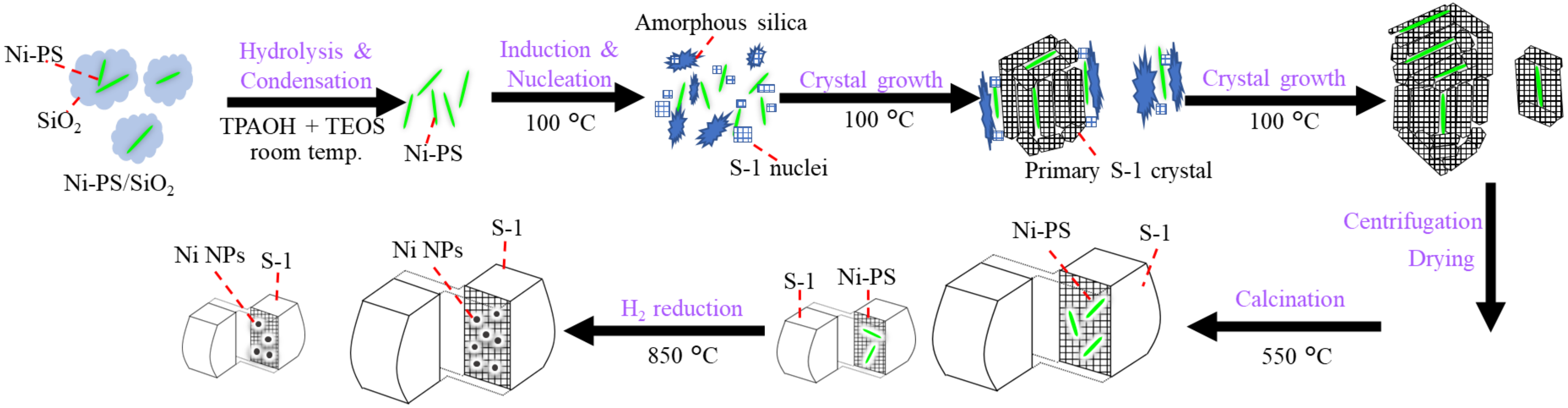

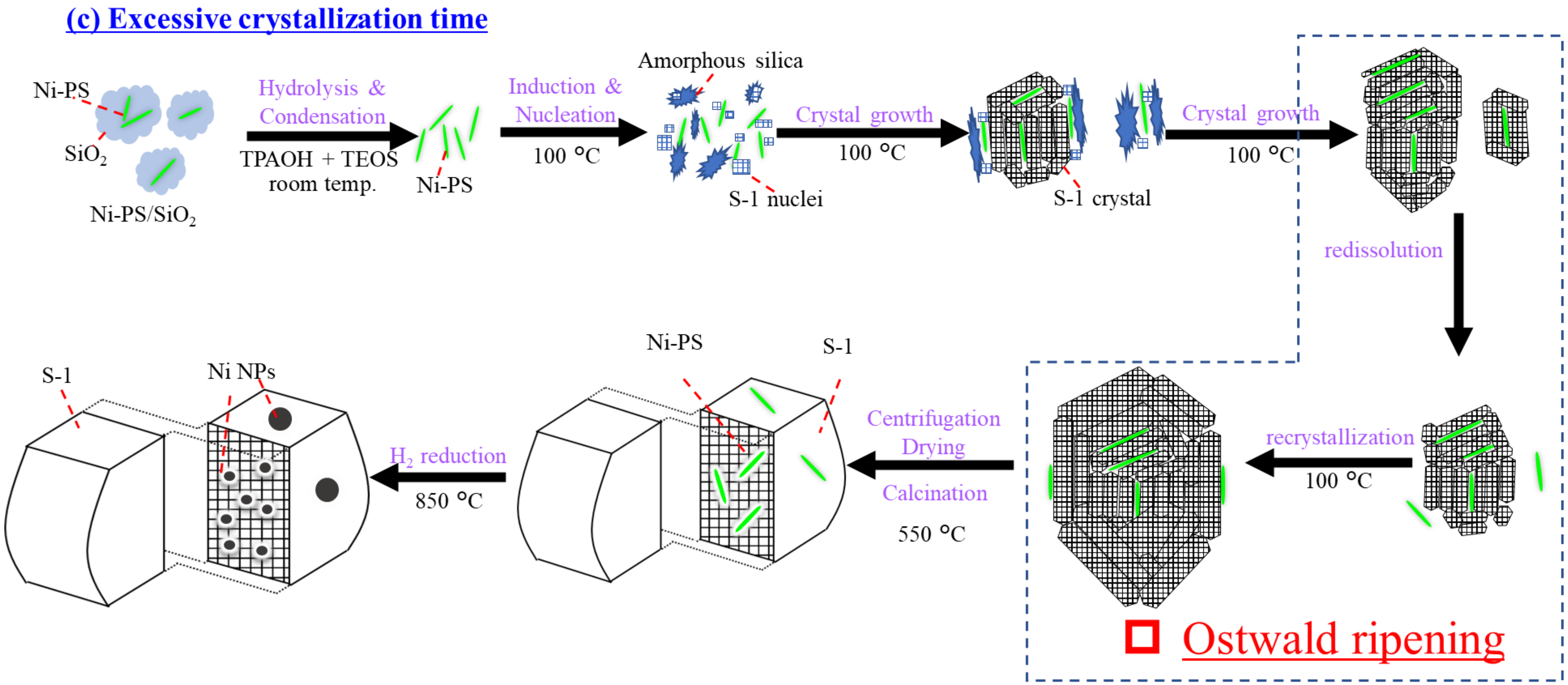

Figure 2.20. The schematic illustration of formation mechanism of Ni@S-1 from Ni-PS/SiO$_2$.

2.5. Effect of HTS temperature

In the last section, the formation mechanism was speculated based on the experimental results, considering that the differences between each catalyst were not particularly large. Therefore, the proposed mechanism was further checked in this section. It is well-known that the higher HTS temperature could cause higher system pressure in parallel with lower water density and viscosity, thus accelerating the crystallization speed.[24,36] Accordingly, the faster redissolution-recrystallization of zeolite could be achieved under high HTS temperature, leading to form larger crystals with fewer Ni NPs immobilized within zeolite. As a result, the Ni@S-1 catalyst prepared at higher HTS temperature should show lower DRM activity and higher coke content. Accordingly, three Ni@S-1 catalysts were prepared at different HTS temperatures, e.g., 100 °C, 150 °C, and 180 °C for three days to double-check the formation mechanism proposed above.

2.5.1. Catalyst characterization

Table 2.11 lists the measured Ni loading in the obtained samples. Ni@S-1 catalysts prepared at 150 °C and 180 °C showed lower Ni loading than the nominal value. It is a general knowledge that the solubility increased with temperature. So, more Ni species may be dissolved in the solution during the synthesis under the higher temperature conditions.

XRD patterns of the resulting catalysts and their relative crystallinity are presented in **Fig. 2.21** and **Table 2.11**. As can be seen, the relative crystallinities were 100.0%, 132.6%, and 166.9% for Ni@S-1-100°C-3d, Ni@S-1-150°C-3d, and Ni@S-

1-180°C-3d, respectively. That is, the crystallinity increased as the HTS temperature increased. SEM images in **Fig. 2.22** exhibited that the Silicalite-1 zeolite with a bigger size (**Table 2.11**) could be synthesized when the higher HTS temperature was used. This observation coincided well with the XRD measurement, namely, the increase in HTS temperature accelerates redissolution-recrystallization of zeolite crystal to form larger crystals. The estimated mesopore volumes from the N_2-physisorption measurement (**Fig. 2.23**) were listed in **Table 2.11**. As anticipated, the Ni@S-1 catalysts synthesized at higher temperatures possessed lower mesopore volume.

Table 2.11. Properties of the as-prepared samples after calcination at 550 °C for 12 h.

Catalyst	Ni loading[a] (wt%)	RC[b] (%)	Crystal length[c] (nm)	V_{meso}[d] (cm^3/g)
Ni@S-1-100°C-3d	0.99	100.0	230	0.316
Ni@S-1-150°C-3d	0.90	132.6	330	0.241
Ni@S-1-180°C-3d	0.94	166.9	770	0.082

[a]. Measured by XRF

[b]. Relative crystallinity was calculated on the basis of the height of the peak at around 23.1° and assumed that the crystallinity of Ni@S-1-100°C-3d was 100%.

[c]. Measured by SEM

[d]. Calculated by BJH method.

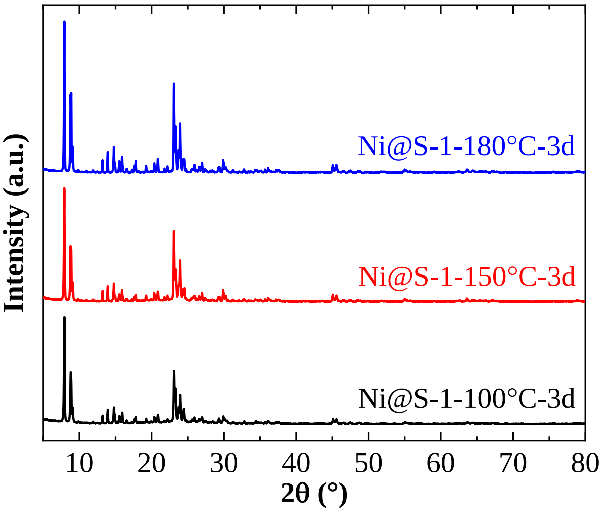

Figure 2.21. XRD patterns of the as-prepared samples.

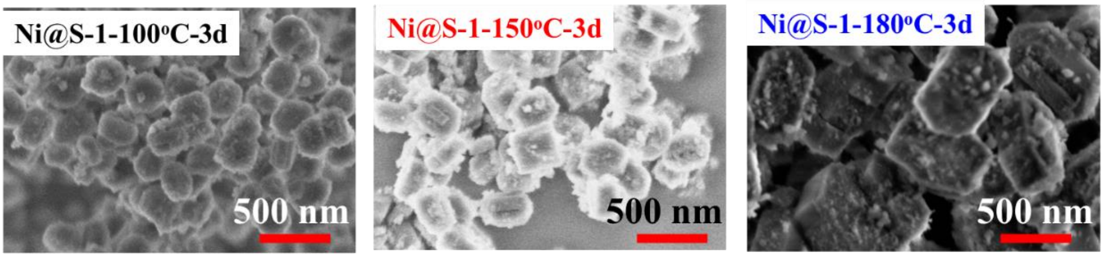

Figure 2.22. SEM images of the as-prepared samples after calcination.

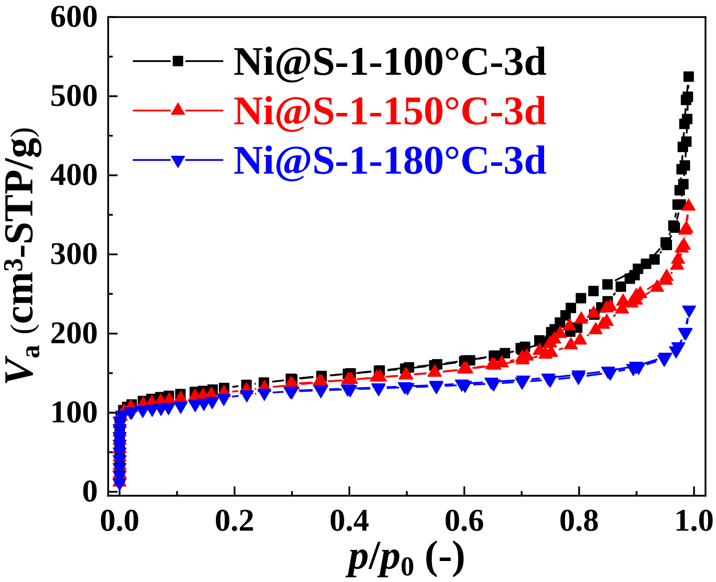

Figure 2.23. N_2-physisorption isotherms of the as-prepared samples after calcination at 550 °C for 12 h.

The TEM characterization was carried out to verify the Ni NPs' size and location. As shown in **Fig. 2.24**, compared to Ni@S-1-100°C-3d, some Ni NPs in Ni@S-1-150°C-3d were observed at the edge of the Silicalite-1 zeolite. The mean Ni NPs size became larger to 4.5 nm with a broader size distribution of 1 to 13 nm. More Ni NPs with a rather big size (> 10 nm) were detected in Ni@S-1-180°C-3d. In more detail, the Ni NPs were 6.5 nm in average size and had a relatively wide distribution from 1 nm to 28 nm. These bigger Ni particles are attributed to the faster crystallization and redissolution-recrystallization speeds at higher HTS temperature, leading to formation of larger crystals with fewer inter-crystalline mesopores and higher purity and causing more Ni-PS migrated and located on the external surface of Silicalite-1 zeolite.

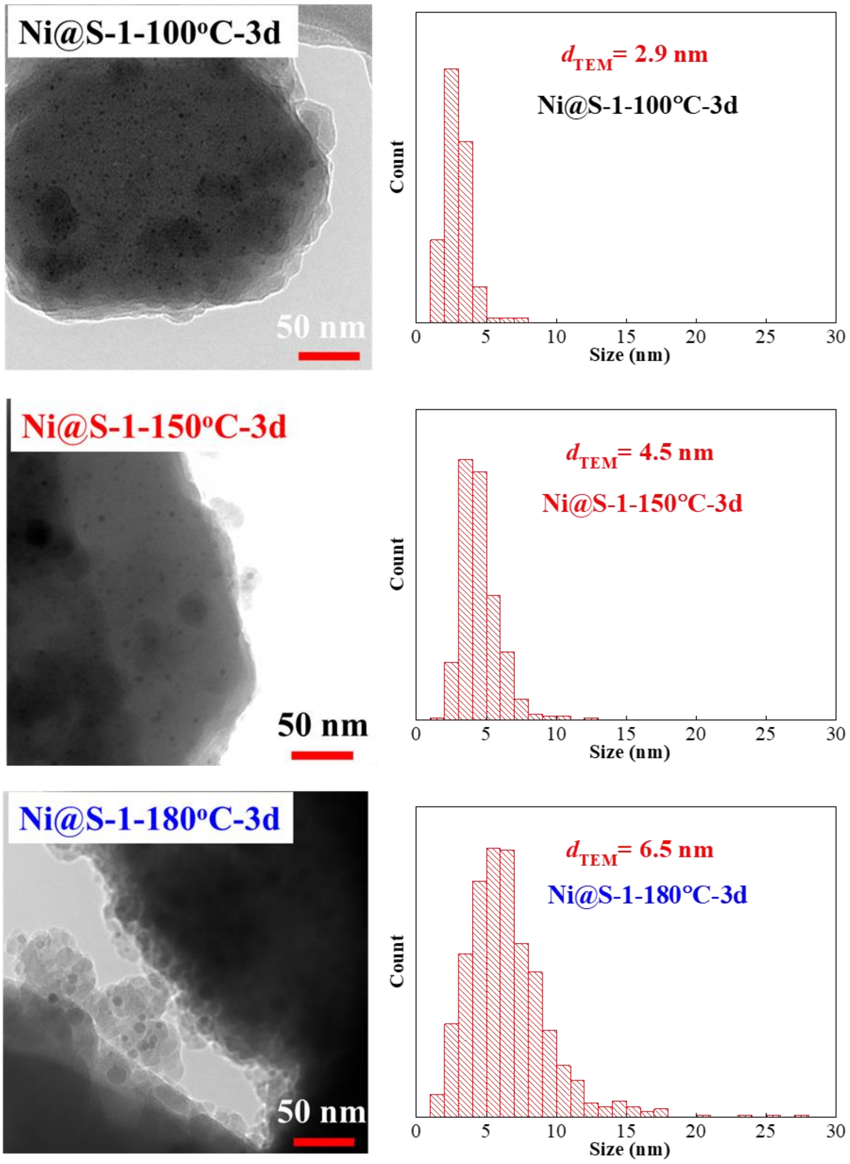

Figure 2.24. TEM images and corresponding Ni particle size distributions of the as-prepared samples after H_2 reduction at 850 °C for 1 h.

2.5.2. Confirmation of Ni location by DRM at 600 °C

Fig. 2.25 tells the DRM test results of the as-prepared Ni@S-1 catalysts. The Ni@S-1-100°C-3d could reach and maintain the equilibrium activity during the DRM reaction. At the same time, the CH_4 and CO_2 conversion rates of Ni@S-1-150°C-3d were slightly lower than that of equilibrium values. Notably, the Ni@S-1-180°C-3d catalyst showed a significant reduction in catalytic activity. Furthermore, Ni@S-1-150°C-3d and Ni@S-1-180°C-3d catalysts displayed a gaseous carbon recovery lower than 100%.

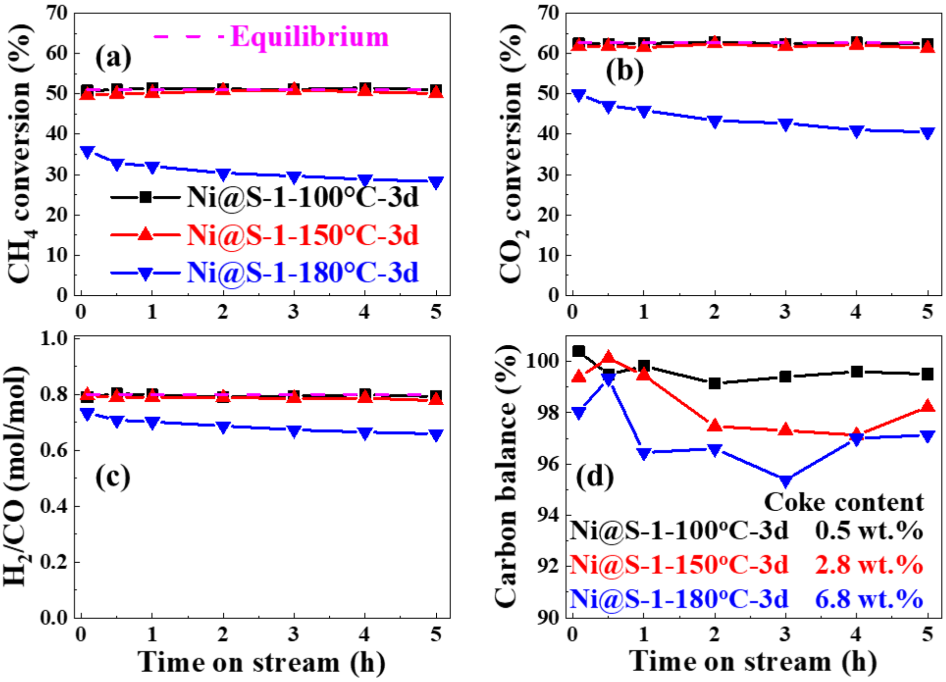

Figure 2.25. Catalytic performances of the as-prepared catalysts for DRM reaction as function of time on stream: (a) CH_4 conversion, (b) CO_2 conversion, (c) H_2/CO ratio, and (d) gaseous carbon recovery (reaction conditions: T= 600 °C, 1 bar, $CH_4/CO_2/Ar/He$= 20/20/40/10mL/min, GHSV= 2,000 L/g-Ni/h)

Combined with TG results in **inset of Fig. 2.25d** and SEM images of spent catalysts in **Fig. 2.26**, it is clear that the Ni@S-1 catalyst synthesized at higher HTS temperature accumulated more undesired carbon during the DRM reaction. In detail, the coke contents were 0.5 wt%, 2.8 wt%, and 6.8 wt% for Ni@S-1-100°C-3d, Ni@S-1-150°C-3d, and Ni@S-1-180°C-3d, respectively. This coke deposition endorsed the characterization results and verified that more Ni NPs located and aggregated on the surface of the Ni@S-1 catalysts prepared at higher synthesis temperatures.

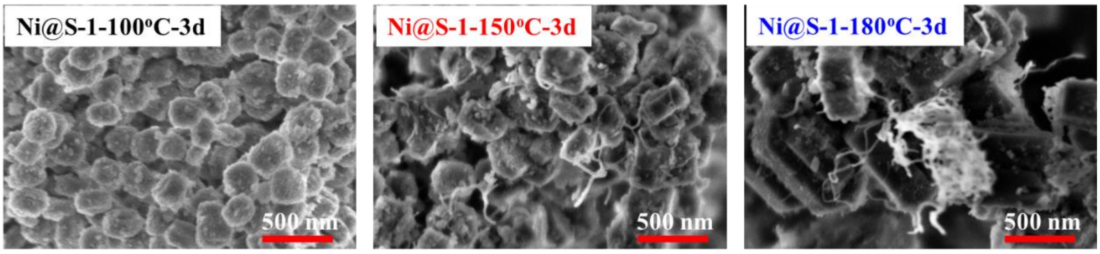

Figure 2.26. SEM images of the as-prepared samples after the DRM reaction.

In summary, these results shed light on that high HTS temperature could lead to high crystallization speed and facilitate the redissolution-recrystallization process. Therefore, the bigger crystal with fewer inter-crystalline mesopores and more Ni particles located on the outer surface of Silicalite-1 zeolite could be prepared. Consequently, the Ni@S-1 catalyst from higher synthesis temperature showed worse catalytic performances and higher coke content during the DRM reaction. In other words, the formation mechanism proposed in the last section was verified.

2.6. Conclusion

In this chapter, a new methodology for encapsulating ultrafine nickel (Ni) nanoparticles within Silicalite-1 zeolite (Ni@S-1) was developed and demonstrated. The novel aspect of this method is the utilization of Ni-PS powder as the nickel source, which has not been previously reported. This approach provides a simple and efficient means for producing Ni@S-1 with encapsulation structure. The effects of three key parameters, namely reactant concentration, hydrothermal treatment (HTS) time, and HTS temperature, on the structure and catalytic activity of Ni@S-1 were investigated. The optimal synthesis conditions were determined to be 100°C for a three-day HTS with an H_2O/SiO_2 ratio of 50. The mechanism of Ni@S-1 formation was also explored. The results showed that the synthesis involved the initial nucleation and growth of the zeolite, followed by encapsulation of Ni species (Ni-PS) within the inter-crystalline mesopores. Subsequently, redissolution and recrystallization of the zeolite (Ostwald ripening process) led to the dissolution of small crystals and growth of larger zeolite particles, resulting in the migration of Ni species from the inner regions of smaller zeolite crystals to the outer surface of larger zeolite with fewer mesopores.

Reference

(1) Alipour, Z.; Babu Borugadda, V.; Wang, H.; Dalai, A. K. Syngas Production through Dry Reforming: A Review on Catalysts and Their Materials, Preparation Methods and Reactor Type. *Chemical Engineering Journal* **2023**, *452*, 139416.

(2) Er-rbib, H.; Bouallou, C.; Werkoff, F. Dry Reforming of Methane - Review of Feasibility Studies. *Chem Eng Trans* **2012**, *29*, 163–168.

(3) Quiroga, M. M. B.; Luna, A. E. C. Kinetic Analysis of Rate Data for Dry Reforming of Methany. *Ind Eng Chem Res* **2007**, *46* (16), 5265–5270.

(4) Song, Q.; Ran, R.; Li, D.; Zhao, B.; Weng, D. Synthesis of Highly-Dispersed Ni/Mesoporous Silica via an Ammonia Evaporation Method for Dry Reforming of Methane: Effect of the Ni Loadings. *Catalysis Surveys from Asia* **2021**, *25* (3), 312–323.

(5) Gao, X.; Ge, Z.; Zhu, G.; Wang, Z.; Ashok, J.; Kawi, S. Anti-Coking and Anti-Sintering Ni/Al2O3 Catalysts in the Dry Reforming of Methane: Recent Progress and Prospects. *Catalysts* **2021**, *11* (8), 1003.

(6) Torrez-Herrera, J. J.; Korili, S. A.; Gil, A. Recent Progress in the Application of Ni-Based Catalysts for the Dry Reforming of Methane. *Catal Rev Sci Eng* **2021**.

(7) Baharudin, L.; Rahmat, N.; Othman, N. H.; Shah, N.; Syed-Hassan, S. S. A. Formation, Control, and Elimination of Carbon on Ni-Based Catalyst during CO2 and CH4 Conversion via Dry Reforming Process: A Review. *Journal of CO2 Utilization* **2022**, *61*, 102050.

(8) Liu, Y.; Chen, Y.; Gao, Z.; Zhang, X.; Zhang, L.; Wang, M.; Chen, B.; Diao, Y.; Li, Y.; Xiao, D.; Wang, X.; Ma, D.; Shi, C. Embedding High Loading and Uniform Ni Nanoparticles into Silicalite-1 Zeolite for Dry Reforming of Methane. *Appl Catal B* **2022**, *307*.

(9) Lu, Y.; Guo, D.; Zhao, Y.; Moyo, P. S.; Zhao, Y.; Wang, S.; Ma, X. Confined High Dispersion of Ni Nanoparticles Derived from Nickel Phyllosilicate Structure in Silicalite-2 Shell for Dry Reforming of Methane with Enhanced Performance. *Microporous and Mesoporous Materials* **2021**, *313*, 110842.

(10) Zhang, J.; Li, F. Coke-Resistant Ni@SiO2 Catalyst for Dry Reforming of Methane. *Appl Catal B* **2015**, *176–177*, 513–521.

(11) Park, J. C.; Bang, J. U.; Lee, J.; Ko, C. H.; Song, H. Ni@SiO2 Yolk-Shell Nanoreactor Catalysts: High Temperature Stability and Recyclability. *J Mater Chem* **2010**, *20* (7), 1239–1246.

(12) Wang, F.; Han, B.; Zhang, L.; Xu, L.; Yu, H.; Shi, W. CO2 Reforming with Methane over Small-Sized Ni@SiO2 Catalysts with Unique Features of Sintering-Free and Low Carbon. *Appl Catal B* **2018**, *235* (January), 26–35.

(13) Lu, Y.; Guo, D.; Zhao, Y.; Moyo, P. S.; Zhao, Y.; Wang, S.; Ma, X. Confined High Dispersion of Ni Nanoparticles Derived from Nickel Phyllosilicate Structure in Silicalite-2 Shell for Dry Reforming of Methane with Enhanced Performance. *Microporous and Mesoporous Materials* **2021**, *313*, 110842.

(14) Fujitsuka, H.; Kobayashi, T.; Tago, T. Development of Silicalite-1-Encapsulated Ni Nanoparticle Catalyst from Amorphous Silica-Coated Ni for Dry Reforming of Methane: Achieving Coke Formation Suppression and High Thermal Stability. *Journal of CO2 Utilization* **2021**, *53*, 101707.

(15) Chen, Y. Y.; Chang, Y. C.; Hung, W. Y.; Lin, H. P.; Shih, H. Y.; Xie, W. A.; Li, S. N.; Hsu, C. H. Green Synthesis of Porous Ni-Silicate Catalyst for Hydrogen Generation via Ammonia Decomposition. *Int J Energy Res* **2020**, *44* (12), 9748–9756.

(16) Sivaiah, M. v.; Petit, S.; Beaufort, M. F.; Eyidi, D.; Barrault, J.; Batiot-Dupeyrat, C.; Valange, S. Nickel Based Catalysts Derived from Hydrothermally Synthesized 1:1 and 2:1 Phyllosilicates as Precursors for Carbon Dioxide Reforming of Methane. *Microporous and Mesoporous Materials* **2011**, *140* (1–3), 69–80.

(17) Bian, Z.; Kawi, S. Preparation, Characterization and Catalytic Application of Phyllosilicate: A Review. *Catal Today* **2020**, *339*, 3-23.

(18) Čejka, J.; Corma, A.; Zones, S. *Zeolites and Catalysis: Synthesis, Reactions and Applications.* **2010**.

(19) Zhang, H.; Samsudin, I. bin; Jaenicke, S.; Chuah, G.-K. Zeolites in Catalysis: Sustainable Synthesis and Its Impact on Properties and Applications. *Catal Sci Technol* **2022**, *12* (19)

(20) Yang, M.; Jin, P.; Fan, Y.; Huang, C.; Zhang, N.; Weng, W.; Chen, M.; Wan, H. Ammonia-Assisted Synthesis towards a Phyllosilicate-Derived Highly-Dispersed and Long-Lived Ni/SiO2 Catalyst. *Catal Sci Technol* **2015**, *5* (12), 5095–5099.

(21) Zhang, Y.; Liu, Q. Nickel Phyllosilicate Derived Ni/SiO2 Catalysts for CO2 Methanation: Identifying Effect of Silanol Group Concentration. *Journal of CO2 Utilization* **2021**, *50*, 101587.

(22) Ashok, J.; Kathiraser, Y.; Ang, M. L.; Kawi, S. Ni and/or Ni-Cu Alloys Supported over SiO2 Catalysts Synthesized via Phyllosilicate Structures for Steam Reforming of Biomass Tar Reaction. *Catal Sci Technol* **2015**, *5* (9), 4398–4409.

(23) IYOKI, K.; ONISHI, T.; ANDO, M.; SUKENAGA, S.; SHIBATA, H.; OKUBO, T.; WAKIHARA, T. Reduction of Crystal Size of Silicalite-1 Synthesized in Fluoride-Containing Media via Multi-Stage Heating with Intermediate Stirring. *Journal of the Ceramic Society of Japan* **2022**, *130* (1), 21139.

(24) Čejka, J.; Bekkum, H. van; Corma, A. *Introduction to Zeolite Science and Practice*, 3rd Revised Edition. Elsevier, **2007**.

(25) Zhang, Y.; Che, S. One-Pot Synthesis and Formation Mechanism of Hollow ZSM-5. *Chemistry – A European Journal* **2019**, *25* (24), 6196–6202.

(26) Mintova, S.; Fieres, B.; Bein, T. Crystal Growth of Nanosized LTA Zeolite from Precursor Colloids; **2002**, *142*, 223–229.

(27) Slezov, V. v.; Schmelzer, J.; Möller, J. Ostwald Ripening in Porous Materials. *J Cryst Growth* **1993**, *132* (3–4), 419–426.

(28) Li, Z.; Mo, L.; Kathiraser, Y.; Kawi, S. Yolk-Satellite-Shell Structured Ni-Yolk@Ni@SiO2 Nanocomposite: Superb Catalyst toward Methane CO2 Reforming Reaction. *ACS Catal* **2014**, *4* (5), 1526–1536.

(29) Pang, T.; Yang, X.; Yuan, C.; Elzatahry, A. A.; Alghamdi, A.; He, X.; Cheng, X.; Deng, Y. Recent Advance in Synthesis and Application of Heteroatom Zeolites. *Chinese Chemical Letters* **2021**, *32* (1), 328–338.

(30) Lei, Q.; Wang, C.; Dai, W.; Wu, G.; Guan, N.; Li, L. Multifunctional Heteroatom Zeolites: Construction and Applications. *Front Chem Sci Eng* **2021**, *15* (6), 1462–1486.

(31) Wu, Q.; Xu, C.; Zhu, L.; Meng, X.; Xiao, F. S. Recent Strategies for Synthesis of Metallosilicate Zeolites. *Catal Today* **2022**, *390–391*, 2–11.

(32) Monpezat, A.; Topin, S.; Thomas, V.; Pagis, C.; Aouine, M.; Burel, L.; Cardenas, L.; Tuel, A.; Malchère, A.; Epicier, T.; Farrusseng, D.; Roiban, L. Migration and Growth of Silver Nanoparticles in Zeolite Socony Mobil 5 (ZSM-5) Observed by Environmental Electron Microscopy: Implications for Heterogeneous Catalysis. *ACS Appl Nano Mater* **2019**, *2* (10), 6452–6461.

(33) Čejka, J.; Corma,, A.; Zone, S. *Zeolites and Catalysis: Synthesis, Reactions and Applications.* Wiley-VCH, **2010**.

(34) Vetter, T.; Iggland, M.; Ochsenbein, D. R.; Hänseler. Modeling Nucleation, Growth, and Ostwald Ripening in Crystallization Processes: A Comparison between Population Balance and Kinetic Rate Equation. *Cryst Growth Des* **2013**, *13* (11), 4890–4905.

(35) Nanev, C. N. On Some Aspects of Crystallization Process Energetics, Logistic New Phase Nucleation Kinetics, Crystal Size Distribution and Ostwald Ripening. *J Appl Crystallogr* **2017**, *50* (4), 1021–1027.

(36) Madras, G.; McCoy, B. J. Temperature Effects on the Transition from Nucleation and Growth to Ostwald Ripening. *Chem Eng Sci* **2004**, *59* (13), 2753–2765.

Chapter 3. Evaluation and Comparison of Ni-loaded catalyst for the DRM reaction

3.1. Introduction

The DRM process has yet to be commercial application due to the absence of highly active, durable, and cost-effective catalyst[1–4]. According to the thermodynamics calculation in **Fig. 3.1a**, the reaction temperature should be higher than 750 °C to achieve a high single-pass conversion (>90%) of CH_4 and CO_2, but the metal sintering of the employed catalyst was favorable to occur at such high temperatures[5–7]. On the other hand, the DRM reaction is a strongly endothermic reaction, as cartooned in **Fig.3.1b**, a distinct temperature gradient would be induced in the catalyst bed after feeding the reactant gas. In other words, the temperature of the catalyst bed in some regions would be greatly decreased to the temperature that favors carbon formation (< 700 °C). If so, the coke would accumulate and deactivate the employed catalyst. Therefore, it is necessary to develop a catalyst with high activity and excellent sintering and coking resistance for DRM reaction.

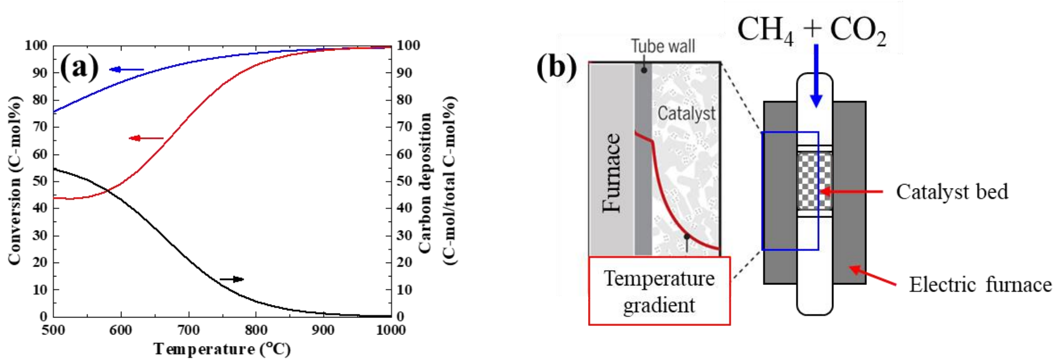

Figure 3.1. (a)the thermodynamic calculation of DRM reaction. (Reaction conditions: CH_4: CO_2: Ar = 2: 2: 5, 1 bar) and (b) a cartoon image of a fixed DRM bed.

In **Chapter 2**, we successfully developed Silicalite-1-encapsulated Ni catalyst (Ni@S-1) by a new method, in which direct addition of Ni-PS as Ni source into the zeolite mother liquid, followed by hydrothermal synthesis (HTS) at 100 °C for three days. The Ni-PS was confined within the S-1 particle, and ultrafine Ni particles were successfully formed in the inter-crystalline pore of the S-1 particle after reduction (Ni@S-1).

In this chapter, the resulting Ni@S-1 catalyst from Ni-PS was evaluated for DRM reaction under different conditions to confirm its suppression of coke formation, resistance to Ni sintering, and longevity. For comparison, the Ni/S-1 catalyst with most Ni NPs supported on the surface of Silicalite-1 zeolite was prepared by impregnation method, and the Ni/SiO_2 catalyst with poor thermal stability was obtained from reduction of Ni-PS/SiO_2. Then, based on the DRM catalytic performances and characterization results of the as-prepared catalysts, the insights on the structure-activity relationship was elucidated.

3.2. Experimental

3.2.1. Chemicals

The details of chemicals used have been described in the **Chapter 2**.

3.2.2. Catalyst Preparation

Three Ni-loaded catalysts were prepared to compare the catalytic performances of catalysts with different structures and properties.

(1) Preparation of 1 wt% Ni@S-1 catalyst with most Ni NPs encapsulated inside Silicalite-1 zeolite by two-step method (Fig. 3.2)

Step 1. Preparation of 3 wt.% Ni-PS/SiO_2 by HTS method**.**

Table 3.1. Preparation conditions of 3wt% Ni-PS/SiO_2

Parameter	Theoretical value
Ni loading	3 wt%
H_2O/Si	34 mol/mol
NH_3/Ni	60 mol/mol
HTS temperature	100 °C
HTS time	3 days

1) added calculated amounts of 1M of $Ni(NO_3)_2$ aqueous solution to diluted 3.0 M of ammonia solution to form the nickel ammonia complex solution.

2) Si source, TEOS, was added to the above nickel ammonia complex solution and stirring for 2 h.

3) transferred the mixture into Teflon-lined autoclave reactor and hydrothermal treated at 100 °C for three days.

4) washed samples with distilled water three times and recovered the samples by centrifugation.

5) dried at 110 °C overnight.

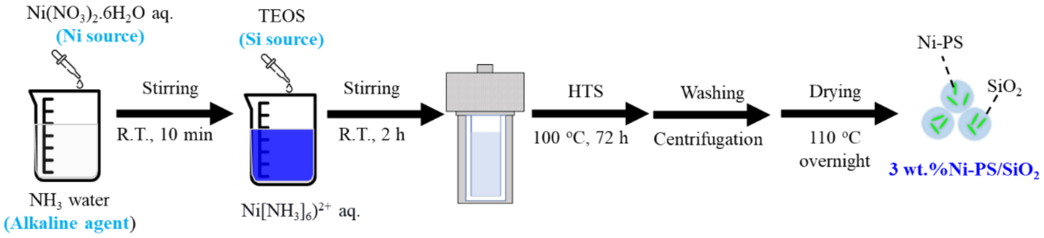

Figure 3.2. Preparation procedures of 3 wt.% Ni-PS/SiO_2.

Step 2. Preparation of 1 wt% Ni@S-1 catalyst using the as-prepared 3 wt% Ni-PS/SiO_2 as the Ni source by HTS method **(Fig. 3.3)**

Table 3.2. Preparation conditions of study on effect of reactants concentration

Parameter	Theoretical value
Ni loading	1 wt%
Si/TPAOH	3 mol/mol
Si_{PS}/Si_{TEOS}	0.49 mol/mol
H_2O/Si	50 mol/mol
Volume of zeolite mother liquor	75 mL (100 mL of autoclave reactor)
HTS temperature	100 °C
HTS time	3 days

1) preparation of zeolite mother liquor by mixing calculated amounts of TEOS, TPAOH, and distilled water at room temperature for 24 h to form a homogenous gel.

2) added designated amount of the 3 wt.% Ni-PS/SiO_2 precursor to the zeolite mother liquor and stirring for 2 h.

3) transferred into a Teflon-sealed autoclave and hydrothermally treated at 100 °C for three days in a tumbling oven.

4) washed samples with distilled water three times and recovered the samples by centrifugation.

5) dried at 110 °C overnight and calcined at 550 °C for 12 h.

6) reduced in 50 vol% H_2 at 850 °C for 1 h.

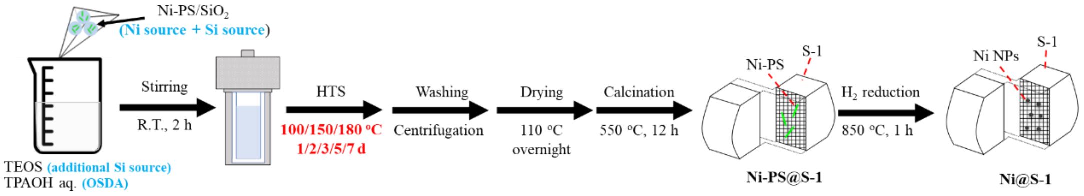

Figure 3.3. Preparation procedures of Ni@S-1

(2) Preparation of 1 wt% Ni/S-1 catalyst with most Ni NPs supported on the external surface of Silicalite-1 zeolite by impregnation method

Table 3.3. Preparation conditions of study on effect of reactants concentration

Parameter	Theoretical value
Ni source	Ni-PS
Ni loading	1 wt%
Si/TPAOH	3 mol/mol
H_2O/Si	50 mol/mol
Volume of zeolite mother liquor	75 mL (100 mL of autoclave reactor)
HTS temperature	180 °C
HTS time	3 days

1) preparation of zeolite mother liquor by mixing calculated amounts of TEOS, TPAOH, and distilled water for 24 h to form a homogenous gel.

2) transferred the resulting gel into a Teflon-sealed autoclave and hydrothermally treated at 180 °C for three days in a tumbling oven

3) washed samples with distilled water three times and recovered the samples by centrifuge

4) drying at 110 °C overnight and calcined at 550 °C for 12 h.

5) dropwise added calculated concentration and amount of nickel nitrate solution dissolved in anhydrous ethanol to the obtained Silicalite-1 zeolite.

6) blended for 30 min to uniformly disperse the Ni species.

7) dried at room temperature overnight and then dried at 110 °C for 3 h

8) calcined at 550 °C for 12 h.

9) reduced in 50 vol%H_2 at 850 °C for 1 h.

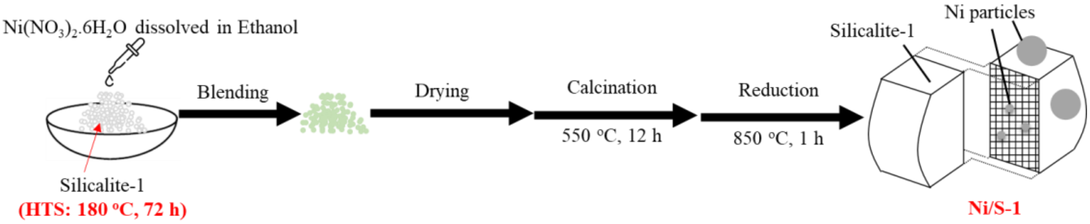

Figure 3.4. Preparation procedures of Ni/S-1 by impregnation method

(3) Preparation of 1 wt% Ni/SiO_2catalyst with poor thermal stability from 1 wt% Ni-PS/SiO_2 by HTS method

Table 3.4. Preparation conditions of study on effect of reactants concentration

Parameter	Theoretical value
Ni source	$Ni(NO_3)_2$ aq.
Ni loading	1 wt%
H_2O/Si	34 mol/mol
NH_3/Ni	120 mol/mol
HTS temperature	100 °C
HTS time	3 days

1) added calculated amounts of 1M of $Ni(NO_3)_2$ aqueous solution to diluted 2.0 M of ammonia solution. Next, Si source, TEOS, was added to the above nickel ammonia complex solution and stirring for 2 h.

2) transferred the mixture into Teflon-lined autoclave reactor and hydrothermally treated at 100 °C for three days.

3) washed samples with distilled water three times and recovered the samples by centrifuge. Then, dried at 110 °C overnight and calcined in air at 550 °C for 12 h.

4) reduced in 50 vol% H_2 at 850 °C for 1 h.

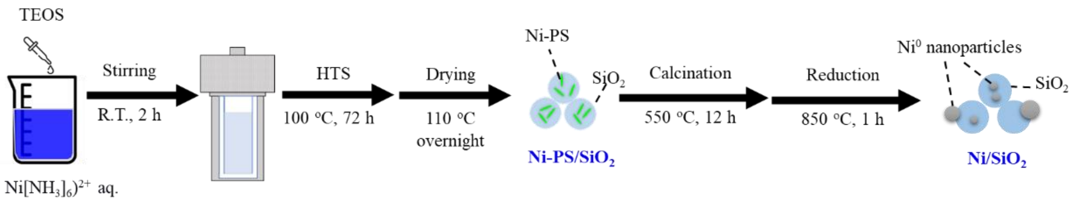

Figure 3.5. Preparation procedures of Ni/SiO_2 by HTS method

3.2.3 Catalyst Characterization

The characterization methods and corresponding acquired information are listed in **Table 3.5**. The measurement conditions were explained in the **Chapter 2**.

Table 3.5. Characterization techniques and corresponding acquired information

Characterization	Acquired information
XRF	Ni loading
SEM	Catalyst morphology
TEM	Ni location, Ni particle size, and carbon formation
XRD	Crystallographic information
N_2-sorption	Porosity, surface area, and pore volume
H_2-TPR	The reducibility of Ni
TG-DTA	Coke content

3.2.4 Catalytic Performance Evaluation

The catalyst was evaluated in a down-flow fixed bed reactor as illustrated in the **Chapter 2**. The evaluation conditions are listed in **Table 3.6**. The GHSV values were calculated on the mass basis of nickel and adjusted by diluting the catalyst with blank Silicalite-1 to change the absolute amount of catalyst loaded into the reactor.

Table 3.6. Catalytic evaluation conditions for the DRM reaction

Pressure	1 bar
H_2 reduction	60 mL/min of 50 vol.% H_2/N_2, 850°C, 1h
DRM temperature	600 °C--- coke resistance 850 °C--- Ni sintering and thermal stability
Reactant gas	CH_4: CO_2: Ar: He = 20: 20: 40: 10 mL/min
GHSV	2,000 L/g-Ni/h. or 40,000 L/g-Ni/h

3.3. Results and discussion

3.3.1 Characterization of the as-prepared samples

The as-prepared catalysts were characterized by several characterization techniques As indicated by the XRD patterns in **Fig. 3.6**, Ni@S-1 and Ni/S-1 exhibit characteristic diffraction peaks corresponding to Silicalite-1 zeolite (JCPDS 44-0696), suggesting the well-crystallized MFI zeolite was synthesized. On the contrary, the diffraction pattern of reference Ni-PS has only a very broad peak and no peaks indicative of crystalline phases, indicating the presence of fully amorphous SiO_2. Notably, no NiO or other Ni species were detected by XRD observed over all three samples because of its lower loading content and good dispersion of the very small NiO particles. As shown in **Fig. 3.6b**, there were no distinct differences in peak position and intensity of XRD patterns before and after H_2 reduction, showing the high thermal stability of the Silicate-1 zeolite. Besides, the characteristic peaks of metallic Ni or other Ni species were not found in all the catalysts, identifying the formation of ultrafine and highly dispersed Ni NPs in each catalyst.

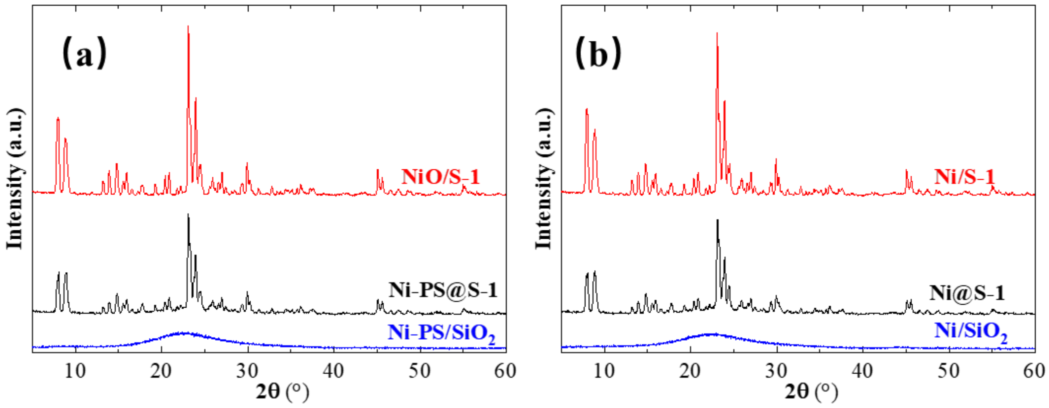

Figure 3.6. XRD patterns of the as-prepared catalysts: (a) after calcination at 550 °C for 12 h and (b) after H_2 reduction at 850 °C for 1 h

These results were consistent with the SEM observation in **Fig. 3.7**. The Ni-PS@S-1 and NiO/S-1 catalysts showed typical morphology of MFI zeolite. For comparison, the Ni-PS/SiO_2 exhibited the totally irregular and randomly distributed shape, which is consistent with that typically observed for amorphous silica.

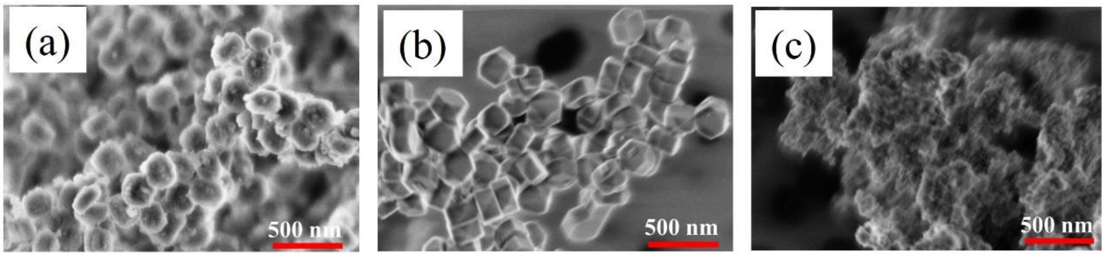

Figure 3.7. SEM images of the as-prepared catalysts after calcination: (a) Ni-PS@S-1, (b) NiO/S-1, and (c) Ni-PS/SiO_2

Table 3.7 lists the Ni loading of the samples measured by XRF. All the three samples exhibited comparable Ni loading to the nominal value. Hence, most Ni atoms were recovered during the preparation. **Fig. 3.8** presents the nitrogen adsorption–desorption isotherms of the samples after H_2 reduction, and the associated BET surface area and micropore volume results are summarized in Table 1. Ni@S-1 with $S_{BET} = 459$ m^2/g and $V_{micro.}= 0.12$ cm^3/g and Ni/S-1 with $S_{BET} = 441$ m^2/g and $V_{micro.}= 0.18$ cm^3/g exhibited the typical type I isotherms for microporous materials, indicating that the significant micropores were developed in these catalysts. In addition, compared to Ni/S-1, Ni@S-1 had an additional hysteresis loop (type H4) at the relative pressure of 0.7-0.9, which suggests the presence of mesopores in Ni@S-1. These mesopores could improve molecular diffusion and thus would be beneficial for the DRM reaction. In contrast, a relatively small N_2 uptake in the micropore filling stage was observed for

Ni/SiO_2, verifying that the Ni/SiO_2 sample contained a smaller number of micropore with a surface area of 137.6 m^2/g and micropore volume of only 0.01 cm^3/g. From the results of XRD and N_2 adsorption measurements, we can conclude that the Ni@S-1 with Silicalite-1 structure using Ni-PS/SiO_2 as Ni source was successfully prepared.

Table 3.7. Properties of the prepared catalysts after H_2 reduction at 850 °C for 1 h

	Ni@S-1	Ni/S-1	Ni/SiO_2
Ni loading[a] (wt.%)	0.99	1.02	0.97
BET surface area[b] (m^2/g)	459.3	440.5	137.6
Micropore volume[c] (cm^3/g)	0.119	0.180	0.01

[a]. Measured by XRF

[b]. Calculated by BET equation

[c]. Calculated by t-plot method

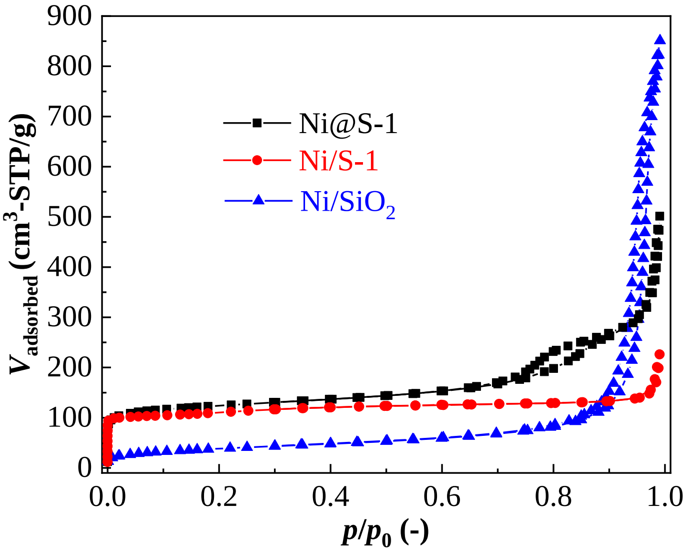

Figure 3.8. N_2 adsorption isotherms of the as-prepared catalysts after H_2 reduction at 850 °C for 1 h

Next, the H_2-TPR analysis was performed. **Fig. 3.9** depicts the hydrogen consumption as a function of temperature during the process of H_2-TPR. As the temperature increased, for the Ni/S-1 catalyst, a major and broad reduction peak ranging from 400 °C to 650 °C (peaked at ca. 560 °C) should be attributed to the reduction of NiO supported on the outer surface of Siliclaite-1 zeolite with weak interaction. Meanwhile, a minor peak at 700-900 °C was associated with NiO introduced into the zeolite channels with improved interaction[1]. In contrast, the large reduction peak at 600-900 °C for Ni-PS@S-1 and Ni-PS/SiO_2 was assigned to the reduction of Ni-PS to metallic Ni [8]. This illustrated the formation of Ni-PS in Ni-PS@S-1. Based on the findings above, the Ni species immobilized in Silicalite-1 showed strong metal-support interaction in comparison with the NiO deposited on the external surface of Silicalite-1 zeolite.

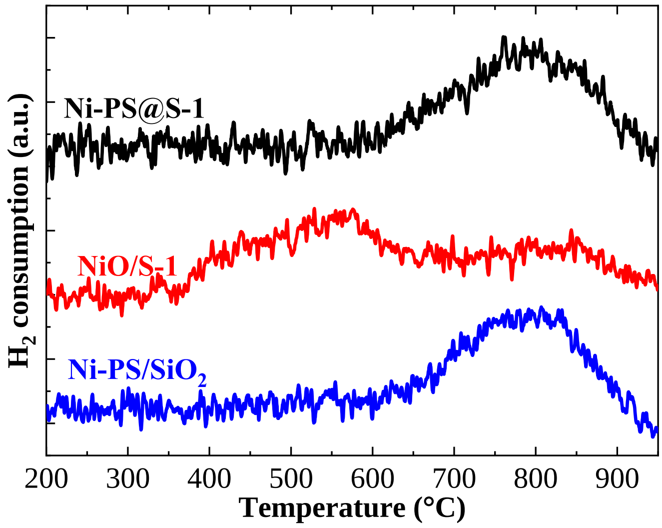

Figure 3.9. H_2-TPR profiles of the as-prepared catalysts

Then, after reduction by H_2 at 850 °C for 1 h, the TEM observations were undertaken to check the morphology and distribution of Ni particles. As presented in **Fig. 3.10a-b**, ultrafine Ni NPs in the Ni@S-1 sample were uniformly and well distributed over the S-1 host and had a narrow size distribution from 1 to 8 nm and average diameter of 2.9 nm, which is the expected size of Ni (< 7nm). This demonstrates that the Ni NPs should be embedded in the Silicalite-1 crystal, and hence this catalyst showed good anti-sintering. By contrast, as can be seen from **Fig. 3.10c-d**, Ni NPs with wider size distribution from 2 to 16 nm and with a larger mean size of 4.9 nm were detected for Ni/S-1, suggesting the agglomeration of Ni particles situated on the surface of the S-1 zeolite occurred in H_2 stream. For the Ni/SiO_2 sample from Ni-PS/SiO_2, Ni NPs were 4.3 nm in mean size and moderately distributed over the amorphous silica. The narrower size distribution of Ni NPs in Ni/SiO_2 compared to that of Ni/S-1 thanks to the stronger interaction between Ni species and silica of the phyllosilicate structure.

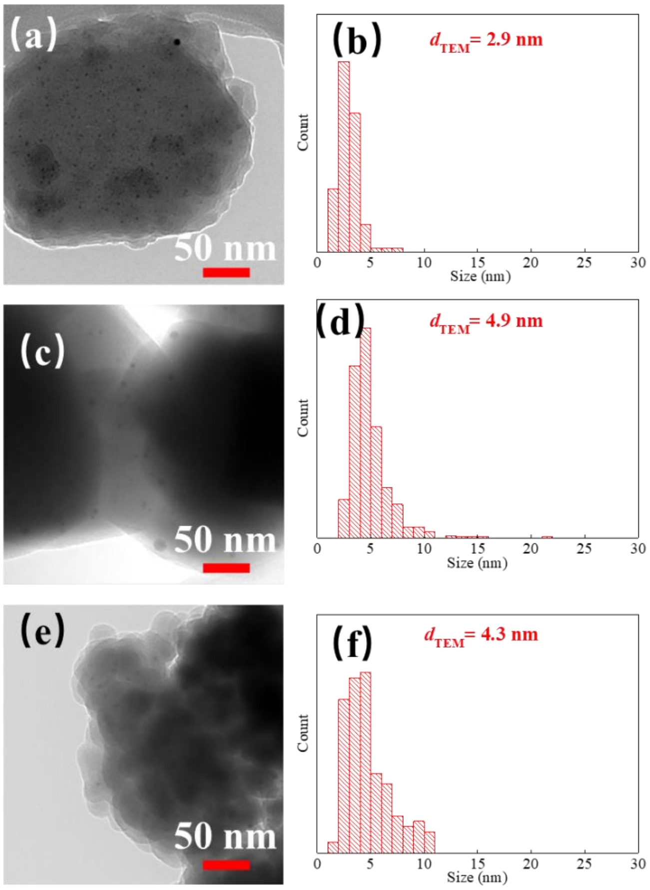

Figure 3.10. TEM images and corresponding Ni particle size distribution of (a–b) Ni@S-1, (c–d) Ni/S-1, and (e–f) Ni/SiO_2 after H_2 reduction at 850 °C for 1 h.

On the basis of the characterization results, we concluded that adding Ni-PS/SiO_2 as the Ni source to zeolite mother liquor, the Ni-PS was successfully anchored in Silicalite-1 crystal after HTS. Then, ultrafine Ni NPs could be formed and fixed within Silicalite-1 after H_2 reduction.

3.3.2. Evaluation of coking suppression for DRM at 600 °C

The anti-coking performance of Ni@S-1, Ni/S-1, and Ni/SiO_2 samples in DRM reaction was evaluated at 600 °C, where coke formation was preferable and speedy according to the calculation of thermodynamics. As shown in **Fig. 3.11**, Ni@S-1 and Ni/SiO_2 catalysts reached the thermodynamic equilibrium for CH_4 conversion, CO_2 conversion, and H_2/CO ratio and maintained their activity for 5 h, and the carbon balance for them was kept at ca. 100% during the reaction. All these imply that Ni@S-1 and Ni/SiO_2 exhibited high DRM activity and excellent ability for suppression of coke formation. Comparatively, the Ni/S-1 catalyst exhibited comparable CH_4 conversion, but lower CO_2 conversion, higher H_2/CO ratio, and lower carbon recovery in gaseous products than that of the former two catalysts, indicating that the side coke formation reactions, e.g., methane decomposition (**Equation 1**)[9] and/or the CO disproportionation reaction (**Equation 2**)[10], were promoted over Ni/S-1 catalyst.

$$CH_4 \longleftrightarrow C\ (\text{coke}) + H_2 \qquad \Delta_r H^{\circ}_{298\ K} = +75\ \text{KJ/mol} \qquad \text{Equation 1}$$

$$2CO \longleftrightarrow C\ (\text{coke}) + CO_2 \qquad \Delta_r H^{\circ}_{298\ K} = -171\ \text{KJ/mol} \qquad \text{Equation 2}$$

Next, TG measurement was employed to calculate the amount of coke deposited after the DRM reaction. As listed in **Fig. 3.12**, the accumulated coke contents were 0.5 wt.% for Ni@S-1 and 0.9 wt% for Ni/SiO_2, whilst it was 40.9 wt.% for Ni/S-1.

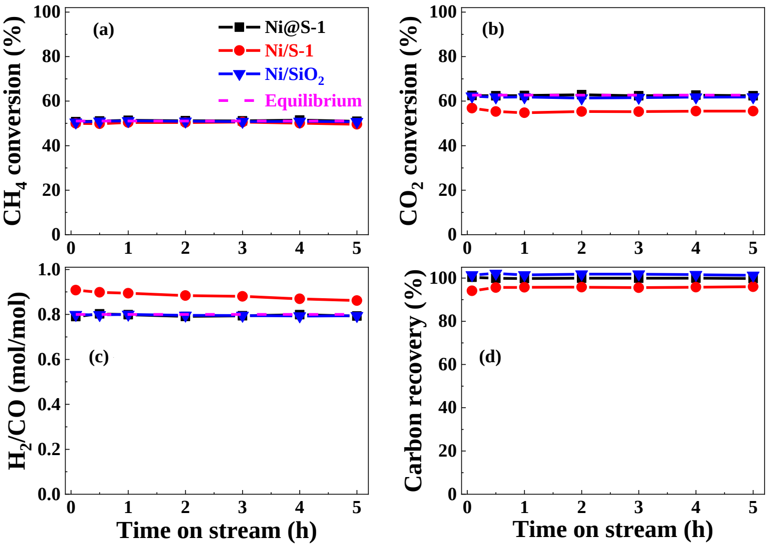

Figure 3.11. Catalytic performances of the as-prepared catalysts for the DRM reaction at 600°C as function of time on stream: (a) CH_4 conversion, (b) CO_2 conversion, (c) H_2/CO ratio, and (d) carbon balance and corresponding coke content after reaction in inset (reaction conditions: T= 600 °C, 1 bar, $CH_4/CO_2/Ar/$ He= 20/20/40/10mL/min, GHSV= 2,000 L/g-Ni/h)

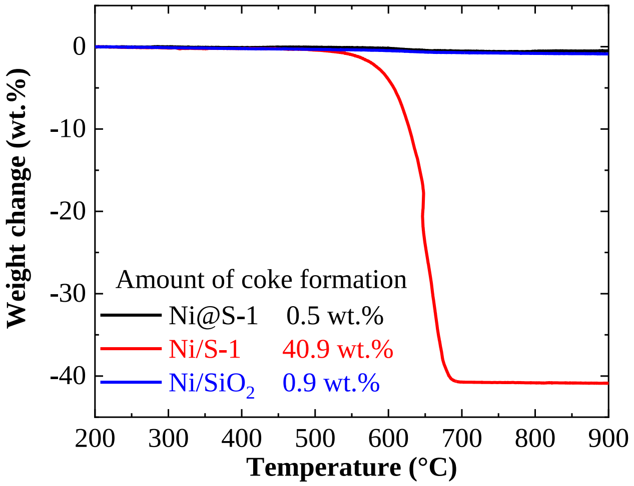

Figure 3.12. TG curves and corresponding coke contents of the spent catalysts after the DRM reaction at 600 °C for 5 h

Then, the morphology of the spent catalysts observed by SEM and TEM was carried out to confirm the coke accumulation. **Fig. 3.13** shows that negligible carbon species were observed on the spent Ni@S-1 and Ni/SiO$_2$ catalysts, whereas numerous filamentous carbons were found on the spent Ni/S-1 catalyst. These results coincide well with the results from the catalytic performances.

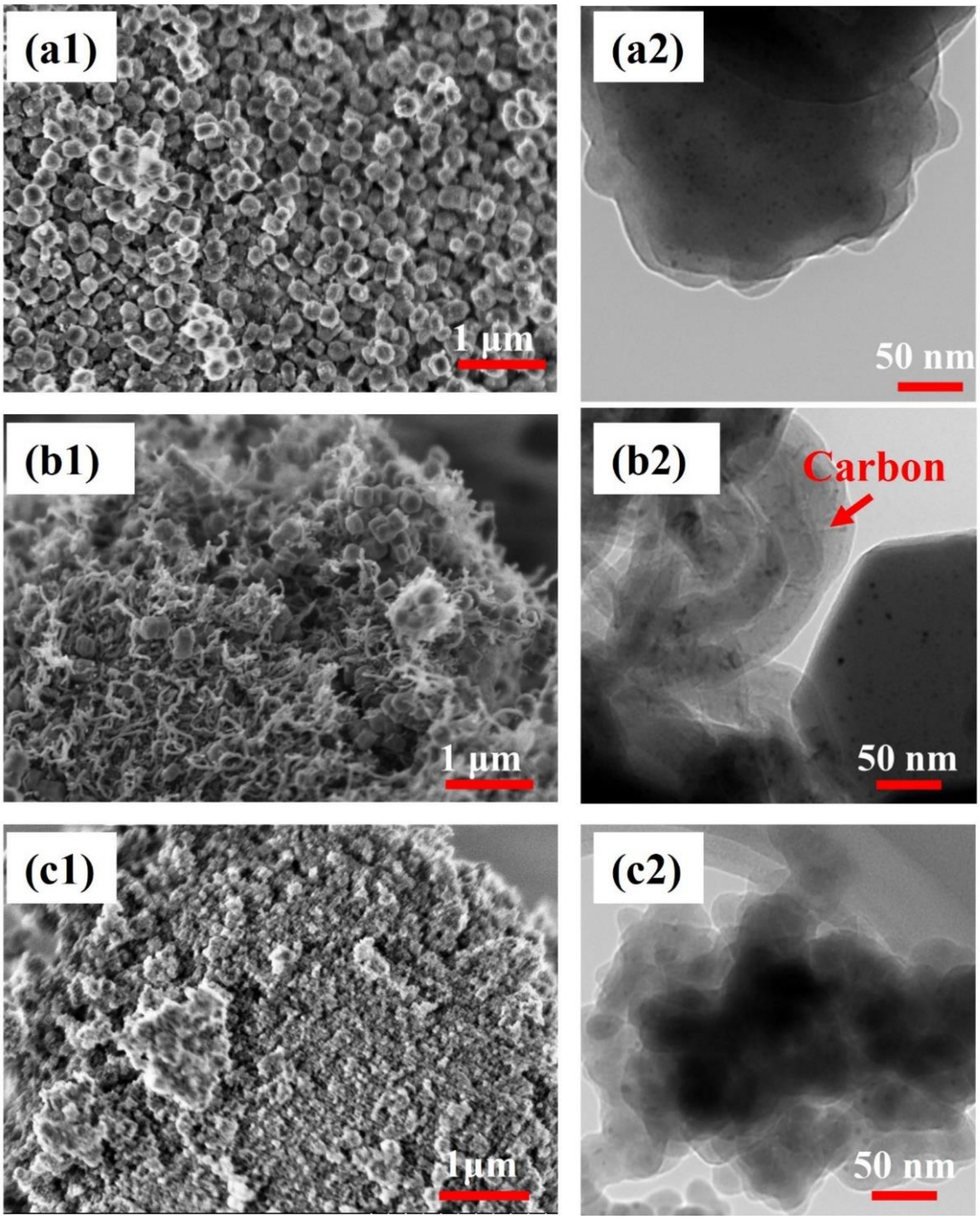

Figure 3.13. SEM (a1-c1) and TEM (a2-c2) images of spent catalysts after the DRM reaction at 600 °C for 5 h: (a) Ni@S-1, (b) Ni/S-1, and (c) Ni/SiO$_2$.

From these results, we can conclude that most of the Ni NPs of the Ni@S-1 catalyst should be confined inside the zeolite support, thus resulting in the internal space around the Ni NPs for coke deposition was limited, preventing the aggregation of the Ni particles. Therefore, the Ni catalysts with encapsulation structure could effectively inhibit coke formation. Contrarily, for the Ni/S-1 catalyst, relatively more Ni particles were located and exposed on the external surface of Silicalite-1with weak interaction, so the agglomeration of the Ni NPs easily occurred and tended to form larger particles. Consequently, the large amount of carbon was favorable to grow on its surface, manifesting the Ni/S-1 prepared by the conventional impregnation method was not suitable for industrial application. As for Ni/SiO_2 catalyst from Ni-PS/SiO_2, the good suppression of coke formation may be due to the strong metal-support interaction (SMSI) of phyllosilicate material. This SMSI could generate good resistance to Ni sintering and prevent the Ni species from forming large particles at moderate temperature, thus showing significant suppression towards coking[8,11].

3.3.3. Evaluation of thermal stability for DRM at 850 °C

Then, the Ni@S-1 and Ni/SiO$_2$ catalysts were further evaluated at 850 °C to investigate their resistance to Ni sintering and thermal stability. Not surprisingly, both catalysts reached thermodynamic equilibrium in **Fig. 3.14** due to the high reaction temperature and low GHSV employed, and hence the active sites and residence time are enough to achieve equilibrium values.

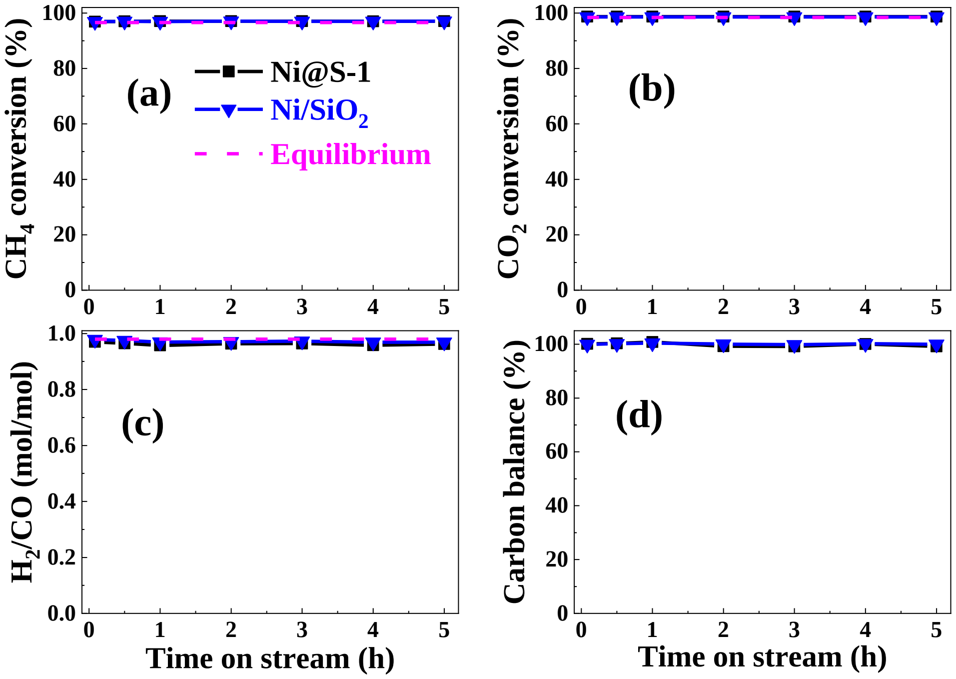

Figure 3.14. Catalytic performances of the as-prepared catalysts in the DRM reaction at 850°C as function of time on stream: (a) CH$_4$ conversion, (b) CO$_2$ conversion, (c) H$_2$/CO ratio, and (d) carbon balance (reaction conditions: T = 850 °C, 1 bar, CH$_4$/CO$_2$/Ar/ He = 20/20/40/10mL/min, GHSV=2,000 L/g-Ni/h)

More importantly, as shown in **Fig. 3.15**, the Ni NPs in the spent Ni@S-1 catalyst after reaction at 850 °C for 5 h were still well dispersed and the average size slightly increased to 4.3 nm in **Fig. 3.15b**. In contrast, the Ni/SiO$_2$ sample suffered from severe sintering, the average size of nickel particles dramatically increased to ca. 8.3 nm after reaction (**Fig. 3.15d**), and several nickel particles with diameters greater than 10 nm were detected.

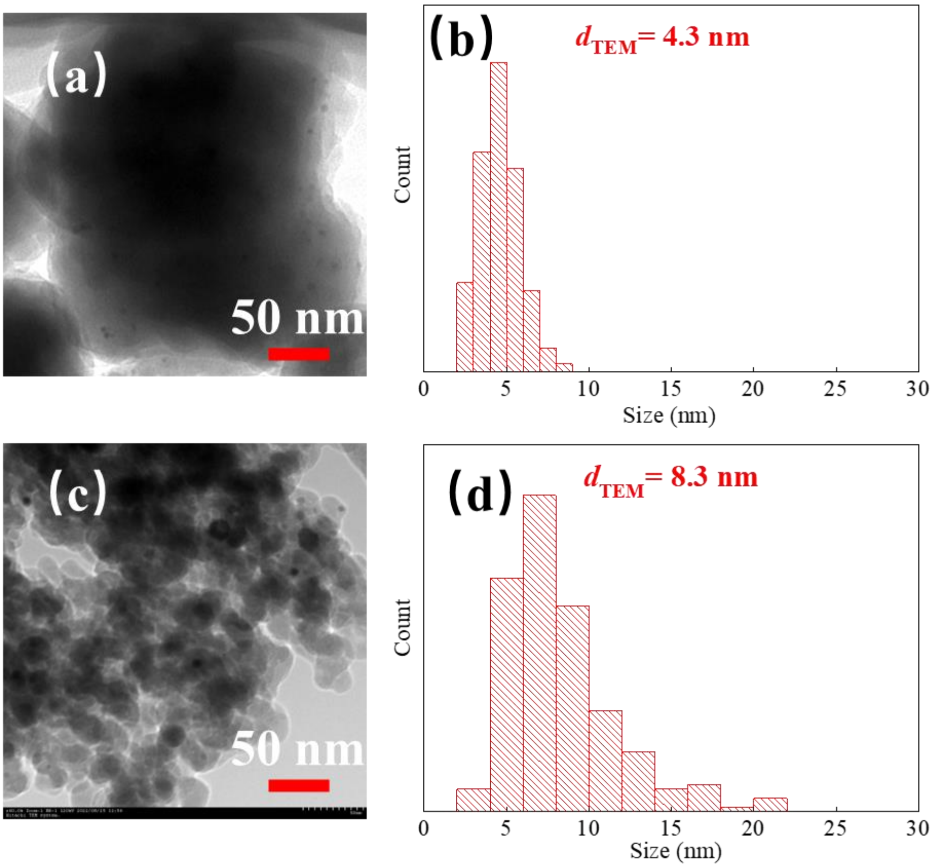

Figure 3.15. TEM images and corresponding Ni particle size distribution of (a–b) Ni@S-1 and (c–d) Ni/SiO_2 after DRM reaction at 850 °C for 5 h. (reaction conditions: T = 850 °C, 1 bar, CH_4/CO_2/Ar/ He = 20/20/40/10mL/min, GHSV = 2,000 L/(g-Ni. h)) [Catalysts were diluted with blank support, e.g. blank Silicalite-1 for Ni@S-1 and blank amorphous silica for Ni-PS/SiO_2, to decrease the catalyst amount.]

Combined with the N_2 adsorption and XRD measurements in **Fig. 3.16** and **Table 3.4**, such discrepancy revealed that Silicalite-1 exhibited high thermal stability and the Ni nanoparticles confined in Silicalite-1 zeolite possessed good resistance to sintering. Contrarily, the structure of amorphous silica in Ni/SiO_2 collapsed and then serious Ni sintering occurred.

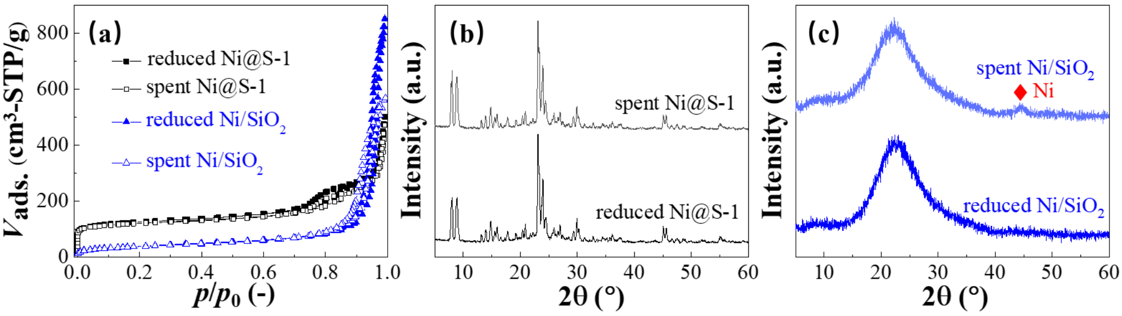

Figure 3.16. Characterizations of the reduced catalysts and spent catalysts after the DRM reaction at 850°C for 5 h (GHSV = 2,000 L/(g-Ni. h)): (a) N_2 adsorption isotherms, (b) and (c) XRD patterns

Table 3.8. Change in the BET surface areas (m^2/g) of Ni@S-1 and Ni/SiO_2 before and after DRM at 850 °C for 5 h (GHSV = 2,000 L/(g-Ni. h))

catalyst	reduced	spent
Ni@S-1	459.3	448.6
Ni/SiO_2	137.6	120.5

Finally, the longevity experiments over Ni@S-1 and Ni/SiO_2 catalysts were conducted at 850°C and GHSV of 40,000 L/g-Ni/h to clearly distinguish and examine the intrinsic activity, stability, and durability under severe conditions. As displayed in **Fig. 3.17**, Ni-PS showed lower initial activity than that of the Ni@S-1 owing to the larger Ni particle and less active sites in this catalyst. Furthermore, quick deactivation with the reaction time was detected for Ni/SiO_2. The CH_4 conversion, CO_2 conversion, and H_2/CO ratio declined significantly from 81.0%, 88.5%, and 0.89 to 73.8%, 83.6%, and 0.85, respectively, which verified the poor stability of the Ni-PS/SiO_2 at the high reaction temperature. In contrast, the initial conversions of CH_4 and CO_2 and products yield over Ni@S-1 catalyst almost reached thermodynamic equilibrium values even at such high GHSV, identifying its superior catalytic activity due to the presence of highly dispersed ultrafine Ni NPs. After running for 24 h, the CH_4 and CO_2 conversions slightly declined from 93.4% to 85.2% and 97.0% to 92.7%, respectively. As discussed in **Fig. 3.16**, the structure of Silicalite-1 was stable and almost unchanged after the reaction at 850°C, so the slight decrease in the activity of Ni@S-1 did not stem from the collapse of zeolite support. However, as depicted in **Fig.3.18**, the slight Ni sintering, namely, increased from 2.9 nm to 5.5 nm, of Ni@S-1 was detected after the reaction at 850°C for 24 h. This Ni sintering should be responsible for the slight decrease of catalytic activity with the time of Ni@S-1 catalyst at more severe conditions. Nonetheless, the Ni@S-1 catalyst still exhibited rather stable performance in comparison to the Ni/SiO_2 catalyst, it suffered from severe Ni sintering from 4.3 nm to 14.5 nm after the DRM reaction at 850°C for 5 h . Therefore, the Ni@S-1 could produce and maintain ultrafine Ni NPs due to the encapsulation structure and high thermal stability of the zeolite support, thereby showing high and stable DRM activity.

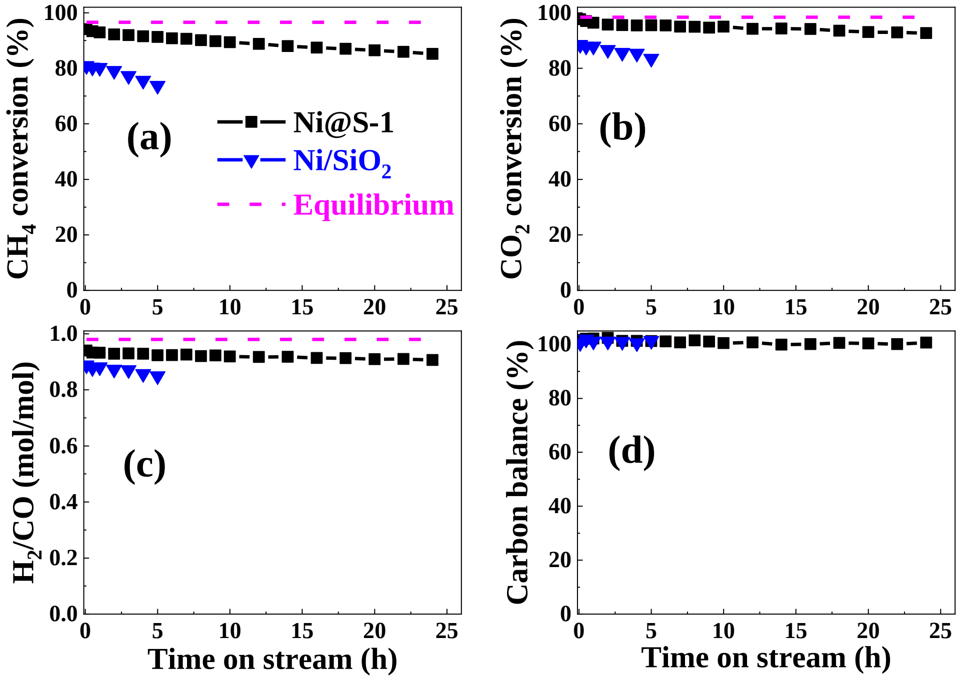

Figure 3.17. Catalytic performances of the as-prepared catalysts in DRM reaction at 850°C as function of time on stream: (a) CH_4 conversion, (b) CO_2 conversion, (c) H_2/CO ratio, and (d) carbon balance (reaction conditions: T = 850 °C, 1 bar, $CH_4/CO_2/Ar/He$ = 20/20/40/10mL/min, GHSV = 40,000 L/(g-Ni. h)) [Catalysts were diluted with blank support, e.g. blank Silicalite-1 for Ni@S-1 and blank amorphous silica for Ni-PS/SiO_2, to decrease the catalyst amount.]

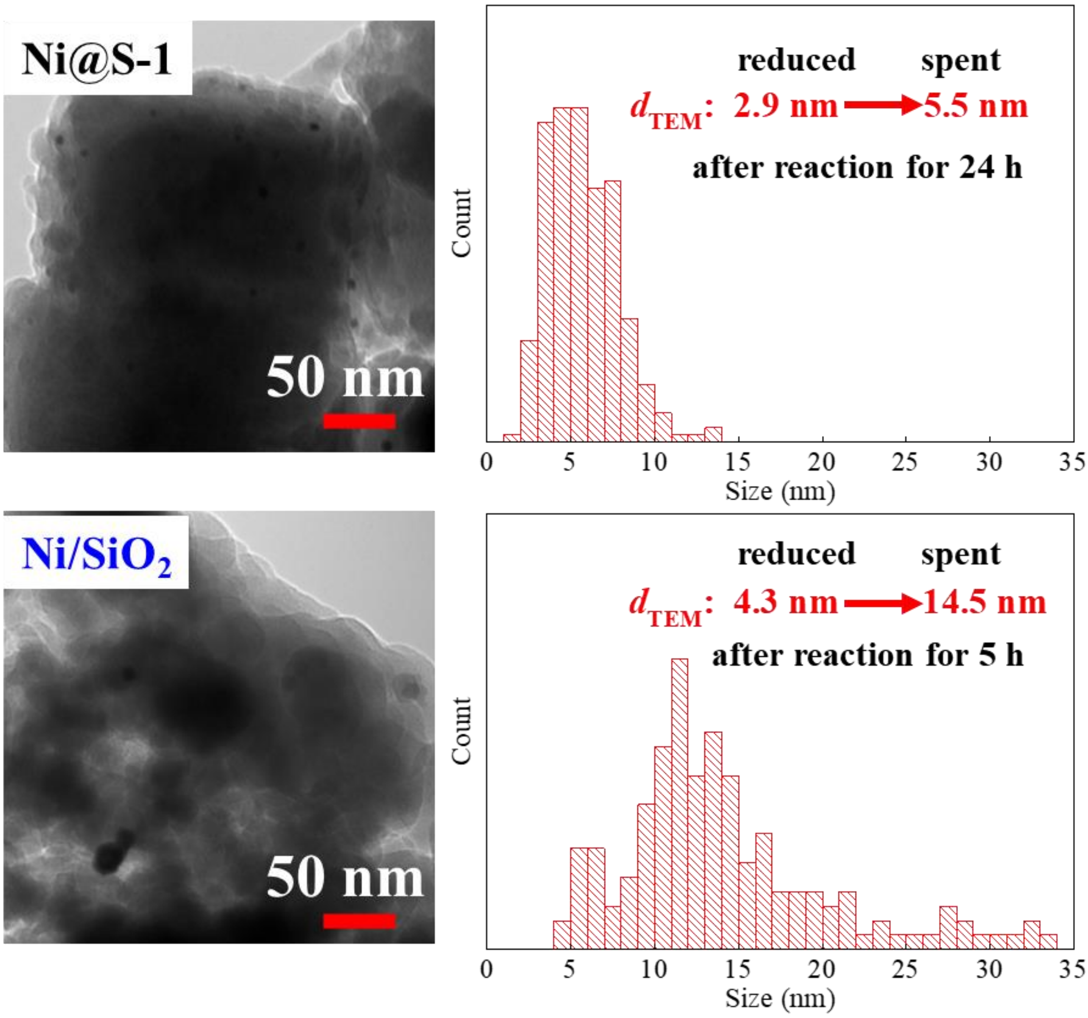

Figure 3.18. TEM images and corresponding Ni particle size distribution of (a–b) Ni@S-1 and (c–d) Ni/SiO$_2$ after DRM reaction at 850 °C (reaction conditions: T = 850 ºC, 1 bar, CH_4/CO_2/Ar/ He = 20/20/40/10mL/min, GHSV = 40,000 L/(g-Ni. h))

3.4. Conclusion

In this chapter, the catalytic performances of the Ni@S-1 catalyst prepared by using the Ni-PS as the Ni source for the DRM reaction were evaluated and compared with other reference Ni-loaded catalysts with different structures. The TEM, H_2-TPR, and XRD measurement results verified that the Ni phyllosilicate was embedded inside the Silicalite-1 zeolite after hydrothermal synthesis, leading to the formation of highly dispersed Ni nanoparticles with an average size of 2.9 nm confined in the Silicalite-1 zeolite after H_2 reduction. This Ni@S-1 catalyst exhibited better catalytic performances in DRM activity, coking suppression, and sintering resistance than the reference catalysts. Specifically, the Ni@S-1 catalyst reached thermodynamic equilibrium activities and showed negligible coke deposition of 0.5 wt.% at 600 °C for 5 h after the DRM reaction. Moreover, the encapsulation structure and high thermal stability of the Silicalite-1 support enabled Ni@S-1 to restrict the migration and aggregation of Ni NPs and thus keeping the ultrafine Ni NPs (< 7 nm) and exhibiting relatively high and stable catalytic performances at 850 °C for 24 h. Therefore, the Ni@S-1 using Ni-PS as the Ni source showed high suppression of coke formation and good resistance to Ni sintering due to the formation and maintenance of ultrafine Ni nanoparticles in thermally stable Silicalite-1 zeolite support. Accordingly, the Ni@S-1 catalyst from the Ni-PS was promising and attractive to meet the industrial application needs of the DRM reaction.

Reference

(1) Fujitsuka, H.; Kobayashi, T.; Tago, T. Development of Silicalite-1-Encapsulated Ni Nanoparticle Catalyst from Amorphous Silica-Coated Ni for Dry Reforming of Methane: Achieving Coke Formation Suppression and High Thermal Stability. *Journal of CO2 Utilization* **2021**, *53*, 101707.

(2) Xu, S.; Slater, T. J. A.; Huang, H.; Zhou, Y.; Jiao, Y.; Parlett, C. M. A.; Guan, S.; Chansai, S.; Xu, S.; Wang, X.; Hardacre, C.; Fan, X. Developing Silicalite-1 Encapsulated Ni Nanoparticles as Sintering-/Coking-Resistant Catalysts for Dry Reforming of Methane. *Chemical Engineering Journal* **2022**, *446*, 137439.

(3) Aramouni, N. A. K.; Touma, J. G.; Tarboush, B. A.; Zeaiter, J.; Ahmad, M. N. Catalyst Design for Dry Reforming of Methane: Analysis Review. *Renewable and Sustainable Energy Reviews* **2018**, *82*, 2570–2585.

(4) Aziz, M. A. A.; Setiabudi, H. D.; Teh, L. P.; Annuar, N. H. R.; Jalil, A. A. A Review of Heterogeneous Catalysts for Syngas Production via Dry Reforming. *J Taiwan Inst Chem Eng* **2019**, *101*, 139–158.

(5) Liu, Y.; Chen, Y.; Gao, Z.; Zhang, X.; Zhang, L.; Wang, M.; Chen, B.; Diao, Y.; Li, Y.; Xiao, D.; Wang, X.; Ma, D.; Shi, C. Embedding High Loading and Uniform Ni Nanoparticles into Silicalite-1 Zeolite for Dry Reforming of Methane. *Appl Catal B* **2022**, *307*.

(6) Abdullah, B.; Abd Ghani, N. A.; Vo, D. V. N. Recent Advances in Dry Reforming of Methane over Ni-Based Catalysts. *J Clean Prod* **2017**, *162*, 170–185.

(7) Huang, Q.; Fang, X.; Cheng, Q.; Li, Q.; Xu, X.; Xu, L.; Liu, W.; Gao, Z.; Zhou, W.; Wang, X. Synthesis of a Highly Active and Stable Nickel-Embedded Alumina Catalyst for Methane Dry Reforming: On the Confinement Effects of Alumina Shells for Nickel Nanoparticles. *ChemCatChem* **2017**, *9* (18), 3563–3571.

(8) Sivaiah, M. v.; Petit, S.; Barrault, J.; Batiot-Dupeyrat, C.; Valange, S. CO2 Reforming of CH4 over Ni-Containing Phyllosilicates as Catalyst Precursors. *Catal Today* **2010**, *157* (1–4), 397–403.

(9) Franz, R.; Tichelaar, F. D.; Uslamin, E. A.; Pidko, E. A. Dry Reforming of Methane to Test Passivation Stability of Ni/ Al2O3 Catalysts. *Appl Catal A Gen* **2021**, *612*, 117987.

(10) Er-rbib, H.; Bouallou, C.; Werkoff, F. Dry Reforming of Methane - Review of Feasibility Studies. *Chem Eng Trans* **2012**, *29*, 163–168.

(11) Bian, Z.; Li, Z.; Ashok, J.; Kawi, S. A Highly Active and Stable Ni-Mg Phyllosilicate Nanotubular Catalyst for Ultrahigh Temperature Water-Gas Shift Reaction. *Chemical Communications* **2015**, *51* (91), 16324–16326.

Chapter 4. Preparation of Ni@S-1 catalyst from Ni-PS with high Ni loading

4.1. Introduction

It is widely accepted that the number of active sites in catalyst is directly proportional to the catalytic activity, playing a critical role in the catalyst application. Normally, there are generally two strategies to increase the number of active sites: (i) increase the metal loading[1–5]; (ii) decrease the metal particle size[6,7]. Considering that the average diameter of nickel particles in the catalyst given in this study was already ultrafine, increasing Ni loading is the practical pathway to get higher mass-specific catalytic activity. Consequently, employing Ni@S-1 catalyst with high Ni loading can reduce the amount of catalyst in use and the size of the reactor, thus leading to higher catalytic efficiency and lower cost at the industrial level.

However, there is a trade-off between Ni loading and dispersion, say, the higher Ni loading of Ni@S-1 is favorable to the agglomeration of Ni NPs to reduce the Ni dispersion[8]. Furthermore, the incorporation of high contents of heteroatom, nickel, would enable the properties of the Ni@S-1 catalyst to change, such as destroying the Silicalite-1 zeolite structure and lowering the micropore area and volume of the support, thus leading to the failure of encapsulation of Ni NPs within the zeolite. Therefore, synthesizing Ni@S-1 catalyst with encapsulation structure and high Ni loading remains challenging

This chapter focused on preparing Ni@S-1 catalyst with high Ni loading. Additionally, the reason for the deterioration of the catalyst performance when the nickel content was higher than 2.5 wt% was also analyzed and proposed.

4.2. Experimental

4.2.1. Chemicals

The details of the chemicals used have been described in **Chapter 2**.

4.2.2. Catalyst Preparation

The Ni@S-1 catalyst was prepared by the same method as reported in the previous chapter. Differently, in the high Ni loading cases, the 10 wt.% Ni-PS/SiO_2 was prepared as precursor. In addition, the as-synthesized 10 wt.% Ni-PS/SiO_2 was calcined at first, and then added to the zeolite mother liquor to eliminate the adverse effect of impurities, e.g., ammonia, from the precursor on the zeolite crystallization.

Step 1. Preparation of 10 wt.% Ni-PS/SiO_2 by HTS method.

Table 4.1. Preparation conditions of 3wt% Ni-PS/SiO_2

Parameter	Theoretical value
Ni loading	10 wt%
H_2O/Si	50 mol/mol
NH_3/Ni	60 mol/mol
HTS temperature	100 °C
HTS time	3 d

1) added calculated amounts of 1M of $Ni(NO_3)_2$ aqueous solution to diluted 7.2 M of ammonia solution.

2) Si source, TEOS, was added to the above nickel ammonia complex solution and stirring for 2 h.

3) transferred the mixture into Teflon-lined autoclave reactor and hydrothermal treated at 100 ºC for three days.

4) washed samples with DI water three times and recovered the samples by centrifuge.

5) dried at 110 °C and then calcined at 550 ºC for 12 h.

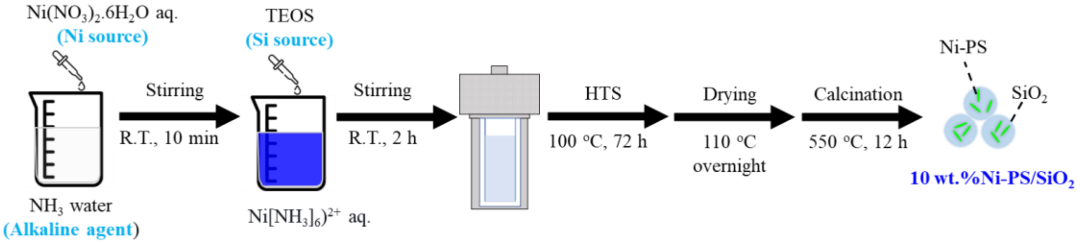

Figure 4.1. Preparation procedures of 10 wt.% Ni-PS/SiO_2

Step 2. Preparation of Ni@S-1 catalyst from Ni-PS by HTS method

Then, the Silicalite-1-encapsulated Ni nanoparticle catalysts with different Ni loadings were prepared by using the obtained 10 wt.% Ni-PS/SiO_2 powder as the Ni source. The preparation conditions and procedures are shown below and in the **Fig. 4.2.** Notably, considering the poor solubility of the calcined 10 wt.% Ni-PS/SiO_2, the precursor was added to zeolite mother liquor and stirred for 18 h.

1) preparation of zeolite mother liquor by mixing calculated amounts of TEOS, TPAOH, and DI water.

2) stirred the zeolite mother liquor for 6 h to form a homogenous gel.

3) added designated amount of the 10 wt.% Ni-PS/SiO_2 into the zeolite mother liquor and stirring for 18 h

4) transferred into a Teflon-sealed autoclave and hydrothermally treated at 100 °C for three days in a tumbling oven

5) washed samples with DI water three times and recovered the samples by centrifuge

6) drying at 110 °C overnight and calcined at 550 °C for 12 h.

7) reduced in 50 vol% H_2 at 850 °C for 1 h.

Table 4.2. Preparation conditions of study on effect of reactants concentration

Parameter	Theoretical value
Ni loading	1.5, 2.0, 2.5, and 3.0 wt%
Si/TPAOH	3 mol/mol
Si_{PS}/Si_{TEOS}	0.20 mol/mol for 1.5 wt% Ni@S-1
	0.29 mol/mol for 2.0 wt% Ni@S-1
	0.39 mol/mol for 2.5 wt% Ni@S-1
	0.51 mol/mol for 3.0 wt% Ni@S-1
H_2O/Si	50 mol/mol
Volume of zeolite mother liquor	75 mL (100 mL of autoclave reactor)
HTS temperature	100 °C
HTS time	3 days

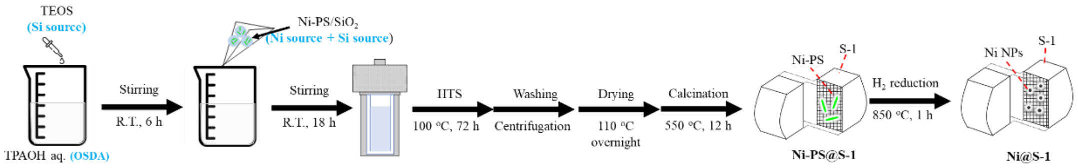

Figure 4.2. Preparation procedures of Ni@S-1.

4.2.3 Catalyst Characterization

The characterization methods and corresponding acquired information are listed in **Table 4.3**. The measurement conditions were explained in the **Chapter 2**.

Table 4.3. Characterization techniques and corresponding acquired information

Characterization	Acquired information
XRF	Ni loading
XRD	Crystallographic information
SEM	Catalyst morphology
TEM	Ni location, Ni particle size, and carbon formation
N_2-sorption	Porosity, surface area, and pore volume
H_2-TPR	The reducibility of Ni
TG-DTA	Coke content

4.2.4 Catalytic Performance Evaluation

The catalyst was evaluated in a down-flow fixed bed reactor as illustrated in **Chapter 2**. The evaluation conditions are listed in **Table 4.2**. The GHSV values were calculated on the mass basis of nickel and adjusted by diluting the catalyst with blank Silicalite-1 to change the absolute amount of catalyst loaded into the reactor.

Table 4.4. Catalytic evaluation conditions for the DRM reaction

Pressure	1 bar
H_2 reduction	60 mL/min of 50 vol.% H_2/N_2, 850°C, 1h
DRM temperature	600 °C--- coke resistance 850 °C--- Ni sintering and thermal stability
Reactant gas	CH_4: CO_2: Ar: He = 20: 20: 40: 10 mL/min
GHSV	2,000 L/g-Ni/h. or 40,000 L/g-Ni/h

4.3. Results and discussion

4.3.1. Characterization of the 10 wt% Ni-PS/SiO_2

Firstly, several instruments measured and characterized the as-synthesized 10 wt% Ni-PS/SiO_2 sample. As shown in **Table 4.5 and Fig. 4.3**, the actual Ni loading in the obtained sample is 8.36 wt%, slightly lower than the nominal value, which is attributed to the Ni loss during the HTS synthesis. Accordingly, this actual value was employed in the following preparation of the Ni@S-1 catalyst. The N_2-physisorption measurement in **Fig. 4.3a** and its corresponding analysis results in **Table 4.5** indicate that the resulting sample had very few pores. The XRD pattern in **Fig. 4.3b** presented a broad peak around 2θ of 15-30°, which was assigned to amorphous silica. Notably, two new discernible peaks at 35.8° and 60.7° were detected, which belong to the characteristic diffraction peaks of 2:1 Ni-PS. In contrast, no peak of crystalline NiO was detected.

TEM image is consistent with XRD observations. As pointed out by the red arrows in **Fig. 4.3c**, the needle-like Ni phyllosilicate was formed in the sample, and no noticeable NiO particles were observed**.** The H_2-TPR profile in **Fig. 4.3c** confirmed that only one reduction peak at 500-900 °C was ascribed to the reduction of 2:1 Ni-PS with a strong Ni-O-Si chemical bond to Ni[09,10]. These results verified that most of the nickel was taken from the raw material and utilized in forming Ni-PS.

Table 4.5. Properties of the prepared sample

Characterization	Ni loading[a] (wt.%)	S_{BET}[b] (m^2/g)	V_{micro}[c] (cm^3/g)
Result	8.36	5.8	0.002

[a]. Measured by XRF

[b]. Calculated by BET equation

[c]. Calculated by t-plot method

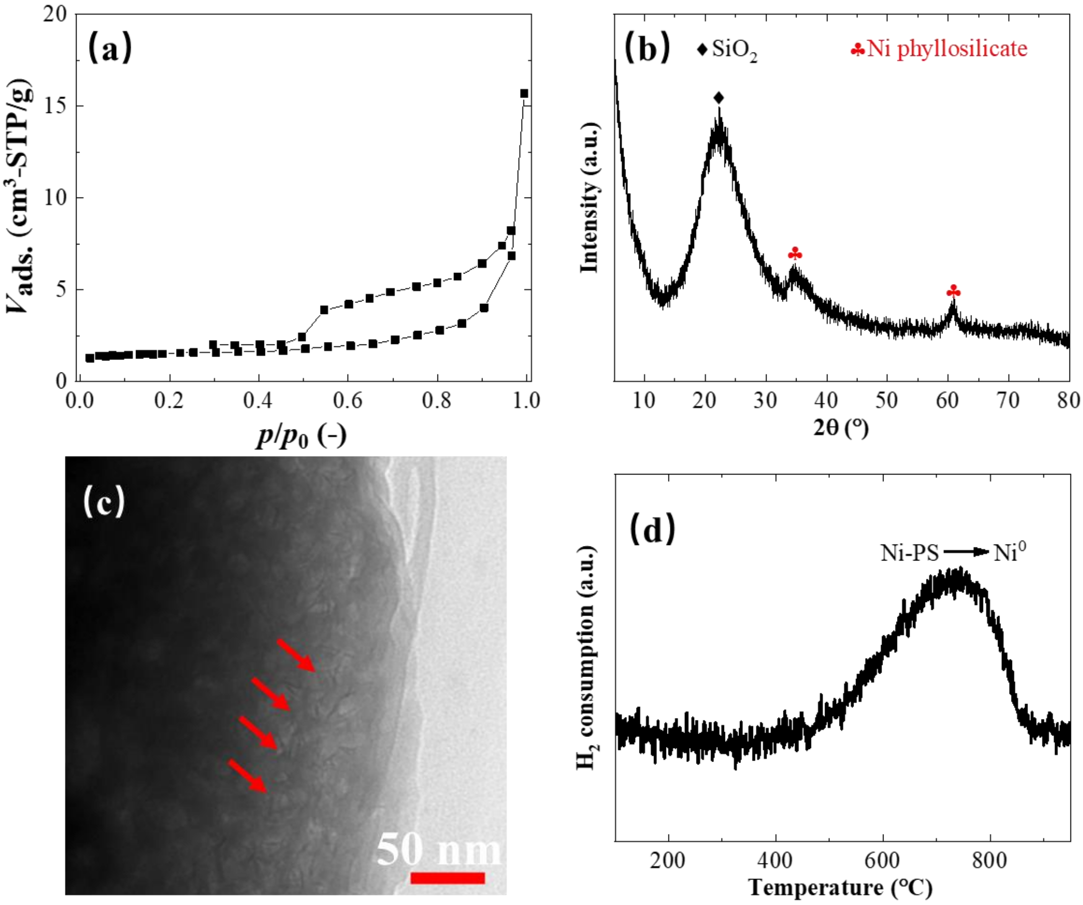

Figure 4.3. The characterization results of the as-prepared 10 wt% Ni-PS/SiO$_2$: (a) N$_2$-physisorption isotherms, (b) XRD pattern, (c) TEM image, and (d) H$_2$-TPR profile.

4.3.2. Characterization of the as-prepared Ni@S-1 samples

The actual Ni loadings measured by XRF are listed in **Table 4.6**. All the samples showed a lower Ni loading than the theoretical value. As described in the catalyst preparation section, the Ni-PS/SiO_2 was calcined to remove the residual ammonium ion, then added to the zeolite mother liquor. Considering calcination could decrease the solubility and surface silanol of Ni-PS/SiO_2, both would be adverse to the transformation of Ni-PS/SiO_2 into Ni-PS@S-1. Consequently, the Ni loss was detected.

Table 4.6. Properties of the as-prepared Ni-PS@S-1 catalysts

Catalyst	1.5 wt%	2.0 wt%	2.5 wt%	3.0 wt%
Ni loading[a] (wt.%)	1.29	1.68	2.24	2.67
S_{BET}[b] (m^2/g)	479	474	465	464
V_{micro}[c] (cm^3/g)	0.169	0.165	0.164	0.178

[a]. Measured by XRF

[b]. Calculated by BET equation

[c]. Calculated by t-plot method

Fig. 4.4a and **Table 4.6** show the N_2-physisorption results. All the samples exhibited prominent nitrogen adsorption capacity at the p/p_0 of around 0. Compared to the Ni-PS/SiO_2, the as-prepared Ni-PS@S-1 samples provided BET specific surface area of 460-480 m^2/g and micropore volume of 0.16-0.18 cm^3/g. The N_2-physisorption results mean the resulting Ni-PS@S-1 catalysts possess well-developed micropores.

Then, the calcined samples were measured by XRD. As displayed in **Fig. 4.4b**, all the Ni-PS@S-1 showed the typical characteristic peaks of MFI-type zeolite, suggesting that the high-crystalline Silicalite-1 formed in each preparation run. On the other hand, no distinguishable peaks of Ni-PS and NiO were detected because of the high dispersion and low content of nickel species in the Ni-PS@S-1 samples.

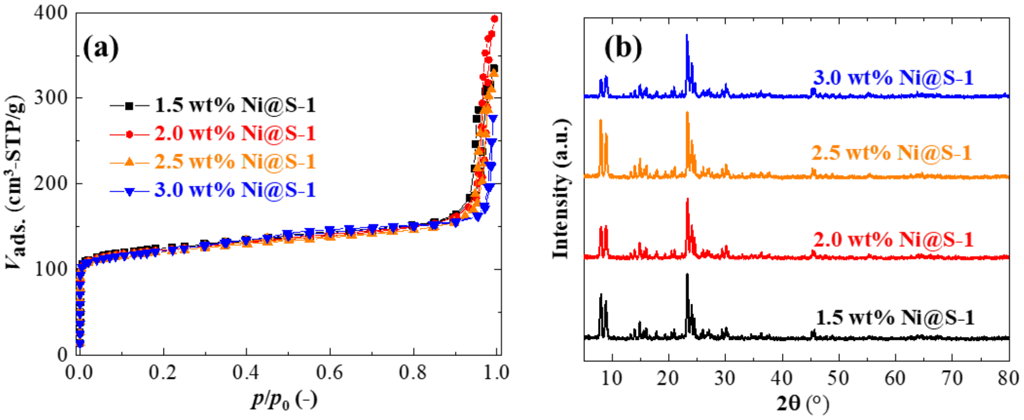

Figure 4.4. N_2-physisorption isotherms (a) and XRD patterns (b) of Ni-PS@S-1 catalysts after calcination in air at 550 °C for 12 h.

Next, the Ni-PS@S-1 samples were measured by SEM and presented in **Fig. 4.5**. All the prepared samples showed a coffin-shaped appearance, which was the typical morphology of MFI zeolite. The average particle size of Ni-PS@S-1 increased with Ni loading, namely, 140 nm for 1.5 wt% Ni-PS@S-1, 150 nm for 2.0 wt% Ni-PS@S-1, 165 nm for 2.5 wt% Ni-PS@S-1, and 270 nm for 3.0 wt% Ni-PS@S-1. This difference was owing to the different amounts of TEOS added to the zeolite mother liquor. It is widely accepted that the silicon source with high solubility would lead to a higher supersaturation and faster nucleation in zeolite mother liquor, which might provide more nucleation sites and favor the formation of small crystals.[11] As illustrated in the catalyst preparation part, the silicon source was provided by Ni-PS/SiO_2 and TEOS together. Undoubtedly, TEOS is better soluble than Ni-PS/SiO_2. Therefore, considering that more TEOS needed to be added in the case of Ni-PS@S-1 with lower nickel loading, which eventually resulted in higher supersaturation and more nuclei in the zeolite mother liquor, and thereof the smaller particle size of the final sample could be obtained.

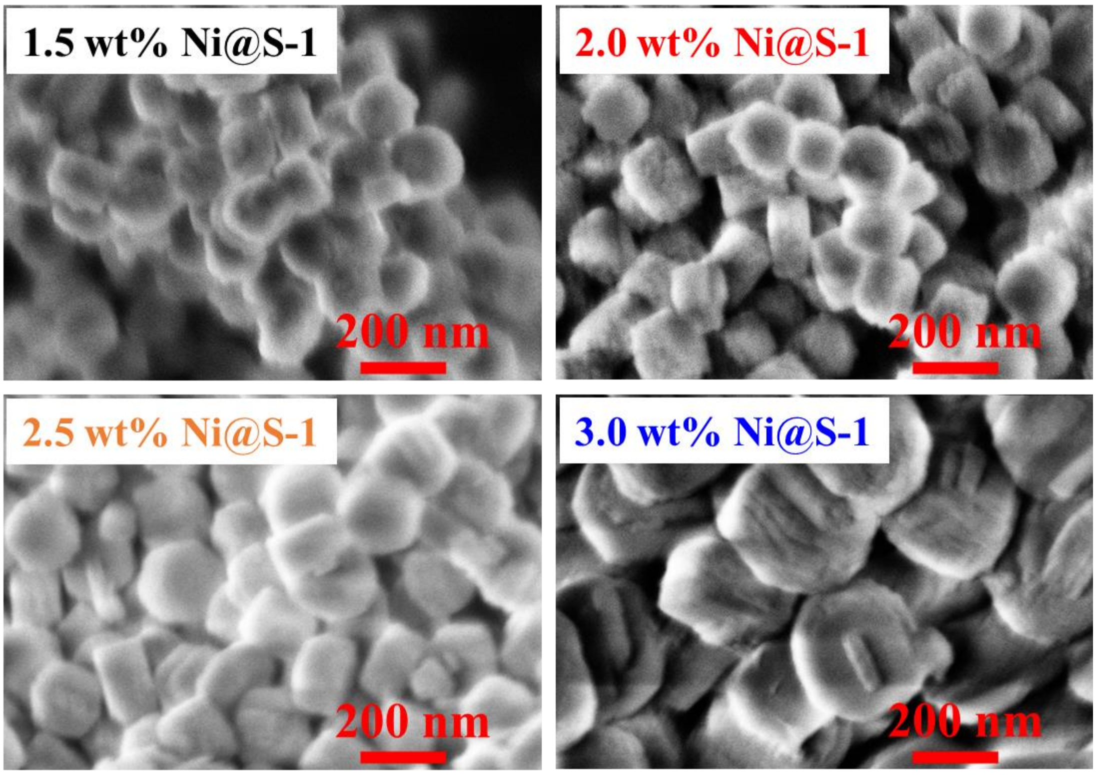

Figure 4.5. SEM images of Ni-PS@S-1 catalysts after calcination at 550 °C for 12 h.

The H_2-TPR was conducted to check the reducibility of Ni species in Ni-PS@S-1. As depicted in **Fig. 4.6**, all the samples exhibited a main and wide reduction peak from 600 °C to 900 °C. This peak should be assigned to the reduction of Ni-PS to Ni^0. Only 2.5 wt% Ni-PS@S-1 showed a tiny reduction peak in the range of 450-550 °C, which was attributed to the reduction of NiO to Ni^0. In short, most nickel atoms of Ni-PS@S-1 were in the form of Ni-PS.

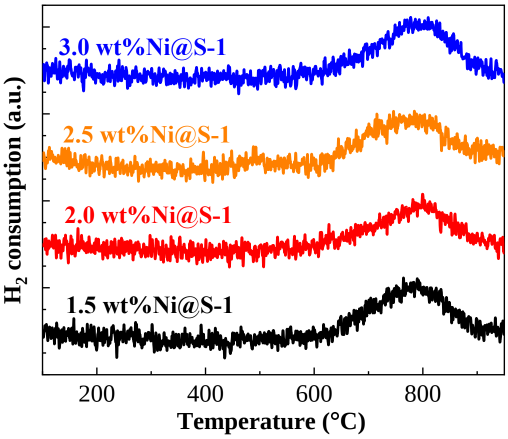

Figure 4.6. H_2-TPR profiles of the as-synthesized Ni-PS@S-1 catalysts

Fig. 4.7 presents the TEM images and the corresponding Ni NPs size distributions of Ni@S-1 catalysts after reduction in H_2 at 850 °C for 1 h. The Ni NPs were highly and uniformly dispersed over the Silicalite-1 support. Ni NPs were 3.3 nm in an average size and distributed in a narrow range of 2-7 nm when Ni loading increased from 1.5 wt% to 2 wt%. With increasing Ni loading to 2.5 wt%, the average size of Ni NPs was maintained at the same level, but some aggregated Ni particles with a diameter larger than 7 nm were found at the edge of Silicalite-1. This Ni sintering became severer as the Ni loading increased to 3 wt%. Ni NPs with a larger mean size of 5.4 nm and with broader size distribution from 1 to 13 nm were detected for 3 wt% Ni@S-1. More importantly, it is obvious that increasing number of Ni particles with bigger size were accumulated and situated at the edge of the zeolite, implying the poorer resistance to Ni sintering of 3 wt% Ni@S-1. In other words, most Ni NPs in Ni@S-1 with Ni loadings of 1.5 wt% and 2.0 wt% should be enveloped within Silicalite-1 crystal and thus exhibit excellent sintering-resistant ability. On the contrary, gradual increase in the number of nickel particles located outside the Silicalite-1 and aggregated into larger particles upon enhancing Ni loadings to > 2 wt%.

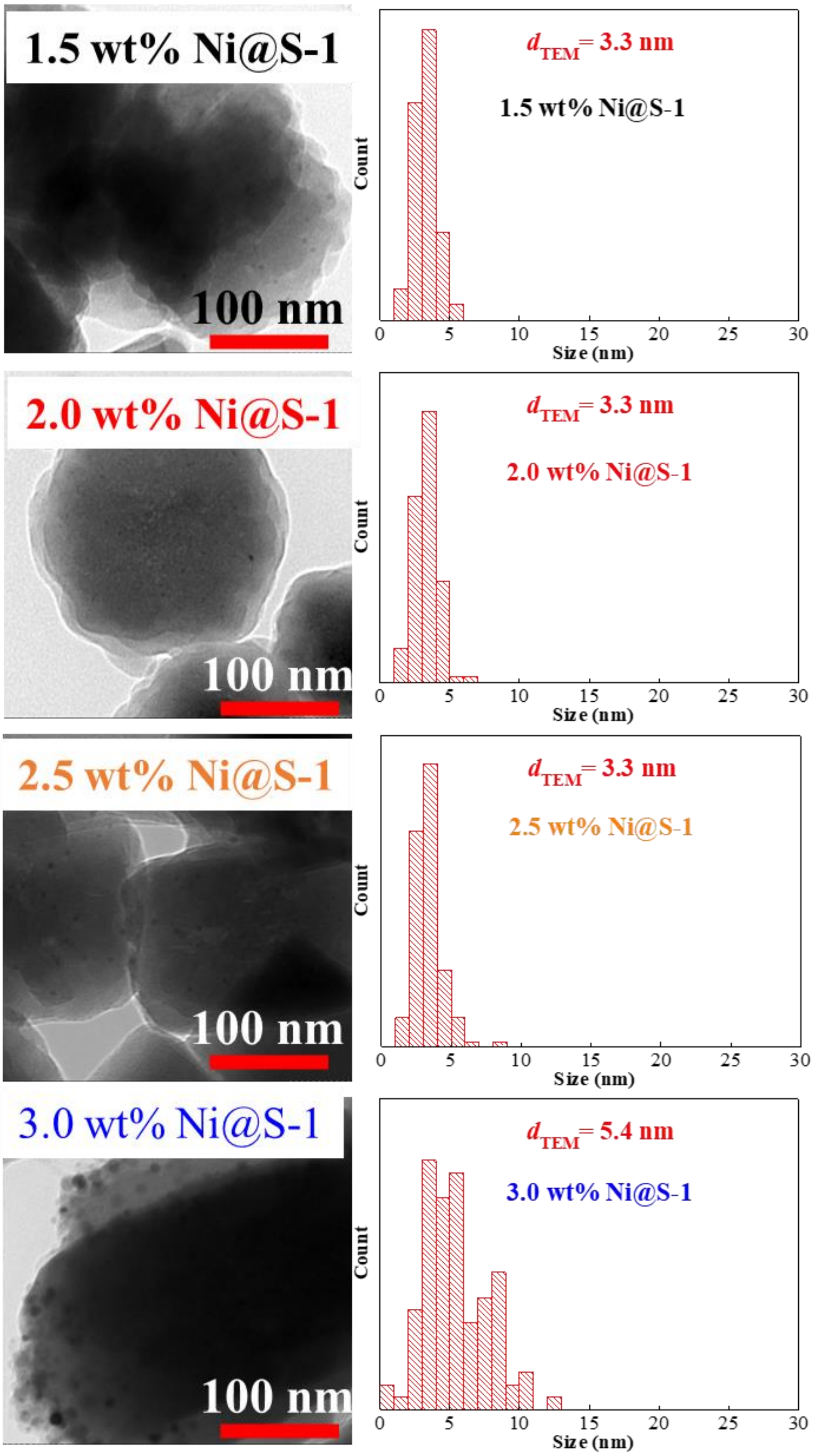

Figure 4.7. TEM images and the corresponding Ni NPs size distributions of Ni@S-1 catalysts after reduction in H_2 at 850 °C for 1 h.

Combined with the characterization results, as cartooned in **Fig. 4.8**, it can be assumed that majority of the Ni species were still stabilized and fixed in the structure of Ni-PS during the dissolution and crystallization processes in the case of low Ni loading. As a result, the Ni-PS was eventually embedded in the matrix of Silicalite-1. Contrarily, more Ni-PS/SiO_2 powder should be added in the higher Ni loading case. That is, according to probability theory, there is a higher probability that some Ni-PS species would be located on the external surface of Silicalite-1 zeolite. If so, after H_2 reduction, these exterior Ni species might aggregate and form larger Ni NPs on the external surface of the zeolite.

(a) Low Ni loading

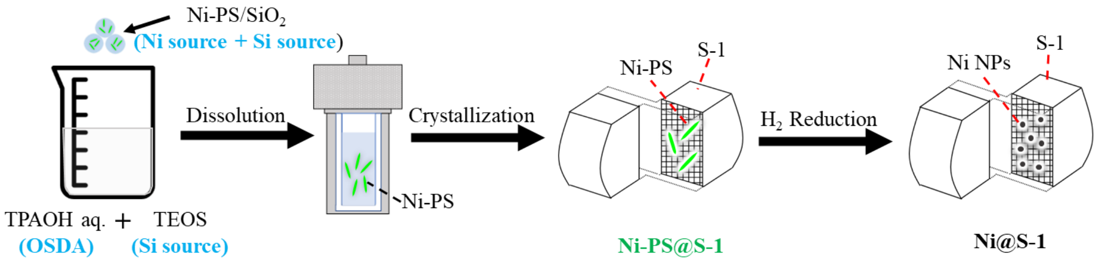

(b) High Ni loading

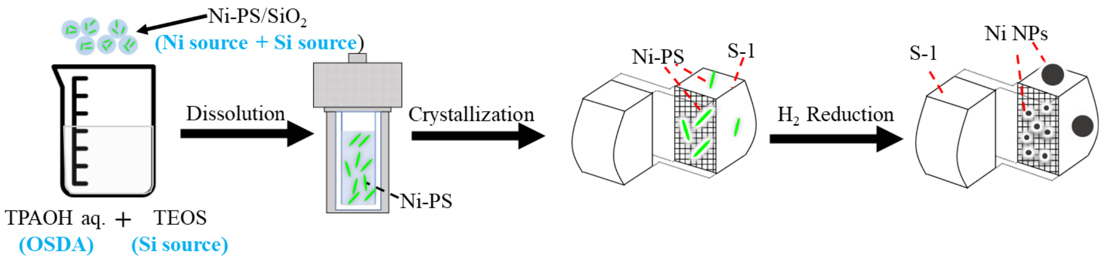

Figure 4.8. Schematic illustration of Ni@S-1 preparation with different Ni loadings from Ni-PS: (a) low Ni loading case and (b) high Ni loading case.

4.3.3. Evaluation of coking resistance for DRM at 600 °C

The DRM reaction was performed at 600 ºC for 5 h to evaluate the coking suppression of the as-prepared Ni@S-1 catalysts. **Fig. 4.9** displayed the associated results. It is clear in **Fig. 4.9a** that 1.5 wt% Ni@S-1 and 2.0 wt% Ni@S-1 could reach and keep at the equilibrium CH_4 conversion rate during the DRM reaction, while the CH_4 conversion rate declined as the Ni loading increased to 2.5 wt% and 3.0 wt%. The 3.0 wt% Ni@S-1 showed the lowest CH_4 conversion rate among the four samples. Similarly, the CO_2 conversion rate exhibited the same trend in **Fig. 4.9b**, say, 1.5 wt% Ni@S-1 and 2.0 wt% Ni@S-1 achieved the stable equilibrium conversion of CO_2. By contrast, continuous activity reduction was detected when the Ni loadings were 2.5 wt% and 3.0 wt.%. **Fig. 4.9c** shows the molar ratio of H_2 to CO in the product gas. Not surprisingly, 1.5 wt% Ni@S-1 and 2.0 wt% Ni@S-1 realized the equilibrium value. Interestingly, 2.5 wt% Ni@S-1 could almost reach the equilibrium, but 3.0 wt% Ni@S-1 showed a slightly higher H_2/CO molar ratio than that of equilibrium. It indicated that the coke formation from concurrent methane decomposition occurred over the 3 wt% Ni@S-1 catalyst to generate more H_2 in the product gas.

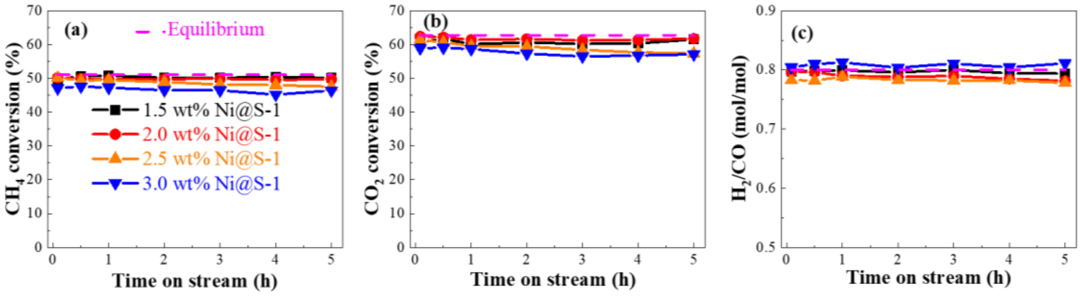

Figure 4.9. Catalytic performances of the as-prepared catalysts for DRM reaction at 600 °C as function of time on stream: (a) CH_4 conversion, (b) CO_2 conversion, and (c) H_2/CO ratio, (reaction conditions: T= 600 °C, 1 bar, CH_4/CO_2/Ar/ He= 20/20/40/10mL/min, GHSV= 2,000 L/g-Ni/h).

The coke content of the Ni@S-1 catalysts after the DRM reaction was estimated by TG analysis. As listed in **Table 4.7**, the coke content was 1.1 wt% for both 1.5 wt% Ni@S-1 and 2.0 wt% Ni@S-1. Comparatively, the amounts of coke were measured to be 5.4 wt% and 17.3 wt% for 2.5 wt% Ni@S-1 and 3.0 wt% Ni@S-1, respectively. The coke content coincides well with the DRM evaluation result at 600 °C. The TEM images of the spent catalysts in **Fig. 4.10** supported the DRM and TG observations. There were no obvious carbon species in the spent 1.5 wt% Ni@S-1 and 2.0 wt% Ni@S-1. In contrast, carbon nanotubes were observed in the spent 2.5 wt% Ni@S-1 and 3.0 wt% Ni@S-1.

Table 4.7. Amount of coke formation after DRM evaluation at 600 °C for 5 h

Ni loading in the Ni@S-1 (wt%)	1.5	2.0	2.5	3.0
Coke content (wt.%)	1.1	1.1	5.4	17.3

The coke content was estimated on the net weight of Ni@S-1 catalyst excluding the weight of blank Silicalite-1 for dilution.

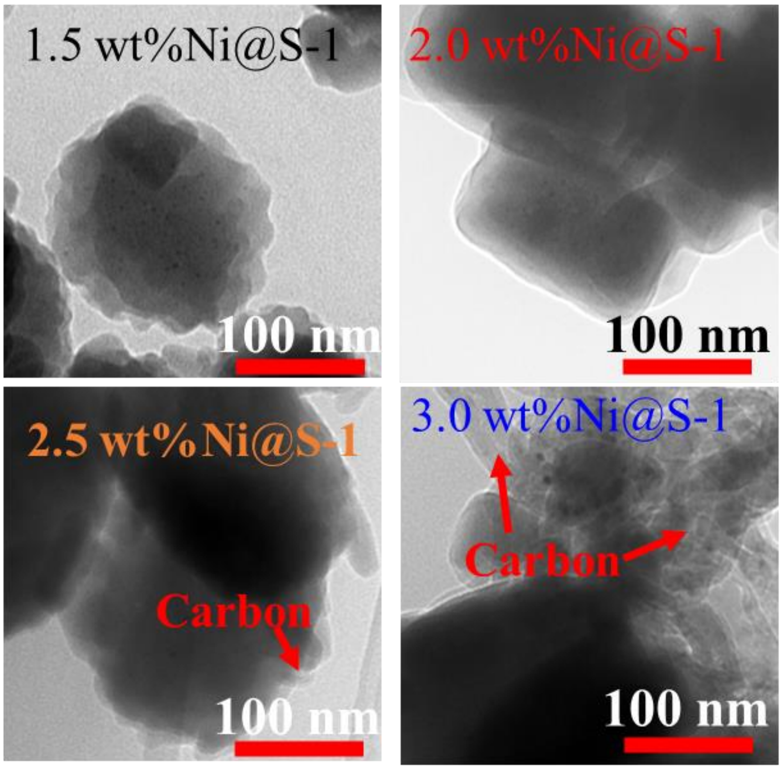

Figure 4.10. TEM images of spent Ni@S-1 catalysts after the DRM reaction at 600 °C for 5 h.

In summary, the characterization and DRM results suggested that most of the Ni NPs in 1.5 wt% Ni@S-1 and 2.0 wt% Ni@S-1 were immobilized in the Silicalite-1 zeolite and thus could effectively inhibit coke formation. On the contrary, 2.5 wt% Ni@S-1 and 3.0 wt% Ni@S-1, wherein part of Ni NPs were located on the external surface of the zeolite support. Those Ni particles without encapsulation were more likely to agglomerate and form relatively large particles. Accordingly, coke formation was favorable, and a large amount of coke was formed.

4.3.4. Evaluation of thermal stability for DRM at 850 ºC

Then, the 2 wt.% Ni@S-1 was analyzed for DRM reaction at 850 °C for 5 h to doublecheck its encapsulation structure and thermal stability. The evaluation results were shown in the **Fig. 4.11**. As expected, 2 wt.% Ni@S-1 exhibited stable and equilibrium activity thanks to the relatively ultrafine Ni particles of this catalyst to offer enough active sites.

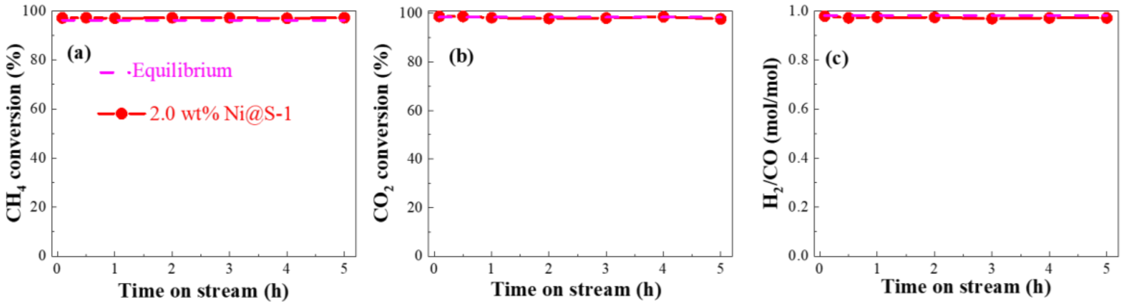

Figure 4.11. Catalytic performances of 2 wt% Ni@S-1 catalyst in the DRM reaction at 850 ºC as function of time on stream: (a) CH_4 conversion, (b) CO_2 conversion, and (c) H_2/CO ratio, (reaction conditions: T = 850 ºC, 1 bar, $CH_4/CO_2/Ar/$ He = 20/20/40/10mL/min, GHSV=2,000 L/g-Ni/h)

Additionally, as delineated in **Fig. 4.12**, the highly dispersed and ultrafine Ni nanoparticles of 2 wt% Ni@S-1 catalyst were sustained after DRM at 850 °C for 5 h. Once again confirming that the Ni nanoparticles should be fixed within the zeolite and hence generating the superior resistance to Ni sintering.

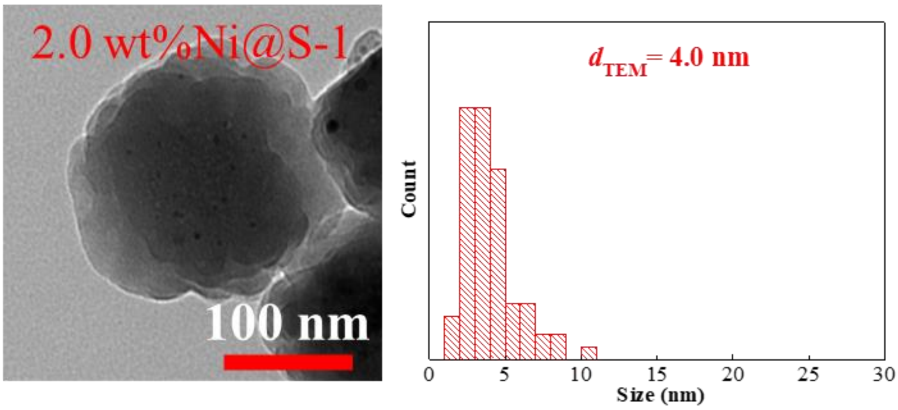

Figure 4.12. TEM images and the corresponding Ni NPs size distributions of spent 2 wt% Ni@S-1 catalyst after the DRM reaction at 850 °C for 5 h.

Finally, the durability of the 2 wt% Ni@S-1 was carried out by varying the GHSV from 2,000 to 40,000 L/g-Ni/h to check the catalytic performance under more severe conditions. Remarkably, as shown in **Fig. 4.13**, three catalytic performance indicators, namely, CH_4 conversion, CO_2 conversion, and H_2/CO ratio, were comparable to those of the low GHSV case reported in **Fig. 4.11**. Notably, the activity was maintained after running for 24 h, demonstrating the excellent DRM activity and thermal stability of the 2 wt.% Ni@S-1. Therefore, the preparation of Ni@S-1 catalyst with ultrafine Ni nanoparticles and encapsulation structure is achieved when the Ni loading increases from 1 wt% to around 2 wt%.

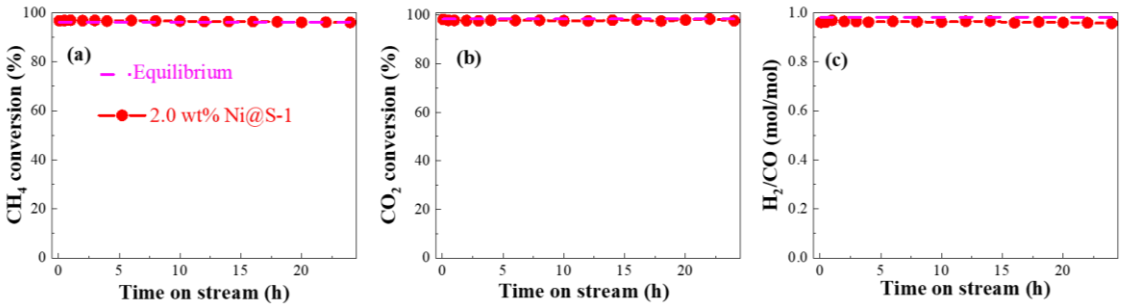

Figure 4.13. Catalytic performances of the as-prepared catalysts in the DRM reaction at 850 ºC as function of time on stream: (a) CH_4 conversion, (b) CO_2 conversion, and (c) H_2/CO ratio, (reaction conditions: T = 850 ºC, 1 bar, $CH_4/CO_2/Ar/$ He = 20/20/40/10mL/min, GHSV = 40,000 L/(g-Ni. h)).

[Catalyst was diluted with blank Silicalite-1 to decrease the catalyst amount.]

4.4. Conclusion

In this chapter, efforts were made to prepare a Ni@S-1 catalyst with a higher Ni loading using Ni-PS as the precursor. The Ni loading was successfully raised from 1 wt% to 2 wt% without any decrease in its catalytic performance, as evidenced by its high activity, effective suppression of coke formation, and excellent resistance to Ni sintering during DRM reaction. These outstanding results were attributed to the presence of ultrafine Ni nanoparticles embedded within the thermally stable zeolite shell. However, for Ni loading greater than 2.5 wt%, unencapsulated and aggregated Ni particles with larger sizes on the surface of Silicalite-1 were observed. To achieve Ni@S-1 with a high Ni loading (greater than 3 wt%), modifications to the preparation strategy are necessary. Potential approaches include adopting a solvent-free or dry-gel conversion method, and/or incorporating promoters to enhance Ni dispersion and resistance to sintering.

Reference

(1) Liu, Y.; Chen, Y.; Gao, Z.; Zhang, X.; Zhang, L.; Wang, M.; Chen, B.; Diao, Y.; Li, Y.; Xiao, D.; Wang, X.; Ma, D.; Shi, C. Embedding High Loading and Uniform Ni Nanoparticles into Silicalite-1 Zeolite for Dry Reforming of Methane. *Appl Catal B* **2022**, *307*.

(2) Song, Q.; Ran, R.; Li, D.; Zhao, B.; Weng, D. Synthesis of Highly-Dispersed Ni/Mesoporous Silica via an Ammonia Evaporation Method for Dry Reforming of Methane: Effect of the Ni Loadings. *Catalysis Surveys from Asia* **2021**, *25* (3), 312–323.

(3) Nguyen, L. Q.; Abella, L. C.; Gallardo, S. M.; Hinode, H. Effect of Nickel Loading on the Activity of Ni/ZrO2 for Methane Steam Reforming at Low Temperature. *Reaction Kinetics and Catalysis Letters* **2008**, *93* (2), 227–232..

(4) Lin, X.; Li, R.; Lu, M.; Chen, C.; Li, D.; Zhan, Y.; Jiang, L. Carbon Dioxide Reforming of Methane over Ni Catalysts Prepared from Ni–Mg–Al Layered Double Hydroxides: Influence of Ni Loadings. *Fuel* **2015**, *162*, 271–280.

(5) Rahbar Shamskar, F.; Rezaei, M.; Meshkani, F. The Influence of Ni Loading on the Activity and Coke Formation of Ultrasound-Assisted Co-Precipitated Ni–Al2O3 Nanocatalyst in Dry Reforming of Methane. *Int J Hydrogen Energy* **2017**, *42* (7), 4155–4164.

(6) She, Z. W.; Kibsgaard, J.; Dickens, C. F.; Chorkendorff, I.; Nørskov, J. K.; Jaramillo, T. F. Combining Theory and Experiment in Electrocatalysis: Insights into Materials Design. *Science* **2017**, *355* (6321).

(7) Li, F.; Han, G. F.; Noh, H. J.; Kim, S. J.; Lu, Y.; Jeong, H. Y.; Fu, Z.; Baek, J. B. Boosting Oxygen Reduction Catalysis with Abundant Copper Single Atom Active Sites. *Energy Environ Sci* **2018**, *11* (8), 2263–2269.

(8) Liu, Y.; Chen, Y.; Gao, Z.; Zhang, X.; Zhang, L.; Wang, M.; Chen, B.; Diao, Y.; Li, Y.; Xiao, D.; Wang, X.; Ma, D.; Shi, C. Embedding High Loading and Uniform Ni Nanoparticles into Silicalite-1 Zeolite for Dry Reforming of Methane. *Appl Catal B* **2022**, *307*.

(9) Sivaiah, M. v.; Petit, S.; Barrault, J.; Batiot-Dupeyrat, C.; Valange, S. CO2 Reforming of CH4 over Ni-Containing Phyllosilicates as Catalyst Precursors. *Catal Today* **2010**, *157* (1–4), 397–403.

(10) Wu, T.; Zhang, Q.; Cai, W.; Zhang, P.; Song, X.; Sun, Z.; Gao, L. Phyllosilicate Evolved Hierarchical Ni- and Cu-Ni/SiO2 Nanocomposites for Methane Dry Reforming Catalysis. *Appl Catal A Gen* **2015**, *503*, 94–102.

(11) Čejka, J.; Bekkum, H. van; Corma, A. *Introduction to Zeolite Science and Practice*, 3rd Revised Edition. Elsevier, **2007**.

Chapter 5. Conclusions and perspectives

5.1. Conclusions

Given the rising global demand for syngas to produce value-added fuels and chemicals, a green and cheap route for syngas production is of great importance. Methane has become abundantly available thanks to technological advancement and the discovery of large reserves of natural gas resources. Therefore, methane reforming to produce syngas is the feasible and attractive option and pathway. Among the reported methane reforming processes, dry (CO_2) reforming of methane (DRM) can convert and remove two leading greenhouse gases, CO_2 and CH_4, into syngas and has drawn much attention due to its remarkable environmental and industrial significance. Highly active and durable catalyst plays a critical role in the commercialization of DRM reaction. Ni-loaded catalyst has been demonstrated to be the most promising for the wide-scale application of the DRM process owing to its high activity and low cost. However, the Ni-based catalyst prepared by the conventional impregnation method suffered from fast deactivation under harsh DRM conditions. Considerable research efforts have been devoted to developing Ni-supported catalysts with high activity and stability. Encapsulation of ultrafine Ni NPs in the Silicalite-1 zeolite has shown exceptional DRM performances in high activity, good resistance to Ni sintering, and excellent suppression of coke formation.

Accordingly, in this study, a new methodology for encapsulating ultrafine nickel (Ni) nanoparticles within Silicalite-1 zeolite (Ni@S-1) was developed and demonstrated. The novel aspect of this method is the utilization of Ni-PS powder as the nickel source, which has not been previously reported. The Ni@S-1 catalyst prepared exhibited exceptional performance characteristics, including high and durable DRM activity, superior resistance to coking and sintering, and remarkable thermal stability. This discovery offers novel strategy to develop highly active and stable Ni@S-1 catalyst for the DRM reaction.

Chapter 2 investigated several parameters, such as reactants concentration, HTS time, and HTS temperature, to get the optimal synthesis conditions and study the formation mechanism of Ni@S-1 catalyst from Ni-PS. Accordingly, the appropriate conditions to prepare the ideal Ni@S-1 catalyst were hydrothermally treated at 100 °C for three days with an water-to-silica ratio of 50 in the zeolite mother liquor. In addition, the formation mechanism was explained as follows: during the HTS process, the nucleation step led to some zeolite nuclei forming around the Ni-PS, followed by crystal growth; the Ni-PS species were immobilized within primary zeolite crystals. However, after that, the redissolution and recrystallization of zeolite to form larger crystals with higher purity occurred, which could result in the confined nickel species migrating from the internal to the external surface of the zeolite when the HTS time was excessive. Thus, controlling the crystallization speed and time could prepare desired Ni@S-1 catalyst with most Ni NPs encapsulated in the zeolite.

Then, **Chapter 3** evaluated and compared the coking suppression, sintering resistance, and durability of the Ni-PS-derived Ni@S-1 catalyst with the counterparts, namely, Ni/S-1 and Ni/SiO_2 catalysts. The Ni@S-1 catalyst with core@shell structure showed excellent DRM activity, good coking and sintering resistance, and longevity. The superior catalytic activity and stability of the Ni@S-1 catalyst were ascribed to the formation and maintenance of ultrafine Ni nanoparticles within thermally stable Silicalite-1 zeolite support.

Chapter 4 was dedicated to preparing Ni@S-1 catalyst with high Ni loading to achieve better mass-specific catalytic activity, thus enhancing the catalytic efficiency and reducing the cost. The encapsulation structure and the ultrafine nickel particles of the Ni@S-1 catalyst maintained, and its DRM catalytic performance did not decline when the nickel content was increased from 1 wt% to 2 wt%. On the contrary, in the case of high nickel loadings, such as 2.5 wt% and 3.0 wt%, an increasing number of Ni-PS species might be located on the Silicalite-1 external surface, resulting in larger Ni NPs formed after the H_2 reduction. Consequently, the lower DRM activity and higher coke content after the DRM reaction were observed over these two catalysts.

5.2. Perspectives

Although the Ni@S-1 catalyst using Ni-PS as the Ni source showed superior activity and stability for DRM reaction under the current evaluation conditions, several challenges should be examined and overcome to achieve wide-scale industrial application. Firstly, the molar ratio of H_2 to CO in the produced gases was lower than 1, which cannot meet the different downstream requirements. Therefore, feeding steam and/or oxygen into the DRM system to conduct combined methane reforming was needed to adjust the composition of product gas flexibly and to examine the catalytic performances of the Ni@S-1 under harsher and more complex conditions. On the other hand, reforming reactors typically operate at high pressures, 3–20 bar, to decrease reactor size and to meet the high-pressure needs of gas separation and purification and downstream syngas applications. Accordingly, the high-pressure evaluation of the Ni@S-1 was indispensable. Furthermore, the reusability and regeneration of the catalyst should also be investigated.

Additionally, modification and further development of the preparation method was required if the Ni@S-1 with higher Ni loading (> 5 wt%) was desired. In view of the fact that trace of solvent was requied, dry-gel conversion method or solvent-free synthesis may be useful to reduce the risk of Ni ion dissolving in the zeolite mother liquor, thereof lessening the Ni NPs on the external surface of the catalyst.

Chapter 6. Appendix.

Preparation of Ni@S-1 catalyst at 180 °C for different time

6.1. Experimental

6.1.1. Catalyst Preparation

The Ni@S-1 catalysts with theoretical Ni loading of 1 wt% were prepared by a two-step method. Firstly, as shown in **Fig. 6.1**, 3 wt% Ni-PS/SiO_2 was prepared by hydrothermal synthesis. Then, the 1 wt% Ni@S-1 catalyst was prepared using the as-synthesized 3 wt.% Ni-PS/SiO_2 as the precursor by second hydrothermal treatment.

Step 1. Preparation of 3 wt% Ni-PS/SiO_2 by HTS method.

Table 6.1. Preparation conditions of 3wt% Ni-PS/SiO_2

Parameter	Theoretical value
Ni loading	3 wt%
H_2O/Si	34 mol/mol
NH_3/Ni	60 mol/mol
Zeolite mother liquor volume	75 mL (100 mL of autoclave reactor)
HTS temperature	100 °C
HTS time	3 d

1) added calculated amounts of 1M of $Ni(NO_3)_2$ aqueous solution to diluted 3.0 M of ammonia solution to form the nickel ammonia complex solution.

2) Si source, TEOS, was added to the above nickel ammonia complex solution and stirring for 2 h.

3) transferred the mixture into Teflon-lined autoclave reactor and hydrothermal treated at 100 °C for three days.

4) washed samples with distilled water three times and recovered the samples by centrifugation.

5) dried at 110 °C overnight.

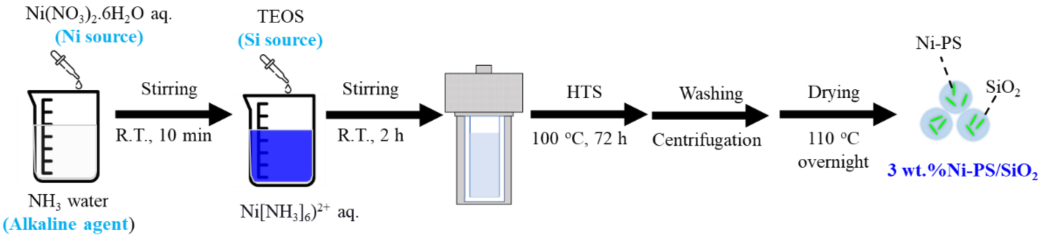

Figure 6.1. Preparation procedures of 3 wt.% Ni-PS/SiO_2

Step 2. Preparation of 1 wt% Ni@S-1 catalyst using the as-prepared 3 wt% Ni-PS/SiO_2 as the Ni source by HTS method at 180 °C for different time

Then, the Ni@S-1 catalysts were prepared at 180 °C for different time using the above-synthesized 3 wt% Ni-PS/SiO_2 as the Ni source. The preparation procedures and conditions are shown in the below and **Fig. 6.2**.

1) preparation of zeolite mother liquor by mixing calculated amounts of TEOS, TPAOH, and distilled water at room temperature for 24 h to form a homogenous gel.

2) added designated amount of the 3 wt.% Ni-PS/SiO_2 precursor to the zeolite mother liquor and stirring for 2 h.

3) transferred into a Teflon-sealed autoclave and hydrothermally treated at 180 °C for different time in a tumbling oven.

4) washed samples with distilled water three times and recovered the samples by centrifugation.

5) drying at 110 °C overnight and calcined at 550 °C for 12 h.

6) reduced in 50 vol% H_2 at 850 °C for 1 h.

Table 6.2. Preparation conditions of Ni@S-1

Parameter	Theoretical value
Ni loading	1 wt%
Si/TPAOH	3 mol/mol
Si_{PS}/Si_{TEOS}	0.49 mol/mol
H_2O/Si	50 mol/mol
Zeolite mother liquor volume	75 mL (100 mL of autoclave reactor)
HTS temperature	180 °C
HTS time	**12 h, 24h, 48 h, and 72 h**

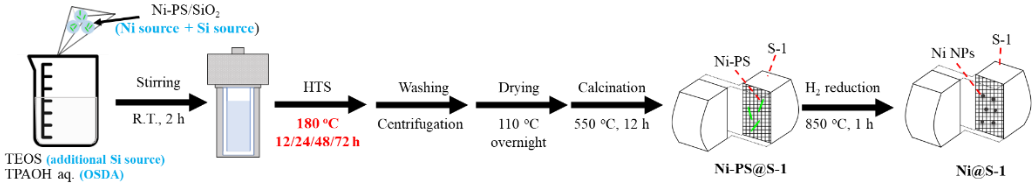

Figure 6.2. Preparation procedures of Ni@S-1

6.1.2 Catalyst Characterization

The characterization methods and corresponding acquired information are listed in **Table 6.3**. The measurement conditions were explained in the **Chapter 2**.

Table 6.3. Characterization techniques and corresponding acquired information

Characterization	Acquired information
XRF	Ni loading
XRD	Crystallographic information
SEM	Catalyst morphology
TEM	Ni NPs location and size, and carbon formation
N_2-sorption	Porosity, surface area, and pore volume
H_2-TPR	The reducibility of Ni
TG-DTA	Coke content

6.1.3 Catalytic Performance Evaluation

The catalytic performances and Ni location of the prepared catalysts were evaluated by DRM reaction at 600 °C in a down-flow fixed bed reactor. The evaluation conditions are listed in **Table 2.6**. The evaluation details and illustration of the DRM apparatus are described in **Chapter 2**.

Table 6.4. Catalytic evaluation conditions for the DRM reaction

Pressure	1 bar
H_2 reduction	60 mL/min of 50 vol.% H_2/N_2, 850°C, 1h
DRM temperature	600 °C
Reactant gas	CH_4: CO_2: Ar: He = 20: 20: 40: 10 mL/min
GHSV	2,000 L/g-Ni/h.

6.2. Results and discussion

The characterization results of the catalysts prepared at 180 °C for different time were shown below. The Ni loadings of all the samples measured by XRF were lower than the theoretical value, indicating some nickel might be dissolved in the solution. It was well-known that the higher HTS temperature would lead to the higher solubility of the solid matter, so more Ni-PS species were dissolved into Ni ion into the zeolite mother liquor and were not incorporated into the zeolite. The XRD patterns and corresponding calculated relative crystallinity results reveal that it took only 24 h to obtain full crystalline zeolite crystals at 180 °C, which was much shorter than 72 h at 100 °C. However, the XRD results (Fig. 6.3a) and SEM images (Fig. 6.4) tell that all the samples synthesized at 180 °C showed the higher relative crystallinity and bigger crystal length compared to that of the reference sample prepared at 100 °C for three days. These suggested that zeolite synthesized at higher hydrothermal temperatures initially tended to form larger crystals with lower surface energy and higher stability. In addition, the analysis of N_2-physisorption isotherms in Fig. 6.3 tell that all the samples from 180 °C exhibited lower mesopore volume (Table 6.5) than that of reference sample from 100 °C, indicating the zeolite crystals prepared at 180 °C had less intracrystalline mesopores. As discussed in the Chapter 2, the formation of larger crystal with less intracrystalline mesopores would result in more Ni-PS located on the external surface of the zeolite. Furthermore, not surprisingly, the crystal length generally increased and the mesopore volume decreased with the HTS time, suggesting larger crystals with less intracrystalline mesopores formed with increasing HTS time.

Table 6.5. Properties of the as-prepared samples after calcination at 550 °C for 12 h.

Sample	Ni loading[a] (wt%)	RC[b] (%)	Crystal length[c] (nm)	V_{mesod} (cm^3/g)
Ni@S-1-100°C-72h	0.99	100.0	220	0.354
Ni@S-1-180°C-12h	0.96	134.8	370	0.216
Ni@S-1-180°C-24h	0.97	164.2	320	0.130
Ni@S-1-180°C-48h	0.87	152.9	330	0.099
Ni@S-1-180°C-72h	0.94	166.9	770	0.097

[a] Measured by XRF.

[b] Relative crystallinity was calculated on the basis of the intensity of the peak at around 23.1° and assumed that the crystallinity of Ni@S-1-100°C-72h was 100%.

[c] Measured by SEM

[d] Measure by N$_2$-physisorption

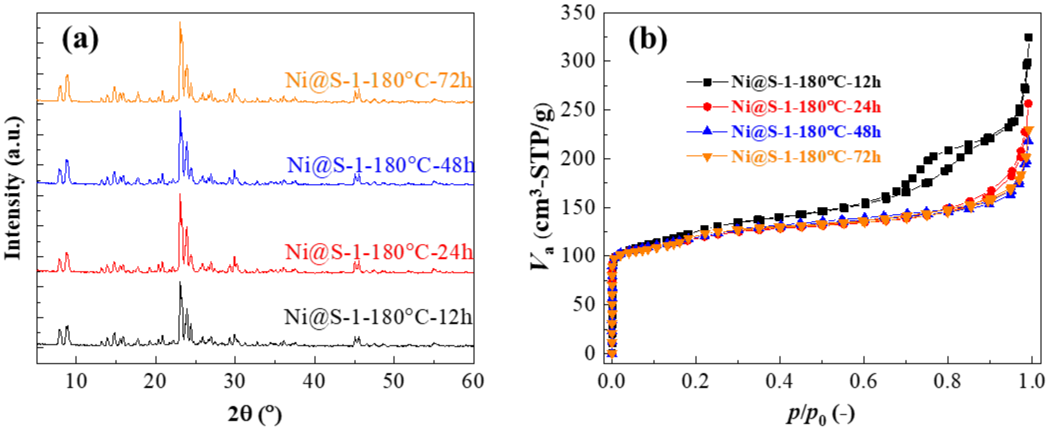

Figure 6.3. (a) XRD patterns and (b) N$_2$-physisorption isotherms of the as-prepared Ni@S-1 samples after calcination at 550 °C for 12 h.

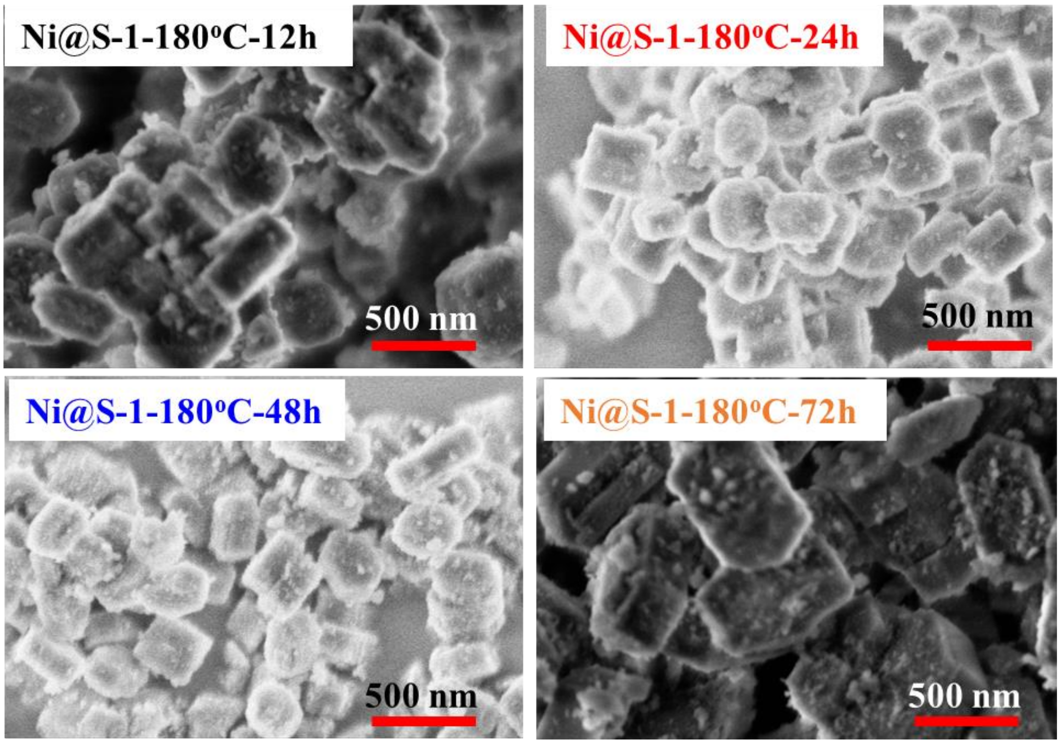

Figure 6.4. SEM images of the as-prepared Ni@S-1 samples after calcination at 550 °C for 12 h.

The TEM images and statistical results of Ni NPs of the obtained samples after after H_2-reduction at 850 °C for 1 h agreed with the observations above. The Ni@S-1-180°C-12h sample exhibited the larger Ni NPs in size and broader size distribution than Ni@S-1-180°C-24h. As shown in the XRD and SEM results, the Ni@S-1-180°C-12h sample was not full crystalline zeolite, and some unconverted amorphous silica was left in the sample. Therefore, the Ni species supported on the amorphous phase with poor thermal stability sintered after H_2-reduction to form larger Ni NPs. Consistent with the situation synthesized at 100 °C, the redissolution-recrystallization proceeded with time, resulting in growth of zeolite particles in the cases of longer HTS time of 48 h and 72 h. During this process, Ni species immobilized inside the zeolite particles migrated to the outer surface of the zeolite. After H_2-reduction, larger Ni NPs formed. Moreover, all the samples in the case of 180 °C synthesis had a larger average nickel particle diameter than that of the catalyst from 100 °C (2.9 nm), demonstrating that the higher HTS temperature favored the formation of larger crystals with fewer nickel species immobilized inside the zeolite, even with shorter HTS time.

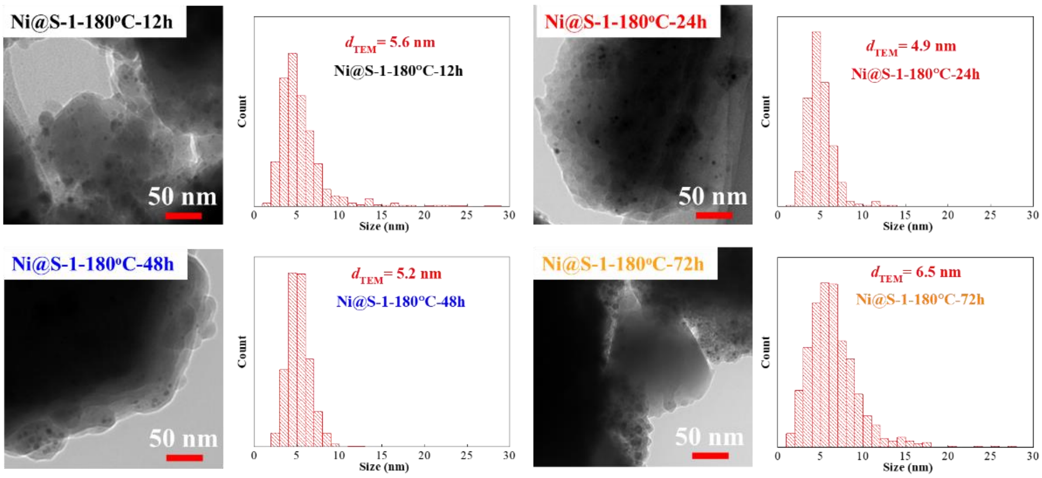

Figure 6.5. TEM images of the as-prepared Ni@S-1 samples after H_2-reduction at 850 °C for 1 h.

The DRM reaction results in the **Fig. 6.6** confirm that all the samples could not reach equilibrium activity due to the insufficient active sites. Additionally, all the samples showed higher coke content in comparison with that of Ni@S-1-100°C-72h, revealing more Ni NPs were located on the external surface of the zeolite in the cases of synthesizing at 180 °C.

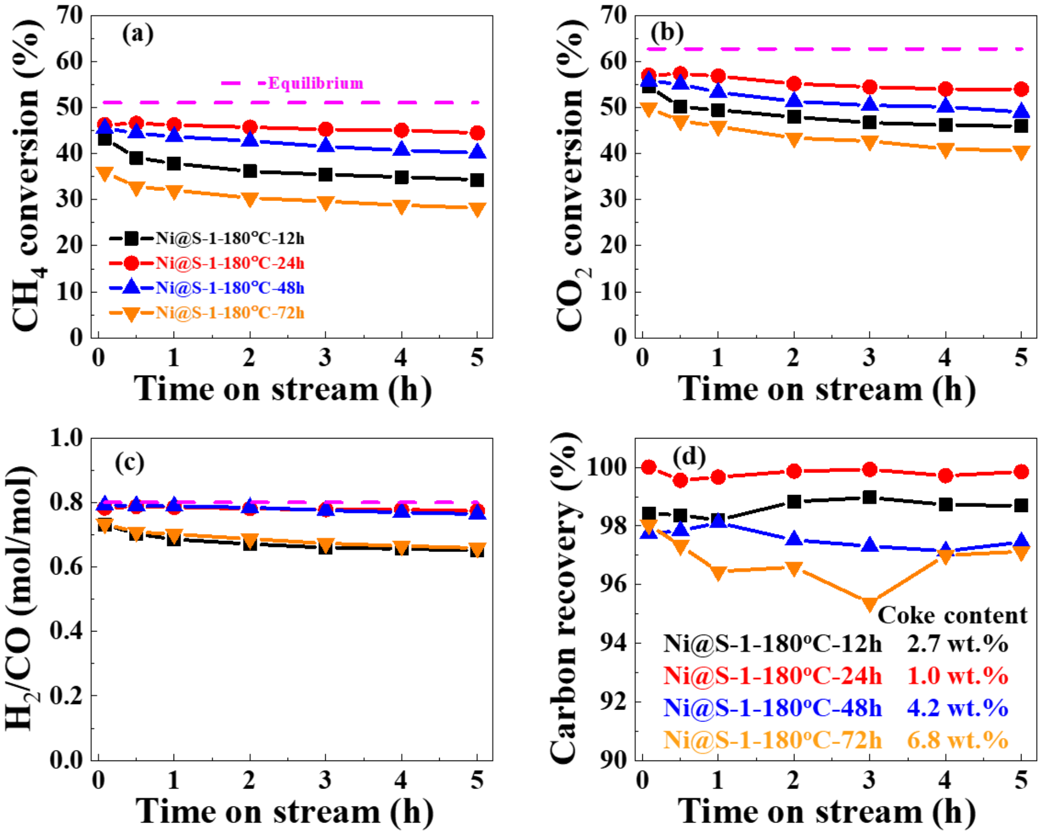

Figure 6.6. Catalytic performances of the as-prepared Ni@S-1 catalysts for DRM reaction at 600ºC as function of time on stream: (a) CH_4 conversion, (b) CO_2 conversion, (c) H_2/CO ratio, and (d) gaseous carbon recovery (reaction conditions: T= 600 ºC, 1 bar, CH_4/CO_2/Ar/ He= 20/20/40/10mL/min, GHSV= 2,000 L/g-Ni/h).

6.3. Conclusion

The synthesis of Ni@S-1 catalyst using Ni-PS as a nickel source at a high hydrothermal temperature of 180°C results in faster crystallization, leading to a fully crystalline zeolite in a shorter time. However, this high temperature also brings several challenges. Firstly, the chemical and physical properties of the hydrothermal system are significantly altered, such as higher saturated vapor pressure, lower viscosity and density of water, and higher solubility of reactants. Consequently, this high temperature also favors the formation of larger, more thermodynamically stable crystals with fewer inter-crystalline mesopores and reduced immobilization of nickel species very fast. Furthermore, higher temperature could result in the aggregation of Ni species during the crystallization to reduce the surface energy. In addition, the enhanced solubility would cause more Ni species dissolved in the water, so higher Ni loss could be detected.

Acknowledgement

Life is a miracle. When I was 14 or 15 years old, an elder wished me out of courtesy, after I helped him, that I would have the opportunity to study abroad. At the time, it was beyond imagination for a child living in a remote and poor mountainous area of China. But fabulously, I am now writing this acknowledgment for my doctoral dissertation at the Tokyo Institute of Technology. I am so lucky to have had the opportunity to receive my doctoral degree, and I owe it all to the help and support of many kind people along the way.

First and foremost, I would like to thank my supervisor, Professor Teruoki Tago, for giving me the precious opportunity to study in your laboratory and pursue my Ph.D. Your profound knowledge, sagacity, rigor, enthusiasm, easy-going personality, and even your sense of humor are all qualities that I will carry with me throughout my lifelong learning journey. I also sincerely thank Assistant Professor Kentaro Kimura and Assistant professor Hiroyasu Fujitsuka. Although I only worked with you for less than one year in the same lab, you both provided me with selfless help in my daily experimental work, feedback and presentation, and paper or thesis writing.

I am deeply grateful to Wang, Lukpla, Goto, Ye, Ding, Saito, Sano, Rikako, Saika, Takahashi, Kanomata, Abiru, Kojima, Endo, Yokosawa, Nodoka, Sakanushi, Iizuka, Asami, Sun, Tan, Tsuchiya, Awano, Pim, and all others who have helped me during my doctoral studies. I couldn't have done it without your kindness and support.

I would also like to express my gratitude to Professor Sekiguchi, Professor Shimoyama, Professor Matsumoto, and Professor Yokoi, all of whom were members of my Ph.D. thesis review committee. Your comments and suggestions on my Ph.D. thesis gave me a deeper and broader thinking of my research to improve my thesis.

I want to extend a heartfelt thank you to the staff of Open Facility Center at the Tokyo Institute of Technology, especially Mr. Kikuchi, for your patience in teaching me to use TEM and SEM.

Professor Zhan-guo Zhang, you always deserve my gratitude and respect to you. Without your recommendation, I never would have had the opportunity to study at the Tokyo Institute of Technology. Your kindness, rigor in doing research, patience, and care for students are all role-model for me to learn. I also sincerely thank Professor Yun-quan Yang, Professor Jian Yu, and Professor Chang-ming Li. It was your guidance during my master's study that allowed me to step into the world of science and develop an interest in doing research.

Without the support of the CSC scholarship, I cannot imagine if I would have been able to finish my Ph.D. study. Therefore, the financial help from CSC is greatly appreciated.

To my wonderful parents, Yong-gang Zhang and Xiu-ying Yang, I cannot thank you enough. You are the perfect parents for me. You gave me life and did your best to create the conditions for me to grow up healthy and happy, enabling me to study without worries and supporting me unconditionally in all my endeavors. Though you always say I am your pride, I am fully aware that all my achievements result from your silent efforts and support behind my back. In the past, you escorted me, and in the future, I will protect you.

I am also fortunate to have a far-sighted grandfather, Xue-jun Zhang, who has always loved and supported me. Your kindness and hard work are qualities that I have inherited, and you have also enlightened and supported me with your actions and life experiences. I am grateful for your wisdom and guidance, which have helped shape me into the person I am today.

I must also express my deepest condolence for the loss of my beloved aunt, Xiao-ying Zhang, who passed away after a long and difficult battle with leukemia while I was preparing for my doctoral dissertation defense. May you rest in peace, free from pain and suffering, and know that you will always be missed.

Finally, I would like to express my gratitude and love to the love of my life, Zhen-zhen Cai. Meeting and falling in love with you is my greatest blessing and reward. I spent most of my time in Japan in the past five years since we met, and I am sorry and regretful that I could not be by your side, especially when you needed me the most. I am grateful to have such a perfect partner as you, who always stands by me, encourages and comforts me, and gives me the energy to devote myself to my challenging doctoral studies. Thank you for being my pillar of strength and always believing in me, and I could not have achieved this milestone without you. I am confident that, as long as you are with me, no difficulty is insurmountable, and we will continue to love and support each other for the rest of our lives. I cannot wait to return to China and start our loving and happy family. Your unwavering love and support will be a constant source of inspiration and motivation throughout my life.

List of Publications and Presentations

Publications related to this thesis

[1] **Yusheng Zhang,** Ryota Takahashi, Kentaro Kimura, Hiroyasu Fujitsuka, Teruoki Tago. Development of Silicalite-1-encapsulated Ni catalyst from Ni phyllosilicate for dry reforming of methane. ***Catalysis Surveys from Asia***, 2023,27: 56-66.

[2] **Yusheng Zhang,** Ryota Takahashi, Yasutomo Iizuka, Kentaro Kimura, Hiroyasu Fujitsuka, Teruoki Tago. Study on the formation mechanism of Ni@S-1 catalyst from Ni phyllosilicate and its catalytic performance for the dry reforming of methane (*tentative*), ***In preparation***

Presentations

[1] **Yusheng Zhang**, Hiroyasu Fujitsuka, Ryota Takahashi, Teruoki Tago, Synthesis of Silicalite-1-encapsulated Ni catalyst from Ni phyllosilicate for dry reforming of methane. The 129th CATSJ meeting, online, March 2022 (Poster)

[2] **Yusheng Zhang**, Ryota Takahashi, Hiroyasu Fujitsuka, Teruoki Tago, Synthesis of Silicalite-1-encapsulated Ni nanoparticle catalyst from Ni phyllosilicate for dry reforming of methane. TOCAT9, Fukuoka, Japan, July 2022 (Oral)

[3] **Yusheng Zhang,** Ryota Takahashi, Yasutomo Iizuka, Hiroyasu Fujitsuka, Kentaro Kimura Teruoki Tago. Effect of Hydrothermal Temperature on Structure of Ni@S-1 from Ni Phyllosilicate and Its Catalytic Performance for Dry Reforming of Methane. The 5th Euro-Asia Zeolite Conference, Busan, Korea, February 2023 (Poster)

[4] 高橋暸太，**張喩昇**，木村健太郎，藤墳大裕，多湖輝興．シリケートを前駆体としたMFIゼオライト内包Ni触媒の開発とメタン改質活性評価．第38回ゼオライト研究発表会. 徳島，2022年12月（口头）

[5] 高橋暸太，**張喩昇**，木村健太郎，藤墳大裕，多湖輝興．優れたメタン改質活性を示すゼオライト内包金属微粒子触媒の開発．第130回触媒討論会. 富山，2022年09月（口头）

Other publications

[1] **Yu-sheng Zhang**,Changming Li, Chao Yu, Tuyetsuong Tran, Feng Guo, Yunquan Yang, Jian Yu, Guangwen Xu. Synthesis, characterization and activity evaluation of Cu-based catalysts derived from layered double hydroxides (LDHs) for DeNOx reaction. ***Chemical Engineering Journal,*** 2017, 330, 1082-1090.

[2] **Yu-sheng Zhang**, Changming Li, Chao Wang, Jian Yu, Guangwen Xu, Zhanguo Zhang, Yunquan Yang. Pilot-scale test of a V_2O_5-WO_3/TiO_2-coated type of honeycomb DeNO_x catalyst and its deactivation mechanism. ***Industrial & Engineering Chemistry Research,*** 2019, 58, 828-835.

[3] **Yu-sheng Zhang**, Changming Li, Hong Zeng, Chao Yu, Jian Yu, Yunquan Yang, Guangwen Xu, Shiqiu Gao. Preparation of V_2O_5–WO_3–TiO_2/Cordierite Based Catalytic Filter for Removal of NO_x from Flue Gas (in Chinese). ***The Chinese Journal of Process Engineering***, 2017, 17, 1249-1256. ***(selected as cover)***

[4] **Yu-sheng Zhang**, Li Jin, Yang Song, Koji Kuramoto, Zhan-guo Zhang. Experimental evidence for the dominating role of external coke deposition in the deactivation process of Mo/HZSM-5 catalysts in the nonoxidative methane dehydro-aromatization at 1073 K. Ready submit to ***Fuel***

[5] Lelin Zeng, Qin Yi,Xiaohui Peng, Zhi Huang, BartVan der Bruggen, **Yusheng Zhang,**Yan Kuang, Yingnan Ma, KewenTang. Modelling and optimization of a new complexing retardant-enhanced polymer inclusion membrane system for highly selective separation of Zn2+ and Cu2+. ***Separation and Purification Technology***, 2022, 292: 121056.

[6] Zhaohui Chen, Deliang Wang, Hang Yang, **Yusheng Zhang**, Yunjia Li, Changming Li, Jian Yu, Shiqiu Gao. Novel application of red mud as disposal catalyst for pyrolysis and gasification of coal. ***Carbon Resources Conversion***. 2021, 4, 10-18

[7] Lelin Zeng, Feixiang Zhou, Xuehui Zhan, **Yusheng Zhang**, Wanyun Xie, Guoxiang Wang, Enxiang Liang. Triethylene tetramine-modified crosslinked acrylonitrile as Cu (II) ion adsorbent by photo-induced precipitation polymerization. ***Iranian Polymer Journal***, 2021, 30(7): 685-695.

[8] Tuyetsuong Tran, Jian Yu, Changming Li, Feng Guo, **Yu-sheng Zhang**, Guangwen Xu. Structure and performance of a V_2O_5–WO_3/TiO_2–SiO_2 catalyst derived from blast furnace slag (BFS) for $DeNO_x$, ***RSC Advances***, 2017, 7, 18108-18119.

[9] Hong Zeng, Pingle Liu, **Yu-sheng Zhang**, Changming Li, Chao Yu, Jian Yu, Guangwen Xu, Shiqiu Gao. Development and Pilot Test of Surface-coating SCR Denitration Catalyst at Low Temperature (in Chinese), ***The Chinese Journal of Process Engineering***, 2017, 17, 1208-1216.

[10] YU Chao, LI Changming, **ZHANG Yusheng**, GUO Feng, YU Jian, YANG Yunquan, XU Guangwen. The effect of ceramic filter on the dispersion of catalytic particles and their DeNOx performance (in Chinese), ***Journal of Chemical Industry and Engineering of China***, 2018, 69(2): 682-689.